Influence of Nanoparticles and Carbon Nanotubes on Electrical Characteristics of Natural and Organic Dye-based Cell

Thesis submitted for the
Degree of Doctor of Philosophy (Science)
Of
Jadavpur University
2024

by

Arnab Kanti Karan

Condensed Matter Physics Research Centre
Department of Physics
Jadavpur University
Kolkata 700 032

Dedicated

to

my loving family

Declaration by the Author

I do hereby declare that the work embodied in this thesis entitled "***Influence of Nanoparticles and Carbon Nanotubes on Electrical Characteristics of Natural and Organic Dyes based Cell***", which is being submitted for the degree of Doctor of Philosophy (Science), is my own work and that, to the best of my knowledge and belief, neither the thesis nor any part thereof has been accepted for the award of any other degree or diploma of the university or other institute of higher learning, except where due acknowledgement has been made in the text.

Date: 20.06.2025

Place: Jadavpur University

Arnab Kanti Karan

(Arnab Kanti Karan)

CERTIFICATE FROM THE SUPERVISOR

This is to certify that the thesis entitled **"Influence of Nanoparticles and Carbon Nanotubes on Electrical Characteristics of Natural and Organic Dye-based Cell"**, submitted by **Mr. Arnab Kanti Karan** who got his name registered on **25th October 2019** for the award of Ph. D. (Science) Degree of Jadavpur University, is absolutely based upon his own work under the supervision of **Professor Nabin Baran Manik** and that neither this thesis nor any part of it has been submitted for either any degree/diploma or any other academic award anywhere before.

Dr. NABIN BARAN MANIK
Professor
Department of Physics
Jadavpur University
Kolkata - 700 032

Date: 20.06.25

.....

Dr. Nabin Baran Manik
Supervisor
Professor
Condensed Matter Physics Research Centre
Department of Physics
Jadavpur University
Kolkata 700 032

Acknowledgement

In this thesis, I summarise my five-year research journey. Throughout this period, I had the privilege of pursuing my Ph.D. at Jadavpur University, Kolkata, which proved to be an immensely rewarding experience.

I am profoundly grateful to my supervisor, Professor Nabin Baran Manik, for allowing me significant independence in my research. His invaluable guidance, patient encouragement, and direction were crucial over the years. His daily instructions were essential for executing experimental work, developing devices, and formulating new concepts. Without his active support, this work would have been very challenging.

I would also like to extend my gratitude to Dr. Chittaranjan Sinha, Professor in the Department of Chemistry at Jadavpur University, for his support and insightful discussions at the beginning of my research. My sincere thanks go to Dr. Koustav Das, Associate Professor in the Department of Physics at Jadavpur University, for granting me access to his laboratory and instruments during my work.

I owe much to my peers for their assistance and support. Special thanks to Dr. Dipankar Sahoo, Dr. S. Sen, Miss S. Rakshit, Dr. S. Bhunia, Dr. P. Das, C. Sarkar, and N. Mondal for their help with measurements and engaging discussions. I am equally grateful to research scholars B. Jana, P. Sengupta, and M. Pramanik for their assistance with data analysis and discussions.

I would like to acknowledge all the members of the Jadavpur Central Library and the Physics Departmental Library, from where I sourced many scientific references for my dissertation. I also appreciate the support from the Central Instrumental Facility of the Department of Physics, Jadavpur University, which allowed me to conduct various measurements, including FESEM, XRD, TEM, UV-Visible spectroscopy, and FTIR.

I am thankful for the financial assistance provided by the Swami Vivekananda Merit-cum-means fellowship. The electrical and optical measurements were carried out in our laboratory, with most instruments and chemicals procured through a research project funded by RUSA 2.0. I acknowledge and thank you for the financial support.

I want to express my deepest gratitude to my family for their unwavering support and encouragement. Their inspiration made this work possible, and I am profoundly grateful for their presence and sacrifices during my research.

Finally, I would like to express my heartfelt appreciation to my closest friend. Your unwavering presence has been an incredible pillar of support throughout the years. Your constant encouragement and boundless inspiration have been an enduring source of motivation, propelling me forward on this journey. Your steadfast belief in me never wavered, and for that, I am truly thankful.

Jadavpur University
Kolkata
2025

Arnab Kanti Karan

List of Abbreviations

Al	Aluminium
ϕ_b	Barrier height
BHI	Barrier Height Inhomogeneity
C-V-F	Capacitance-Voltage-Frequency Characteristics
CNT	Carbon nanotube
COOH	Carboxylic acid functionalized
N_D	Concentration of donor atoms
Cu	Copper
I-V-T	Current-Voltage-Temperature characteristics
DMSO	Dimethyl sulfoxide
DMF	Dimethylformamide
ETL	Electron transport layer
σ	Electrical conductivity
E_F	Activation energy
HOMO	Highest occupied molecular orbital
HTL	Hole transport layer
η	Ideality factor
ITO	Indium tin oxides
LED	Light emitting diode
LUMO	Lowest unoccupied molecular orbital
M/S	Metal semiconductor contact
MWCNT	Multi walled carbon nanotube
PD	Photodiode
R_s	Series resistance
SWCNT	Single walled carbon nanotube
SCLC	Space charge limited current
V_{th}	Threshold voltage
TiO_2	Titanium dioxide
E_t	Trap energy

List of Tables

List of Figures

Contents

Preface

The research presented in this thesis, entitled ***"Influence of Nanoparticles and Carbon Nanotubes on Electrical Characteristics of Natural and Organic Dye-based Cell,"*** is focused on understanding and improving the electrical properties, mostly on charge injection and transport parameters in organic dye-based semiconductor devices. We have focused on the barrier height distribution, activation energy levels and hopping parameters organic dye based cells. Also, we have presented experimentally and theoretically how the incorporation of NPs and MWCNTs can affect those parameters. These parameters are primarily governed by the nature of the metal–organic semiconductor devices.

Despite considerable advances in organic electronics, there remains a lack of comprehensive studies aimed at improving charge injection by addressing the role of interfacial barrier height. This research gap has provided the impetus for the present investigation. The work was conducted under the supervision of Professor Nabin Baran Manik in the Department of Physics, Jadavpur University, Kolkata. Subsequently, the author registered for the Ph.D. program under Professor N. B. Manik's guidance.

This thesis explores the electrical characteristics of organic dye-based devices through detailed dark current-voltage (I–V) measurements. From these measurements, critical parameters associated with charge injection, such as Richardson constant, barrier height distribution, trap energy, ideality factor, depletion layer width, image-force barrier lowering, and threshold voltage, hopping parameters, activation energy levels, have been extracted and analysed. Both experimental and theoretical approaches have been employed to address key challenges associated with inefficient charge injection, aiming to improve the overall device performance.

The theoretical approach leads us to a modified equation that can be used to determine the value of the inhomogeneous barrier height of organic cells and can be related to the inhomogeneous Richardson constant. To modify the barrier inhomogeneity at the metal-organic interface, this work incorporates Titanium Dioxide (TiO_2) nanoparticles into the device architecture and found that TiO_2 nanoparticles successively reduce the inhomogeneity, thereby facilitating improved charge injection.

Furthermore, extensive studies were conducted on the effects of MWCNTs on the electrical properties of the devices. Results indicate that SWCNTs outperform MWCNTs in promoting

charge flow due to their superior conductivity and one-dimensional structure. The inclusion of CNTs led to reductions in barrier height, trap concentration, and depletion layer width, culminating in a lower device threshold voltage. These improvements are attributed to the formation of conductive percolation pathways that promote efficient charge transport and injection.

Additionally, this work investigates several synthetic organic dyes, including Sunset Yellow (SY), Brillent Blue (BB), and Carmoisine (CS) dye with and without nanomaterial additives. Dark I–V characterisation of these systems revealed significant reductions in both interfacial barrier height and trap energy. The charge injection mechanisms were further analysed using the Richardson–Schottky (R–S) thermionic emission model, incorporating the presence of trap states. The interdependence of trap energy, barrier height, and threshold voltage is thoroughly discussed.

Despite the progress achieved, charge transport in organic dye-based devices remains a complex phenomenon, highly dependent on the specific material system and device architecture. There is currently no universal model that adequately describes charge injection and transport across all configurations. As such, continued research is essential for a deeper understanding of these processes. The insights gained from this work are expected to significantly contribute to the advancement of organic optoelectronic devices, particularly in the context of interface engineering, charge injection enhancement, and trap-state management through the integration of functional nanomaterials.

CHAPTER 1

Inspiration and Framework

Table of Contents

1.1 Introduction

The increasing demand for sustainable and eco-friendly electronic devices has driven significant interest in organic materials due to their cost-effectiveness, abundance, and potential for reduced environmental impact. Natural and synthetic organic dyes have emerged as promising candidates for various electronic applications, including light-emitting diodes (LEDs), photovoltaic cells (PVCs), sensors, and electrochromic devices, among others. These dyes are attractive materials for the fabrication of such devices due to their unique optical properties, such as high absorption coefficients, broad spectral range, and tunable absorption and emission wavelengths [1–7]. However, the inherent challenges in the conductivity and electrical performance of these materials require further exploration and improvement. Key factors contributing to these challenges include a sufficiently high Richardson constant, uneven barrier height distribution, elevated activation energy, long polaron hopping distances, and high polaron binding energy, which hold significant potential for optimisation [8–20].

The Richardson constant (A*) is a material-specific parameter that influences electron emission from metal to semiconductor in metal-organic dye contacts, where the dye acts as the semiconductor [21,22]. It significantly impacts conductivity by determining electron injection efficiency. In metal-dye interfaces, electron flow occurs if there's a Fermi level difference. This process is vital for devices like solar cells and LEDs. A higher Richardson constant can improve electron injection. Factors such as the metal's work function, dye energy levels, and interface structure affect this process. Higher doping in the dye can offset recombination effects, enhancing conductivity even with a higher Richardson constant.

In another way, in metal-organic contacts, the barrier distribution refers to the variation in the energy barrier height at the interface between the metal and the organic material. It can be caused by various factors, such as variations in the surface roughness of the metal and the organic material or the presence of impurities at the interface [23–26]. An inhomogeneous barrier distribution, where the barrier height varies over a range of values, can cause low conductivity in the metal-organic contact. When the barrier height is high in certain regions of the interface, it becomes difficult for charge carriers to cross that region, resulting in low conductivity. This can be particularly problematic when the interface is large, as the inhomogeneous distribution of barriers can lead to the formation of current bottlenecks.

Again, in metal-organic contacts, activation energy is the energy required for charge carriers to overcome a barrier and move through the interface. When the activation energy is high, it

becomes difficult for charge carriers to move through the interface, resulting in low conductivity [27,28]. The high activation energy can be caused by various factors such as differences in the electronic properties of the metal and the organic material, variations in the interface structure, or impurities at the interface. Additionally, the high activation energy can also be attributed to the presence of traps or defects in the materials, which can trap the charge carriers and inhibit their movement.

Also, Polaron binding energy and hopping length significantly influence the conductivity of organic dye-based cells. High polaron binding energy stabilises the polaron, trapping electrons and hindering their mobility, which reduces conductivity as fewer charge carriers are available for current flow [29]. Conversely, lower binding energy allows easier electron release, enhancing conductivity. The polaron hopping length, the distance a polaron can travel before losing coherence, also plays a crucial role [30]. Short hopping lengths restrict polaron movement, limiting electron transport and decreasing conductivity. However, excessively long hopping lengths increase the likelihood of polaron decay into separate electrons and lattice vibrations, disrupting charge flow and similarly reducing conductivity. Thus, optimising both binding energy and hopping length is essential for improving the efficiency of organic dye-based cells.

One promising approach to improving the performance of organic dye-based devices is the incorporation of nanomaterials such as nanoparticles and carbon nanotubes (CNTs). These nanostructures are known for their exceptional electrical, mechanical, and thermal properties, which can significantly influence the charge transport mechanisms and overall device performance [31–36]. By integrating nanoparticles and CNTs into organic dye matrices, it is possible to enhance the conductivity, reduce charge trapping, and improve the stability and efficiency of the devices [37–39]. This thesis focuses on the investigation of the influence of nanoparticles and carbon nanotubes on the conductivity and electrical characteristics of devices based on natural and synthetic organic dyes. This research is motivated by the potential to develop advanced, sustainable electronic devices with superior performance. This study aims to explore how different types of nanoparticles and CNTs affect the electrical properties of organic dye-based devices and identify optimal combinations for enhanced device functionality. The effects of various nanoparticles and nanotubes, such as Zinc Oxide (ZnO) nanoparticles, Titanium Dioxide (TiO_2) nanoparticles, Single-Walled Carbon Nanotubes (SWCNT) and Multi-Walled Carbon Nanotubes (MWCNT) on the above-discussed parameter have been studied in detail.

1.2 Objective of Our Work

The primary aim of our study is to explore and modify the Richardson constant (A^*), Barrier-Height Inhomogeneity (BHI), Activation Energy (E_F), Polaron Hopping Parameters in metal/organic (M/O) junctions. Additionally, we seek to examine the influence of different nanoparticles and nanotubes on these factors in various organic dye-based devices. The charge injection process at the junction is primarily governed by the A^* and BHI, while the charge transport process within the device is controlled by E_F and polaron hopping parameters, such as hopping length and binding energy. To evaluate these parameters, the steady-state current-voltage (I-V) characteristics of the organic devices will be analysed. This will include the assessment of electrical parameters such as trap energy, depletion layer width, image force barrier lowering, and barrier inhomogeneities in the presence and absence of nanoparticles and nanotubes, allowing for an in-depth analysis. For our experiments, we selected synthetic organic dyes including Sunset Yellow (SY), Brilliant Blue (BB), Carmoisine (CS), and Tartrazine (TZ). To study the impact of nanoparticles and nanotubes, materials such as ZnO, TiO_2, multi-walled carbon nanotubes (MWCNT), and single-walled carbon nanotubes (SWCNT) were incorporated as guest materials.

Furthermore, we aimed to understand the charge injection mechanism at the metal-organic interface. Relevant literature on charge injection and entrapment at Metal-Organic (M/O) interfaces has been thoroughly reviewed, and the role of various nanoparticles and nanotubes in dye-based organic devices has been investigated. The dye/polymer solution was typically applied using a spin-coating process at room temperature, with no significant barriers to device fabrication or film deposition. By studying the factors influencing the injection process, the findings of this research will help address different challenges associated with charge infusion at the M/O interface. This work will also contribute to advancing the application of device physics for nanoparticles and nanotubes in the field of organic electronics.

1.3 History: Chronological Development

The development of organic electronics began in the early 20th century, with the discovery of organic semiconductors like anthracene and polypyrene. However, significant progress occurred in the 1970s when researchers discovered that polyacetylene could conduct electricity when doped with iodine, leading to the Nobel Prize in Chemistry in 2000 [32]. In the 1980s and 1990s, breakthroughs in organic light-emitting diodes (OLEDs) and organic field-effect transistors (OFETs) expanded the potential applications of organic materials in electronics

[36]. In the 2000s, there was a rapid advancement in flexible, printable electronics and organic photovoltaics (OPVs), driven by improved materials and fabrication techniques. Today, organic electronics play a vital role in next-generation technologies such as foldable displays, wearable devices, and sustainable energy solutions.

1.3.1 Organic dye-based electronics

The development of organic dye-based metal-organic (M/O) contact cells has progressed significantly since the 1950s, beginning with the discovery of organic semiconductors like polycyclic aromatic hydrocarbons. In the 1960s and 1970s, dyes such as phthalocyanines and porphyrins gained attention for their semiconducting and light-absorbing properties [40,41]. The 1980s introduced dye-sensitised systems, notably with ruthenium complexes, while studies in 1988 highlighted the importance of charge injection at M/O interfaces. A breakthrough came in 1991 with Grätzel and O'Regan's Dye-Sensitised Solar Cell (DSSC), inspiring research into dye-based solid-state junctions [42]. By the late 1990s, materials like ZnO and TiO_2 were incorporated to enhance charge transport [43–46]. The 2000s focused on optimising parameters like the Richardson constant and barrier height inhomogeneities, with nanoparticles and nanotubes improving charge mobility. The 2010s brought advancements in nanotechnology and scalable film deposition techniques, while the 2020s have emphasised environmentally friendly dyes, advanced characterisation, and multi-functional device applications, marking a new era in organic electronics.

1.3.2 Richardson constant (A*)

The Richardson constant (A*), originally introduced in 1901 by Owen Willans Richardson as part of thermionic emission theory, has become a key parameter in understanding charge injection in organic dye-based cells. Early developments in the mid-20th century applied the Richardson-Schottky equation to semiconductors, providing a foundation for studying metal-organic (M/O) interfaces [47–49]. In the 1980s, as organic electronics gained momentum, the Richardson constant was adapted to account for the unique properties of organic materials, such as molecular structure and barrier inhomogeneities [50,51]. By the 1990s, the advent of dye-sensitised solar cells (DSSCs) and research into dye-based devices highlighted A*'s role in governing electron injection efficiency.

1.3.3 Activation Energy (E_F)

The concept of activation energy (E_F) has been pivotal in understanding charge transport in organic dye-based cells, evolving alongside advancements in organic electronics [52]. In the

1950s and 1960s, early studies on organic semiconductors identified activation energy as a critical factor in overcoming energy barriers for charge carriers [53]. By the 1980s, with the rise of dye-sensitised systems, activation energy became central to analysing electron transfer processes at metal-organic (M/O) interfaces, particularly for organic dyes like phthalocyanines and porphyrins. The introduction of dye-sensitised solar cells (DSSCs) in 1991 further emphasised the role of E_F in facilitating photo-induced electron transfer, inspiring deeper studies into its impact on charge injection and transport. During the 2000s, the integration of nanomaterials such as ZnO and TiO_2 revealed how activation energy could be tailored to improve charge mobility and reduce recombination losses. In the 2010s, there was an advancement in understanding polaron hopping mechanisms, linking E_F to hopping length and binding energy, while advanced characterisation techniques like impedance spectroscopy and I-V analysis further refined its measurement.

1.3.4 Barrier Height Inhomogeneity (BHI)

The concept of barrier height inhomogeneity (BHI) has been pivotal in understanding charge transport mechanisms in organic dye-based electronics. Early studies on metal-semiconductor interfaces revealed that variations in the Schottky barrier height could significantly influence device performance. For instance, research on Au/n-Si Schottky barrier diodes with organic interfacial layers demonstrated that inhomogeneities in barrier height could affect the electrical characteristics of the devices [54]. Further investigations into Schottky barrier inhomogeneities at different epitaxial interfaces highlighted the impact of these variations on charge injection and transport processes [55,56]. These findings underscore the importance of considering BHI in the design and optimisation of organic dye-based electronic devices, as it plays a crucial role in determining their efficiency and stability.

1.3.5 Polaron Hopping

The concept of polaron hopping is an integral part of understanding charge transport in organic dye-based electronics. In the 1950s, researchers began exploring the electrical properties of organic materials, leading to the discovery of charge transfer complexes that exhibited semiconducting behaviour. This period marked the initial recognition of charge carriers in organic systems, laying the groundwork for future studies on polaron dynamics. In the 1980s, significant advancements in the development of conductive polymers, where the role of polarons—quasi-particles formed by electrons coupled with local lattice distortions—became more evident. Studies during this time highlighted the importance of polaron hopping mechanisms in facilitating charge transport within these materials. As research progressed, the

focus shifted towards understanding the parameters influencing polaron hopping, such as hopping distance and activation energy, to optimise the performance of organic electronic devices. Recent studies have delved deeper into the modelling of polaron transport, providing insights into how these mechanisms can be manipulated to enhance the efficiency of organic dye-based electronics [10,29,30,57].

1.4 Outline of the work

The main intention of our work is to investigate the above-discussed parameters for some selected dyes and make a comparison of them in the presence of nanoparticles and nanotubes. For this case, as stated above, we have selected some synthetic dyes like SY, CS, TZ and BB, and some guest nanoparticles like ZnO, TiO_2, MWCNT and SWCNT in our study. For a step-by-step discussion, we have divided our thesis into seven chapters.

In Chapter 1, we have discussed the parameters that are the cause of low conductivity for organic dye-based cells. Also, we have elaborated on the historical background of the parameters.

In Chapter 2, we review the conductivity and semiconducting properties of organic dye-based cells, including the challenges to apply them in electronic and optoelectronic devices with these dyes. Also, we have discussed on the role of nanoparticles and nanotubes on the semiconducting parameters. A detailed theoretical understanding has been elaborated in this chapter.

In Chapter 3, we experimented and showed how the incorporation of TiO_2 nanoparticles affects the inhomogeneous distribution of barrier height at the interface of the Brillent-Blue dye-based cell. Also, we have correlated how the modification of BHI can increase the overall conductivity as well as the semiconducting property of the cell.

In Chapter 4, we have analysed how the discrepancy in the activation energy can affect the overall conductivity of the organic dye-based cell. To do that, we have used Sunset-Yellow dye as the active material. Also, we have analysed how the incorporation of ZnO nanoparticles can modify the activation energy level and overall conductivity of the cell. Additionally, we have extracted different charge conduction and injection parameters with a comparison between dye with and without nanoparticles.

In Chapter 5, we have shown how the incorporation of MWCNT can affect the polaron hopping mechanism. To do that, we have used Carnosine dye-based organic cells. In this chapter, we explained the cause of the modification of the polaron hopping mechanism by the incorporation of MWCNT.

In Chapter 6, we have discussed the conclusion and future scope of our work.

1.5 Reference

[1] D. Pinjari, Y. Patil, R. Misra, Near-Infrared Absorbing Aza-BODIPY Dyes for Optoelectronic Applications, Chem Asian J 19 (2024). https://doi.org/10.1002/asia.202400167.

[2] F. D'Amico, B. de Jong, M. Bartolini, D. Franchi, A. Dessì, L. Zani, X. Yzeiri, E. Gatto, A. Santucci, A. Di Carlo, G. Reginato, L. Cinà, L. Vesce, Recent Advances in Organic Dyes for Application in Dye-Sensitized Solar Cells under Indoor Lighting Conditions, Materials 16 (2023). https://doi.org/10.3390/ma16237338.

[3] Q. Zhang, W. Hu, H. Sirringhaus, K. Müllen, Recent Progress in Emerging Organic Semiconductors, Advanced Materials 34 (2022). https://doi.org/10.1002/adma.202108701.

[4] S.R. Forrest, The path to ubiquitous and low-cost organic electronic appliances on plastic, 2004. www.nature.com/nature.

[5] A. Dessì, M. Calamante, A. Mordini, M. Peruzzini, A. Sinicropi, R. Basosi, F. Fabrizi De Biani, M. Taddei, D. Colonna, A. Di Car, G. Reginato, L. Zani, Organic dyes with intense light absorption especially suitable for application in thin-layer dye-sensitized solar cells, Chemical Communications 50 (2014) 13952–13955. https://doi.org/10.1039/c4cc06160h.

[6] Y. Li, X. Li, J. Qi, Y. Xu, Tunable optoelectronic properties of D-A-π-A type dyes by altering auxiliary acceptor position and atomic electronegativity, J Mol Liq 287 (2019). https://doi.org/10.1016/j.molliq.2019.110883.

[7] S.G. Stenspil, B.W. Laursen, Photophysics of fluorescent nanoparticles based on organic dyes - challenges and design principles, Chem Sci 15 (2024) 8625–8638. https://doi.org/10.1039/d4sc01352b.

[8] C.J. Taylor, A. Pomberger, K.C. Felton, R. Grainger, M. Barecka, T.W. Chamberlain, R.A. Bourne, C.N. Johnson, A.A. Lapkin, A Brief Introduction to Chemical Reaction Optimization, Chem Rev 123 (2023) 3089–3126. https://doi.org/10.1021/acs.chemrev.2c00798.

[9] A.B. Muñoz-García, I. Benesperi, G. Boschloo, J.J. Concepcion, J.H. Delcamp, E.A. Gibson, G.J. Meyer, M. Pavone, H. Pettersson, A. Hagfeldt, M. Freitag, Dye-sensitized solar cells strike back, Chem Soc Rev 50 (2021) 12450–12550. https://doi.org/10.1039/d0cs01336f.

[10] K. Morita, M.J. Golomb, M. Rivera, A. Walsh, Models of Polaron Transport in Inorganic and Hybrid Organic-Inorganic Titanium Oxides, Chemistry of Materials 35 (2023) 3652–3659. https://doi.org/10.1021/acs.chemmater.3c00322.

[11] J. Li, M. Bouchard, P. Reiss, D. Aldakov, S. Pouget, R. Demadrille, C. Aumaitre, B. Frick, D. Djurado, M. Rossi, P. Rinke, Activation Energy of Organic Cation Rotation in CH3NH3PbI3 and CD3NH3PbI3: Quasi-Elastic Neutron Scattering Measurements

and First-Principles Analysis Including Nuclear Quantum Effects, Journal of Physical Chemistry Letters 9 (2018) 3969–3977. https://doi.org/10.1021/acs.jpclett.8b01321.

[12] D.B. Go, J.R. Haase, J. George, J. Mannhart, R. Wanke, A. Nojeh, R. Nemanich, Thermionic Energy Conversion in the Twenty-first Century: Advances and Opportunities for Space and Terrestrial Applications, Front Mech Eng 3 (2017). https://doi.org/10.3389/fmech.2017.00013.

[13] C.P. Lee, C.T. Li, K.C. Ho, Use of organic materials in dye-sensitized solar cells, Materials Today 20 (2017) 267–283. https://doi.org/10.1016/j.mattod.2017.01.012.

[14] M. Sharma, S.K. Tripathi, Study of barrier inhomogeneities in I-V-T and C-V-T characteristics of Al/Al 2O 3/PVA:n-ZnSe metal-oxide-semiconductor diode, J Appl Phys 112 (2012). https://doi.org/10.1063/1.4737589.

[15] N. Tuğluoğlu, Ö.F. Yüksel, H. Şafak, S. Karadeniz, The double Gaussian distribution of inhomogeneous barrier heights in the organic-on-inorganic Schottky devices, Physica Status Solidi (A) Applications and Materials Science 209 (2012) 2313–2316. https://doi.org/10.1002/pssa.201228163.

[16] B.H. Moon, G.H. Han, H. Kim, H. Choi, J.J. Bae, J. Kim, Y. Jin, H.Y. Jeong, M.K. Joo, Y.H. Lee, S.C. Lim, Junction-Structure-Dependent Schottky Barrier Inhomogeneity and Device Ideality of Monolayer MoS2 Field-Effect Transistors, ACS Appl Mater Interfaces 9 (2017) 11240–11246. https://doi.org/10.1021/acsami.6b16692.

[17] N. Jiang, T. Sumitomo, T. Lee, A. Pellaroque, O. Bellon, D. Milliken, H. Desilvestro, High temperature stability of dye solar cells, Solar Energy Materials and Solar Cells 119 (2013) 36–50. https://doi.org/10.1016/j.solmat.2013.04.017.

[18] M. Ben Bechir, F. Alresheedi, Interpretation of dielectric behavior and polaron hopping in lead-free antimony-based double perovskite, RSC Adv 13 (2023) 34703–34714. https://doi.org/10.1039/d3ra05857c.

[19] I. Jahangir, M.A. Uddin, A.K. Singh, G. Koley, M.V.S. Chandrashekhar, Richardson constant and electrostatics in transfer-free CVD grown few-layer MoS2/graphene barristor with Schottky barrier modulation >0.6eV, Appl Phys Lett 111 (2017). https://doi.org/10.1063/1.5005796.

[20] A.A.M. Farag, I.S. Yahia, Rectification and barrier height inhomogeneous in Rhodamine B based organic Schottky diode, Synth Met 161 (2011) 32–39. https://doi.org/10.1016/j.synthmet.2010.10.030.

[21] C.P.Y. Wong, C. Troadec, A.T.S. Wee, K.E.J. Goh, Gaussian Thermionic Emission Model for Analysis of Au/Mo S2 Schottky-Barrier Devices, Phys Rev Appl 14 (2020). https://doi.org/10.1103/PhysRevApplied.14.054027.

[22] Ş. Çavdar, P. Oruç, S. Eymur, N. Tuğluoğlu, Investigation of photosensitive and photodetector characteristics of n-TPA-IFA/p-Si heterojunction structure, Journal of

Materials Science: Materials in Electronics 35 (2024). https://doi.org/10.1007/s10854-024-12749-4.

[23] H.T. Chien, M. Pölzl, G. Koller, S. Challinger, C. Fairbairn, I. Baikie, M. Kratzer, C. Teichert, B. Friedel, Effects of hole-transport layer homogeneity in organic solar cells – A multi-length scale study, Surfaces and Interfaces 6 (2017) 72–80. https://doi.org/10.1016/j.surfin.2016.11.008.

[24] K. Sunahara, A. Furube, R. Katoh, S. Mori, M.J. Griffith, G.G. Wallace, P. Wagner, D.L. Officer, A.J. Mozer, Coexistence of femtosecond- and nonelectron-injecting dyes in dye-sensitized solar cells: Inhomogeniety limits the efficiency, Journal of Physical Chemistry C 115 (2011) 22084–22088. https://doi.org/10.1021/jp2093109.

[25] S. Sen, P.K. Das, N.B. Manik, Study on the effect of singlewalled carbon nanotubes on junction properties of safranin –t dye-based organic device, J Phys Commun 5 (2021). https://doi.org/10.1088/2399-6528/ABF2CF.

[26] J.E. Kroeze, N. Hirata, S. Koops, M.K. Nazeeruddin, L. Schmidt-Mende, M. Grätzel, J.R. Durrant, Alkyl chain barriers for kinetic optimization in dye-sensitized solar cells, J Am Chem Soc 128 (2006) 16376–16383. https://doi.org/10.1021/ja065653f.

[27] P.P. Kumavat, P. Sonar, D.S. Dalal, An overview on basics of organic and dye sensitized solar cells, their mechanism and recent improvements, Renewable and Sustainable Energy Reviews 78 (2017) 1262–1287. https://doi.org/10.1016/j.rser.2017.05.011.

[28] D. Joly, L. Pellejà, S. Narbey, F. Oswald, J. Chiron, J.N. Clifford, E. Palomares, R. Demadrille, A robust organic dye for dye sensitized solar cells based on iodine/iodide electrolytes combining high efficiency and outstanding stability, Sci Rep 4 (2014). https://doi.org/10.1038/srep04033.

[29] R. Ghosh, F.C. Spano, Excitons and Polarons in Organic Materials, Acc Chem Res 53 (2020) 2201–2211. https://doi.org/10.1021/acs.accounts.0c00349.

[30] R. Karsthof, M. Grundmann, A.M. Anton, F. Kremer, Polaronic interacceptor hopping transport in intrinsically doped nickel oxide, Phys Rev B 99 (2019). https://doi.org/10.1103/PhysRevB.99.235201.

[31] P. Naphon, S. Wiriyasart, N. Naphon, Thermal, mechanical, and electrical properties of rubber latex with TiO2 nanoparticles, Composites Communications 22 (2020). https://doi.org/10.1016/j.coco.2020.100449.

[32] T. Gao, B.P. Jelle, Thermal conductivity of TiO2 nanotubes, Journal of Physical Chemistry C 117 (2013) 1401–1408. https://doi.org/10.1021/jp3108655.

[33] E. Laudadio, E. Mohebbi, E. Pavoni, C. Minnelli, S. Sabbatini, P. Stipa, Density functional theory and molecular dynamics studies on electrical, mechanical, and thermal properties of TiO2 nanoparticles interacting with poly lactic-co-glycolic acid, Colloids Surf A Physicochem Eng Asp 667 (2023). https://doi.org/10.1016/j.colsurfa.2023.131388.

[34] Z. Meng, T. Zhang, Q. Chi, C. Zhang, C. Tang, H. Li, Q. Lei, Electrical, mechanical and thermal properties of ZnO/SiR composite dielectric, Journal of Materials Science: Materials in Electronics 32 (2021) 17253–17265. https://doi.org/10.1007/s10854-021-06204-x.

[35] K. Kumar, P.K. Ghosh, A. Kumar, Improving mechanical and thermal properties of TiO2-epoxy nanocomposite, Compos B Eng 97 (2016) 353–360. https://doi.org/10.1016/j.compositesb.2016.04.080.

[36] R.S. Ruoff, D.C. Lorents, MECHANICAL AND THERMAL PROPERTIES OF CARBON NANOTUBES, 1995.

[37] M. Hosni, Y. Kusumawati, S. Farhat, N. Jouini, T. Pauporté, Effects of oxide nanoparticle size and shape on electronic structure, charge transport, and recombination in dye-sensitized solar cell photoelectrodes, Journal of Physical Chemistry C 118 (2014) 16791–16798. https://doi.org/10.1021/jp412772b.

[38] S. Singh, A. Singh, N. Kaur, Efficiency Investigations of Organic/Inorganic Hybrid ZnO Nanoparticles Based Dye-Sensitized Solar Cells, J Mater 2016 (2016) 1–11. https://doi.org/10.1155/2016/9081346.

[39] D. Maheswari, P. Venkatachalam, Enhancing the performance of dye-sensitized solar cells based on organic dye sensitized TiO2 nanoparticles/nanowires composite photoanodes with ionic liquid electrolyte, Measurement (Lond) 60 (2015) 146–154. https://doi.org/10.1016/j.measurement.2014.10.016.

[40] J.E. Anthony, Functionalized acenes and heteroacenes for organic electronics, Chem Rev 106 (2006) 5028–5048. https://doi.org/10.1021/cr050966z.

[41] K.-Y. Law, Organic Photoconductive Materials: Recent Trends and Developments, 1993. https://pubs.acs.org/sharingguidelines.

[42] M. Grätzel, Dye-sensitized solar cells, Journal of Photochemistry and Photobiology C: Photochemistry Reviews 4 (2003) 145–153. https://doi.org/10.1016/S1389-5567(03)00026-1.

[43] V.L. Devi, D. De, P. Kuchhal, R.K. Pachauri, Photovoltaic performance of TiO2 and ZnO nanostructures in anthocyanin dye-sensitized solar cells, Clean Energy 8 (2024) 144–156. https://doi.org/10.1093/ce/zkae059.

[44] G.S. Selopal, H.P. Wu, J. Lu, Y.C. Chang, M. Wang, A. Vomiero, I. Concina, E.W.G. Diau, Metal-free organic dyes for TiO2 and ZnO dye-sensitized solar cells, Sci Rep 6 (2016). https://doi.org/10.1038/srep18756.

[45] D. Sinha, D. De, D. Goswami, A. Mondal, A. Ayaz, ScienceDirect ZnO and TiO 2 Nanostructured Dye sensitized Solar Photovoltaic Cell Selection and peer-review under responsibility of Conference Committee of the 2 nd International Conference on Emerging Materials: Characterisation and Application (EMCA-2017), n.d. www.sciencedirect.com.

[46] B. Levy, Photochemistry of Nanostructured Materials for Energy Applications, Kluwer Academic Publishers, 1997.

[47] J.R. Nimmo, New insights on the origin of the Richardson-Richards equation, Hydrological Sciences Journal (2024). https://doi.org/10.1080/02626667.2024.2404714.

[48] S.J. Pilkington, M. Missous, D.A. Woolf, On the Richardson constant of intimate metal-GaAs (111)B Schottky diodes grown by molecular beam epitaxy, J Appl Phys 74 (1993) 6256–6260. https://doi.org/10.1063/1.355169.

[49] C.R. Crowbll, THE RICHARDSON CONSTANT FOR THERMIONIC EMISSION IN SCHOTTKY BARRIER DIODES, 1965.

[50] J. Weippert, P. Reinke, F. Benkhelifa, H. Czap, C. Giese, L. Kirste, P. Straňák, J. Kustermann, J. Engels, V. Lebedev, Pseudovertical Schottky Diodes on Heteroepitaxially Grown Diamond, Crystals (Basel) 12 (2022). https://doi.org/10.3390/cryst12111626.

[51] A.F. Paterson, S. Singh, K.J. Fallon, T. Hodsden, Y. Han, B.C. Schroeder, H. Bronstein, M. Heeney, I. McCulloch, T.D. Anthopoulos, Recent Progress in High-Mobility Organic Transistors: A Reality Check, Advanced Materials 30 (2018). https://doi.org/10.1002/adma.201801079.

[52] H. Om Y A D A V, Relation between the activation energy of the electrical conduction in organic semiconductors and their first excited singlet state energies, 1991.

[53] C.N. Hinshelwood, K.J. Laidler, E.W. TIMM, jr9380000848, Journal of Chemical Society (1938) 848–858. https://doi.org/https://doi.org/10.1039/JR9380000848.

[54] I. Taşçoğlu, U. Aydemir, Ş. Altndal, The explanation of barrier height inhomogeneities in Au/n-Si Schottky barrier diodes with organic thin interfacial layer, J Appl Phys 108 (2010). https://doi.org/10.1063/1.3468376.

[55] J.H. Werner, H.H. Güttler, Barrier inhomogeneities at Schottky contacts, J Appl Phys 69 (1991) 1522–1533. https://doi.org/10.1063/1.347243.

[56] H. Cetin, B. Şahin, E. Ayyildiz, A. Türüt, The barrier-height inhomogeneity in identically prepared H-terminated Ti/p-Si Schottky barrier diodes, Semicond Sci Technol 19 (2004) 1113–1116. https://doi.org/10.1088/0268-1242/19/9/007.

CHAPTER 2

Theoretical Framework

Table of Content

2.1 Introduction

In the previous chapter, we outlined the context and objectives of our current research. It also presented the framework for the thesis and discussed its potential outcomes. This chapter will delve into the fundamental operating principles of organic devices, covering the various models and factors about the problems outlined in the previous chapter. Additionally, the properties of the nanoparticles to be integrated into these organic dye-based devices will be discussed in detail.

2.2 Conductivity in Organic Dye-Based Cells

Since 1990, organic dye-based devices have garnered significant attention from researchers. These devices are made from very thin layers, and since most organic semiconductors are p-type with a relatively high optical band gap, production costs are reduced [1,2]. Organic materials consist of π-bonded electrons in sp^2-hybridized carbon atoms, which can move through delocalized π-orbitals [3]. In our study, we created an M/O contact in the prepared organic device. The work function of the metal electrode, along with the Lowest Unoccupied Molecular Orbital (LUMO) and Highest Occupied Molecular Orbital (HOMO) energy levels of the organic materials, remain unchanged prior to establishing the M/O contact. Once the M/O contact is formed, the energy levels align. If the work function of the metal electrode is higher than the LUMO energy level of the organic materials, electrons will flow from the metal electrode to the organic materials. Conversely, if the work function of the metal electrode is lower than the LUMO energy level, electrons will move from the organic materials to the metal electrode [4–6]. This movement generates an electric field from the organic materials to the metal electrode. As the electrons travel from the organic materials to the metal electrode, they will face an energy barrier due to the electric field [7,8].

There are very few research reports available about the conductivity of natural organic dyes like Curcumin, Hibiscus Rosasinesis, Sesbania Grandiflora, and Indigo-Tyrian Purple that show that the natural dyes can be used as organic semiconductors [9–16]. The indigoids show stable p-type operation in the air with a high-lying LUMO level (−3.8 eV) [10]. Indigo shows balanced electron and hole mobilities of 1×10^{-2} $cm^2\ V^{-1}s^{-1}$ and good stability against degradation in air, and fabricated natural and biodegradable devices show the large potential for organic electronics [11]. Recent work has shown the possibility of employing inexpensive biodegradable polymers and natural semiconducting and insulating materials in electronic

devices [12]. The natural pigment Tyrian Purple, 6,6'-dibromoindigo, is an ambipolar organic semiconductor with large electron and hole mobilities. The LUMO level of Tyrian purple is deeper, however, at −4.0 eV, and devices could be operated stably in the air for both p- and n-channels for at least 30 minutes with repeated cycling [13]. β−carotene, a natural dye, behaves as a p-type semiconductor with a hole mobility of 4×10^{-4} $cm^2/ V\cdot s$ [14]. Commercial textile dyes based on anthraquinone represent two available vat dyes, Yellow 1 and Orange 3, both of which are wide-bandgap semiconductors with high electron affinity (LUMO level ~ -3.6 to -3.8 eV) and high oxidation potential [17]. The conductivity of an organic dye-based Schottky cell has been controlled by a 2-step process, charge injection and charge transport process. The following are examples of injection-limited transports or electrode-limited conduction mechanisms: Direct tunnelling, Fowler-Nordheim (F-N) tunnelling, and Schottky emission. Poole-Frenkel (P-F) emission, Ohmic conduction, Space Charge Limited Transport (SCLC), Hopping conduction, Trap-assisted tunnelling (TAT), and Ohmic conduction are examples of bulk-limited conduction mechanisms [18–22]. In the following section, we will discuss a few of these transport models in brief, especially those that have been utilised in this work.

2.2.1 Injection Limited Transport

Injection-limited transport refers to a regime in which the interfacial properties of the electrode–semiconductor junction predominantly dictate the kinetics of charge carrier migration or diffusion. The nature of electrical conduction under this constraint is governed by the physicochemical attributes of the electrode–semiconductor interface, with the Schottky barrier height emerging as the principal determinant. The predominant modalities of electrode-limited conduction encompass (a) quantum mechanical direct tunnelling, (b) Fowler–Nordheim field-assisted tunnelling, and (c) thermionic emission over the interfacial barrier. Notably, while tunnelling-mediated currents exhibit negligible thermal dependence, thermionic emission currents are intrinsically sensitive to variations in temperature.

2.2.1.a Thermionic Emission Model

Thermionic emission denotes the process by which charge carriers, typically electrons, acquire sufficient thermal energy to surmount the potential energy barrier at the surface of a material, thereby enabling their ejection into the vacuum or an adjacent medium. This phenomenon occurs when the thermal agitation of electrons exceeds the work function of the material, facilitating their escape from the solid phase. The resultant emission of electrons significantly contributes to charge transport mechanisms and underpins the operational principles of various

vacuum-based and solid-state electronic devices. According to thermionic emission theory, the resultant current density (J_0) can be mathematically described by the Richardson-Dushman equation, which is expressed as **Equation (2.1)** [23]

$$J_0 = A^* T^2 \exp\{-e\phi/kT\} \tag{2.1}$$

Where ϕ is the barrier height and $A^* = \frac{4\pi m^{\ 2}}{h^3}$ and in which the numerical value of A^* is roughly 120 [A/ (cm^2 K^2)]. If electrons encounter an external retarding potential of height V_s above ϕ, fewer electrons will escape, resulting in a current J escaping from the cathode that is less than Jo. The derivation of Equation (2.1) applies with the utilisation of $\phi + V_s$ instead of ϕ. Thus, the above equation transforms into **Equation (2.2)**.

$$J = \frac{4\pi mek^2T^2}{h^3} \exp\{-e(\phi + V_s)/kT\} \tag{2.2}$$

where the zero-field subscript is omitted. This equation can now also be written as **Equation (2.3).**

$$J = J_0 \exp\{-eV_s/kT\} \tag{2.3}$$

where J_o is given by Equation (2.1). Upon application of bias across the junction the **Equation (2.1)** becomes [24,25]

$$J_0 = AT^2 \exp\{e(V_{app} - \phi_a)/kT\} \tag{2.4}$$

Where V_{app} is the applied bias and ϕ_a is the anode potential. Therefore, when an electric field is applied, the potential energy barrier at the interface is lowered, increasing the flow of current through the M-S junction. The observed increase in current flow, along with its dependence on the applied electric field, is known as the Schottky effect. According to this model, an electron can escape from a metal surface if it acquires sufficient thermal energy to overcome the potential barrier formed by the combined effects of the image charge potential and the external electric field [18]. This framework effectively describes and analyses the interfacial current flow at the junction between metal and perovskite materials. In the present thesis, we have

applied this model to investigate the current transport behaviour in the fabricated perovskite-based optoelectronic devices.

2.2.1.b Direct tunneling model (DTM)

The Direct Tunnelling Mechanism (DTM) arises from a quantum mechanical principle wherein, under sub-threshold bias conditions (i.e., $V < \phi_B$) electrons exhibit non-classical penetration through the potential barrier intrinsic to a metal-semiconductor-metal (MSM) junction. This process becomes dominant when the interfacial barrier, typically less than 4 nm in thickness and devoid of structural defects, permits coherent electron tunnelling across its entire spatial extent. Under such conditions, DTM governs the dominant charge transport mechanism within the MSM configuration. At cryogenic temperatures (e.g., $T < 30$ K), where thermionic emission is significantly suppressed, the current-voltage (J–V) behaviour of the device can be experimentally profiled to assess the extent of direct tunnelling. In such cases, a plot of $\ln(J/V^2)$ as a function of $1/V$ yields a linear regime under low-bias excitation (on the order of millivolts), thereby confirming tunnelling conduction. The corresponding tunnelling current density is quantified by the following **Equation (2.5)** [25,26]

$$J_{DT} = J_0\left[\left\{\phi_B \exp\left(-A_s\sqrt{\phi_B}\right)\right\} - \left\{(\phi_B + V)\exp\left(-A_s\sqrt{\phi_B + V}\right)\right\}\right] \quad (2.5)$$

Where $J_0 = \frac{q^2}{2\pi h d_i^2}$ and $A_s = \frac{4\pi d_i\sqrt{2qm^*}}{h}$, d_i is the thickness of the sample film. Equation (2.5) can be understood as a current density, just as the Schottky Emission current density $J_0\left[\phi_B \exp\left(-A_s\sqrt{\phi_B}\right)\right]$ flowing from metal-1 to metal-2, and another $J_0\left[(\phi_B + V)\exp\left(-A_s\sqrt{\phi_B + V}\right)\right]$ flowing from metal-2 to metal-1.

2.2.2 Bulk-Limited Transport

Bulk-limited transport refers to a charge transport mechanism in semiconductors where the inherent properties of the material itself primarily govern the movement of charge carriers. Unlike interface-limited transport, which is influenced by the characteristics of material interfaces, bulk-limited transport focuses on the behaviour within the interior (bulk) of the Semiconductor. This mechanism is fundamental to the design and performance of various semiconductor devices, including integrated circuits, diodes, transistors, and solar cells. A thorough understanding of how charge carriers move through the bulk of the material is essential for optimising device efficiency and functionality. In bulk-limited conduction, the electrical behaviour is determined by the intrinsic properties of the semiconductor layer. Among these, the trap energy levels play a critical role in influencing charge transport [27,28].

Common mechanisms associated with bulk-limited conduction include Poole–Frenkel emission, hopping conduction, ohmic conduction, space charge-limited conduction (SCLC), and trap-assisted tunnelling. By analysing these mechanisms, key electrical parameters of the semiconductor films—such as trap energy levels, trap spacing, trap density, carrier mobility, dielectric relaxation time, and the density of states in the conduction band—can be extracted and evaluated.

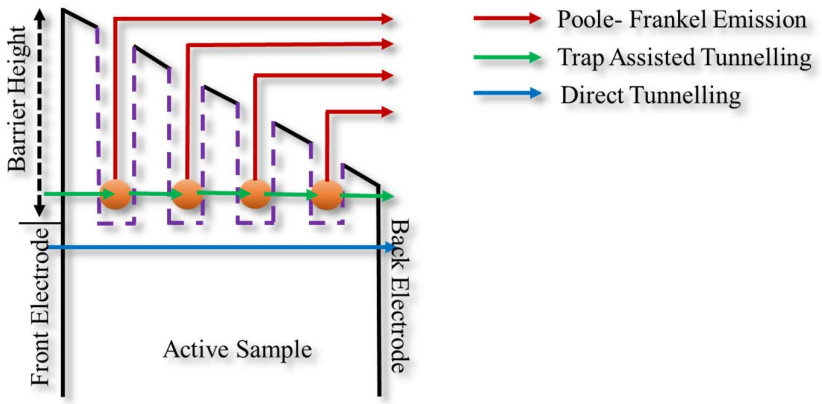

Figure 2.1: Schematic diagram of several transport mechanisms in a metal-sample (semiconductor)-metal structure.

2.2.2.a Hopping Conduction

The tunnelling effect of trapped electrons "hopping" from one trap site to another in semiconductor films is the cause of hopping conduction. The schematic energy band map for hopping conduction is displayed in **Figure 2.1**. Hoping that conduction can be expressed as **Equation (2.6)** [20]

$$J = qanf \exp\left[\frac{qaE - E_a}{kT}\right] \tag{2.6}$$

where f is the frequency of thermal vibration of electrons at trap sites, n is the electron concentration in the semiconductor's conduction band, a is the mean hopping distance (i.e., the mean spacing between trap sites), and E_a is the activation energy-that is, the energy level from the trap states to the bottom of the conduction band (E_C).

2.2.2.b Ohmic conduction

In the conduction regime, the current density exhibits a direct proportionality to the applied electric field, characterising a linear transport behaviour. Despite the relatively wider energy bandgap inherent to certain perovskite semiconductors when compared to silicon, thermal excitation processes can still generate a limited population of charge carriers. These thermally activated carriers may arise either through valence band to conduction band transitions or via excitation from impurity or defect states within the forbidden energy gap. While the carrier concentration remains minimal under such conditions, it is non-negligible. Ohmic conduction is thus defined by a linear current–electric field relationship, as represented by **Equation (2.7)**, and is attributed to the drift of free electrons within the conduction band and holes within the valence band. This linear I–V characteristic in Equation (2.7) is predominantly observable at low applied biases in semiconductor thin films, indicating negligible space charge effects and the dominance of intrinsic carrier dynamics.

$$J = \sigma E = ne\mu E \tag{2.7}$$

Where $n = N_C \exp\left[\frac{E_F - E_C}{kT}\right]$ and σ is electrical conductivity, n is the number of electrons in the conduction band, μ is electron mobility, and N_C It is the effective density of states of the conduction band. This current has a relatively small magnitude. This type of current mechanism can be observed when there are no substantial contributions from other modes of current transport in materials.

2.2.2.c Space charge- limited conduction

Precise evaluation of the intrinsic electronic properties of semiconducting materials is pivotal for the development and optimisation of contemporary electronic and optoelectronic systems. Among the suite of methodologies employed to probe charge transport phenomena, the space-charge limited current (SCLC) technique stands as a prominent and extensively utilised steady-state diagnostic approach. Through current density–voltage (J–V) analysis, it enables the investigation of charge carrier injection and transport dynamics for both electrons and holes. The foundational framework of this theory was introduced by C. D. Child and I. Langmuir during the early 20th century (1911–1913), wherein they described the current density (J) in vacuum diodes as being proportional to the three-halves power of the applied voltage ($J \propto V^{3/2}$) [29,30]. However, this empirical law fails to accurately represent charge transport behaviour

in solid-state devices comprising semiconducting, organic, or polymeric materials interposed between metallic contacts.

To address these discrepancies, the Mott–Gurney law was subsequently formulated, establishing a refined model applicable to trap-free semiconducting media under specific assumptions. The theoretical treatment of SCLC begins with the formulation of the one-dimensional drift current equation for a single carrier species, represented by **Equation (2.8)**, coupled with Poisson's equation, represented by **Equation (2.9)**, which governs the spatial distribution of electric potential due to space charge effects within the device structure.

$$J = n(x)q\mu E \tag{2.8}$$

$$\frac{dE}{dx} = \frac{q}{\varepsilon}n(x) \tag{2.9}$$

Here, q represents the electronic charge, μ is the electronic mobility, and n denotes the density of thermally generated background free charges. ε is the permittivity of the medium. When the density of thermally generated charge carriers (n) is significantly lower than the injected charge density (n_{inj}) and the system is free of traps, Mott-Gurney proposed an estimation for the relationship between current density (J) and applied voltage (V). They derived that in such conditions, space charge limited conduction (SCLC) follows a relationship described as **Equation (2.10)** [31]

$$J = \frac{9}{8}\mu\varepsilon\frac{V^2}{L^3} \tag{2.10}$$

Here, L denotes the physical thickness of the active layer within the device. The canonical SCLC relationship remains valid solely under the idealised condition of a trap-free medium. However, real-world materials—such as perovskite, organic, and certain inorganic semiconductors—are invariably populated with intrinsic and extrinsic trap states. Consequently, carriers injected from an ohmic contact are impeded from traversing the device instantaneously, giving rise to space-charge-limited current (SCLC). An electronic trap is broadly defined as a localised electronic defect that introduces discrete or distributed energy levels within the bandgap of a semiconductor. Such trap states in perovskite systems can arise from extrinsic impurities, intrinsic crystallographic disorder, geminate electron-hole pairs, or

polaronic self-trapping phenomena. Due to the inherently weak intermolecular interactions in perovskite frameworks, molecular orbitals such as the HOMO or LUMO may localize in the interstitial regions between adjacent host moieties, forming trap states. Variability in π-conjugation lengths, stemming from structural non-uniformities, may further engender tail states near the transport edges, significantly contributing to electronic trapping. These structural anomalies are not confined to tail state generation alone, as any defect at the molecular or crystalline scale can potentiate trap formation.

Traps are energetically classified as either shallow or deep, based on their proximity to the conduction or valence band edges relative to thermal energy (kT). Shallow traps reside within a few kT of the band edges and may transiently immobilise charge carriers, subsequently releasing them under thermal agitation, electric field perturbation, or photonic stimulation [32,33]. In models such as the Multiple-Trap-and-Release (MTR) framework, shallow localised states intermittently capture carriers from delocalized bands, which are then thermally re-emitted. In densely trap-populated systems, carrier transport may proceed via thermally-assisted hopping or quantum tunnelling among these localised trap states. By contrast, deep traps—situated several kT from the band edges—are energetically less likely to facilitate de-trapping and predominantly act as recombination centres, thereby curtailing carrier lifetimes. These trap states may manifest as discrete energy levels or conform to continuous distributions, typically modelled by Gaussian or exponential functions. The schematic in **Figure 2.2** graphically delineates the energetic distribution of such traps within the semiconductor's bandgap. For our analysis, we have only considered the discrete and the exponential distribution of traps. In this case drift current equation, as mentioned in Equation (2.8) is remains the same, but the Poisson equation is represented by **Equations (2.11)**.

$$\frac{dE}{dx} = \frac{q}{\epsilon}(n + n_t) \tag{2.11}$$

Where n and n_t are the concentrations of free and trapped charges, respectively. The following scenarios can be obtained using the preceding equations. At low voltages, it is often observed that ohmic conduction with low mobility dominates via thermally generated free charges over injected charge contributions. In this scenario, the current density J is described by

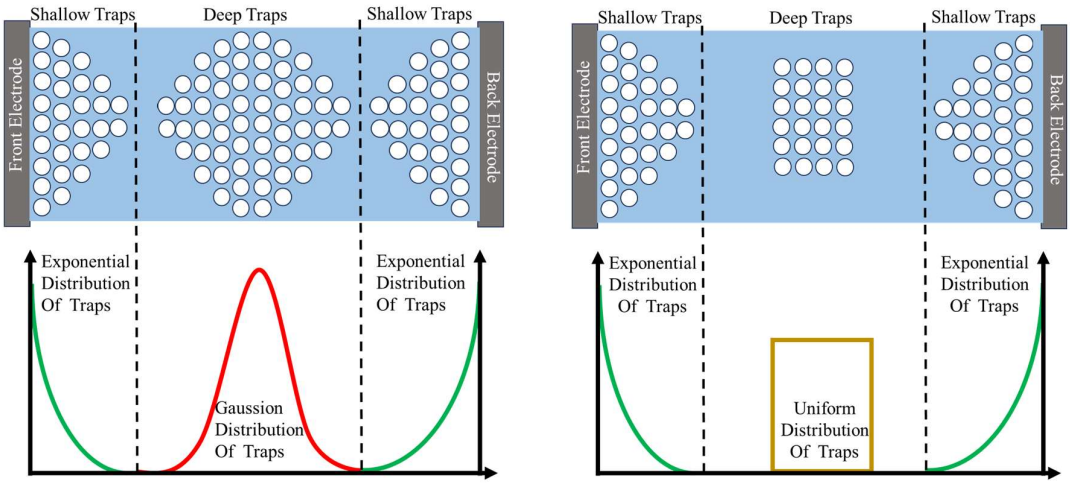

Figure 2.2: Different types of trap distributions in the bandgap of a sample

$$J_d = nq\mu E \tag{2.12}$$

As the applied voltage increases, space charge-limited current can be observed in a system with traps. Considering a system with discrete traps in the bandgap described by **Equation (2.13)**, the relationship between current and voltage follows **Equation (2.14)** [34].

$$n_t = \frac{N_t}{1+\exp\left[\frac{E_T - E_F}{kT}\right]} \tag{2.13}$$

$$J = \frac{9}{8}\mu\varepsilon\theta\frac{V^2}{L^3} \tag{2.14}$$

Where N_t, E_T, k and T are trap density, single trap energy, Boltzmann constant and absolute temperature, respectively. θ is defined as the trap factor and can be related to the free and trapped carrier density as

$$\theta = \frac{n_f}{n_f + n_t} \tag{2.15}$$

Typically, the presence of a single or discrete trap results in a sudden increase in current observed after the ohmic region in the log(I) versus log(V) curve. Suppose the system contains an exponential trap distribution within the bandgap region, characterised by a trap density

distribution as given by **Equation (2.16)**. In that case, the behaviour of the current-voltage characteristics can be distinctly influenced.

$$n_t = H_t \exp\left(\frac{F_n}{kT_c}\right) \tag{2.16}$$

Where T_c is the characteristic temperature, where $T_c = E_t/k$, where, E_t is trap energy, H_t is trap density, F_n is the electron Fermi energy. n_t and n are interrelated as follows

$$n_t = H_n \exp\left(\frac{F_n}{kT_c}\right) \tag{2.17}$$

$$n = N_c \exp\left(\frac{F_n}{kT}\right) \tag{2.18}$$

$$n_t = H_n \exp\left(\frac{F_n}{kT} * \frac{T}{T_c}\right) \tag{2.19}$$

$$n_c = H_n \left(\frac{n}{N_c}\right)^{1/m} \tag{2.20}$$

$$n_t = Cn^{1/m} \tag{2.23}$$

The expression for current density can be derived from the solution of the Poisson **Equation (2.11)** and **Equation (2.16)** as follows [35]

$$J = N_c \mu \left(\frac{2m+1}{m+1}\right)^{m+1} \left(\frac{\varepsilon m}{(m+1)H_n}\right)^{m} q^{m-1} \frac{V^{m+1}}{L^{2m+1}} \tag{2.24}$$

This process is known as Trap Charge Limited Conduction. The power law dependency, where $J \sim V^{m+1}$, is the most notable aspect of the **Equation (2.24)** mentioned earlier [36]. This specific current-voltage (I-V) relationship emerges due to exponential traps distribution in the bandgap.

In this section, we have discussed the different transport mechanisms utilized in our study to analyse the current-voltage characteristics. Our goal was to gain insights into the charge transport mechanisms in perovskite-based optoelectronic devices, including scenarios

involving the presence of carbon nanotubes (CNTs). Additionally, we have estimated several electrical parameters of the devices, directly illustrating the enhancements in charge transport within the system. In the next section, we shall delve into the significance of carbon nanotubes (CNTs) in optoelectronic devices and their role in improving the charge transport mechanism.

2.3 Factors Affecting the Conductivity

As we have discussed in our previous chapter, the conductivity of organic dye-based cells is influenced by multiple interconnected factors that govern charge transport and recombination dynamics. Molecular structure and energy levels of the dye play a critical role, as efficient charge transfer depends on the alignment of the dye's highest occupied molecular orbital (HOMO) and lowest unoccupied molecular orbital (LUMO) with the semiconductor and electrolyte. Charge carrier mobility is another key factor, affected by the intrinsic electronic properties of the dye, the presence of π-conjugated systems, and molecular packing. Electrode material and interface quality significantly impact conductivity, as poor contact or high resistance at the dye/semiconductor or semiconductor/electrode interface can limit charge collection. We have discussed some of the factors below.

2.3.1 Richardson Constant

As we have discussed in the previous chapter the Richardson constant (A^*) plays a crucial role in understanding and optimizing the conductivity of organic dye-based cells, particularly in the context of thermionic emission and charge transport mechanisms at metal/organic (M/O) interfaces [37–39]. It plays a crucial role in determining the efficiency of charge injection from metal electrodes into organic dye-based devices [40]. The value of the Richardson constant influences the temperature-dependent conductivity and carrier mobility, which are essential for optimizing organic electronic devices [41,42].

The concept of the Richardson constant is derived from the free electron theory of metals, assuming that electrons inside a metal behave like a Fermi gas. The density of electron states determines the number of electrons per unit volume with energy between $\vec{E}$ to $\vec{E} + d\vec{E}$ given by the function below (**Equation (2.25)**) [43].

$$g(\vec{E}) = \frac{8\pi\sqrt{2m^3}E^{\left(\frac{1}{2}\right)}}{h^3} \tag{2.25}$$

where m is the electron mass and h is Planck's constant. At thermal equilibrium, electrons follow the Fermi-Dirac distribution, expressed as follows (**Equation (2.26)**).

$$f(\vec{E}) = \frac{1}{1+e^{\left(\frac{E-E_F}{kT}\right)}} \tag{2.26}$$

where E_F is the Fermi energy. For the total emission current density, the electron has energy greater than the Barrier Height (Φ_b) can give the conductivity of the cell. Integrating over all possible electron energies, we can get the expression for current density as **Equation (2.27).**

$$J_0 = \int_{\Phi_b}^{\infty} eV_Z g(\vec{E}) f(\vec{E}) d\vec{E} \tag{2.27}$$

The velocity component normal to the surface is related to the total energy as **Equation (2.28)** below.

$$V_Z = \sqrt{\frac{2E}{m}} \tag{2.28}$$

Integrating Equation 2.3 over all possible velocities leads to the expression as **Equation (2.29)** below.

$$J_0 = A^* T^2 e^{-\left(\frac{\Phi_b}{kT}\right)} \tag{2.29}$$

Thus the Schottky diode's forward-bias I-V relation becomes as **Equation (2.30)**

$$J = J_0 \exp\left[\frac{qV}{nkT}\right] \tag{2.30}$$

Substituting numerical values for fundamental constants results in A^*=120.2 A/cm²K². Now for a many-electron system, the mass (m) in the above equation can be replaced with the effective mass (m^*) of the system as **Equation (2.31)**.

$$A^* = \frac{4\pi m^* e k^2}{h^3} \tag{2.31}$$

This theoretical formulation of the Richardson constant is fundamental in understanding thermionic emission and charge transport in metal-organic and semiconductor devices. **Equation (2.29)** is known as the Richardson-Dushman Equation. In 1938, Walter Schottky extended this theory to metal-semiconductor contacts, accounting for the influence of an electric field at the interface, which reduces the barrier height, given by **Equation (2.32)** [44].

$$J_0 = A^* T^2 e^{-\left(\frac{\phi_b^{eff}}{kT}\right)} \tag{2.32}$$

where ϕ_b^{eff} is the effective barrier height considering the field-induced lowering. As organic electronics began to gain attention in the mid-20th century, the theory was adapted to M/O contacts to incorporate the unique properties of organic materials. The equation was further modified to include field-enhanced emission effects, described by the Poole-Frenkel effect, **Equation (2.33)** [45,46].

$$J_0 = A^* T^2 e^{-\left(\frac{\Phi_b - \beta\sqrt{E}}{kT}\right)} \tag{2.33}$$

where β is the Poole-Frenkel coefficient. These advancements have been fundamental in understanding charge injection and transport in devices such as organic light-emitting diodes (OLEDs), organic photovoltaics (OPVs), and organic field-effect transistors (OFETs). Key articles contributing to the development of the Richardson-Schottky theory include Richardson's 1901 paper on thermionic emission, Schottky's 1938 work on metal-semiconductor junctions, and later studies such as Poole and Frenkel's 1940s work on field effects, with modern reviews found in works like Burgelman et al. (2003) and Kahn et al. (2003) [45–47].

2.3.2 Barrier Height Inhomogeneity

Barrier inhomogeneity refers to the spatial variation in the energy barrier height at the interface between a metal electrode and a semiconductor, often observed in real-world Schottky junctions. Unlike the ideal case where a uniform barrier exists across the entire contact area, practical devices exhibit microscopic fluctuations due to interfacial defects, grain boundaries,

surface roughness, chemical inhomogeneities, or localised interface states. These non-uniformities cause the local Schottky barrier height to deviate from the average, resulting in the formation of high and low barrier patches across the interface, as **Figure 2.3**. Consequently, current conduction becomes dominated by the lower-barrier regions, particularly under forward bias, leading to deviation from ideal thermionic emission behaviour and a reduction in the effective barrier height extracted from current-voltage (J–V) characteristics. Barrier inhomogeneity not only influences charge injection and transport dynamics but also affects the temperature dependence of device performance, Richardson constant modification, and the overall reliability of electronic and optoelectronic systems. Early models, such as Schottky's 1938 theory, considered a single uniform barrier [48]. However, experimental deviations suggested a Gaussian distribution of barrier heights, leading to a modification of the standard equation [49]. The effective barrier height (ϕ_b^{eff}) is expressed as **Equation (2.34)** [30,50,51],

$$\phi_b^{eff} = \phi_b - \frac{q\zeta_0^2}{2kT} \tag{2.34}$$

where ζ_0 represents the reduced patch parameter determines the standard deviation of the barrier height distribution. This modification accounts for barrier inhomogeneity due to interface fluctuations. Consequently, the thermionic emission equation is rewritten as **Equation (2.35)**.

$$J = A_{eff}^{*} T^2 e^{-\left(\frac{\phi_b^{eff}}{kT}\right)} \tag{2.35}$$

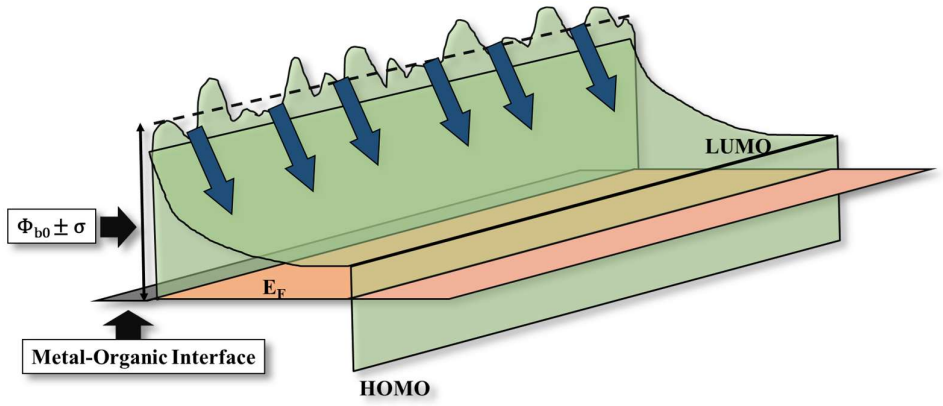

Figure 2.3: Energy band diagram to show the presence of BHI at the interface

Where A^*_{eff} It is the Richardson constant of a homogeneous barrier junction. Further refinements, including patch models and two-barrier models, have been introduced to address lateral variations at the contact interface. Studies such as Werner and Gütler (1991) and Tung (2001) have provided significant contributions to understanding barrier inhomogeneity and its impact on transport mechanisms [52–56]. These developments are essential in designing high-performance electronic and optoelectronic devices, where non-uniformities in the barrier significantly influence charge injection, transport, and overall device efficiency. Tung's analytical model describes the impact of barrier height inhomogeneity (BHI) on the current-voltage-temperature (I-V-T) characteristics of a Schottky diode [57]. This concept is physically represented as a network of low-barrier (LB) regions embedded within a high-barrier (HB) matrix. The reduction in barrier height is quantified by the patch parameter γ [$\gamma = 3(0.25R_0^2)^{1/3}$], which accounts for the patch size (R_0) and the variation in interfacial barrier height between LB and HB regions (Δ). More broadly, the inhomogeneous Schottky barrier is often described using a semi-Gaussian distribution, characterised by the peak patch density (C_1) and the spread in the reduced patch parameter (σ) [57]. In such an inhomogeneous Schottky barrier diode (SBD), both temperature and applied bias influence the effective area participating in current transport. At lower temperatures, current is predominantly carried through the LB regions, engaging only a limited portion of the total contact area. However, as temperature increases, the contribution from the HB regions grows, leading to a more uniform spatial distribution of current flow. Considering the BHI parameters C_1 and σ, Equation (2.30) can be written as:

$$J = \left[A^*T^2 \exp\left(\frac{-q\phi_b}{kT}\right)\left\{1 + \frac{8C_1\pi\sigma^2}{9\beta_1}\exp\left(\frac{q^2\beta^2\zeta_0^2}{2k^2T^2}\right)\right\}\right] \exp\left[\frac{qV}{kT}\right] \quad (2.36)$$

Where $\beta = \left(\frac{V_i}{\eta}\right)^{1/3}$ and $\eta = \left(\frac{\epsilon_s}{qN_d}\right)$ is a doping density-dependent parameter [57]. Comparing the above Equation (2.36) with Equation (2.30), we can write

$$J_0 = A^*T^2 \exp\left(\frac{-q\phi_b}{kT}\right) 1 + \frac{8C_1\pi\zeta_0^2}{9\beta_1} \exp\left(\frac{q^2\beta^2\zeta_0^2}{2k^2T^2}\right) \quad (2.37)$$

Taking ln on both sides of Equation (2.37) and using the approximation $\ln(1 + x) \approx x$ in the HB-dominated regime, we can rewrite as (**Equation (2.38)**).

$$\ln\left(\frac{J_0}{T^2}\right) = -\frac{q\phi_b}{kT} + \ln A^* + \frac{8C_1\pi\zeta_0^2}{9\beta_1}\exp\left(\frac{q^2\beta^2\zeta_0^2}{2k^2T^2}\right) \tag{2.38}$$

From Equation (2.38) and Equation (2.35) we can write

$$\ln(A^*_{eff}) - q\frac{\phi_b^{eff}}{kT} = -\frac{q\phi_b}{kT} + \ln A^* + \frac{8C_1\pi\zeta_0^2}{9\beta_1}\exp\left(\frac{q^2\beta^2\zeta_0^2}{2k^2T^2}\right) \tag{2.39}$$

2.3.3 Polaron Formation and Hopping Transport

A polaron is a quasi-particle consisting of a charge carrier (electron or hole) coupled with a local lattice distortion due to electron-phonon interactions. In organic semiconductors, charge carriers are strongly localised on individual molecules or polymer chains, creating a self-trapped state where the charge is surrounded by a deformation in the molecular structure [58,59]. Organic materials exhibit strong electron-phonon interactions due to their molecular flexibility. When an electron or hole is introduced, it distorts the surrounding lattice, leading to a local potential well. The strength of this coupling determines whether the charge carrier will move freely or remain self-trapped as a polaron. The Holstein small polaron model describes this process, where charge carriers hop from one localised state to another via phonon-assisted mechanisms [60]. Polarons in organic dye-based materials can be classified into two types: Small Polarons (SP) and Large Polarons (LP). SPs are highly localised on a single molecule, requiring high activation energy for hopping transport. While LPs are spread over multiple molecular sites, allowing easier charge transport with lower activation energy. The formation of these polarons depends on the molecular packing, electronic structure, and dielectric properties of the organic material [60–62]. Due to the absence of extended band states in organic materials, charge transport occurs primarily via hopping mechanisms. Various models describe this process, including Nearest-Neighbour-Hopping (NNH), Variable-Range-Hopping (VRH), and Marcus Theory.

2.3.3.a Nearest-Neighbour Hopping (NNH)

NNH is a charge transport mechanism in organic semiconductors where charge carriers move between adjacent localised states [63]. Due to the disorder and weak intermolecular interactions in organic dye-based materials, extended band transport is not viable. Instead, charge transport occurs through thermally activated hopping between molecular sites. The hopping rate between two sites i and j is described by the Miller-Abrahams, **Equation (2.40)**.

$$W_{ij} = \nu_0 \exp\left(-\frac{2\gamma R_{ij}+\Delta E}{kT}\right) \quad (2.40)$$

Here, ν_0 represents the attempt frequency, which defines the intrinsic probability of a charge carrier attempting a hop. The parameter γ is the wavefunction decay constant, which quantifies the extent to which the electronic wavefunction of a localised state decays spatially. The hopping distance between sites is denoted as R_{ij}, describing the spatial separation between the initial and final states. Additionally, ΔE represents the energy difference between the two states, influencing the thermal activation energy required for hopping. When the energy difference ΔE is negative ($E_j < E_i$The hopping rate is maximised since the process is downhill energetically. However, for upward hopping ($E_j > E_i$The rate decreases exponentially with increasing ΔE, making charge transport thermally activated, **Equation (2.41)**.

$$\sigma_{dc} = \sigma_0 \exp\left(-\frac{E_a}{kT}\right) \quad (2.41)$$

2.3.3.b Variable-Range Hopping (VRH)

VRH is a charge transport mechanism that describes electron hopping between localised states in disordered semiconductors at low temperatures [64]. Unlike nearest-neighbour hopping (NNH), where charge carriers hop between adjacent sites, VRH allows carriers to hop over variable distances to minimise energy barriers, improving charge transport efficiency. Again, Mott's Variable-Range Hopping Model is a temperature-dependent expression for electrical conductivity in disordered systems, represented by **Equation (2.42)**.

$$\sigma_{dc} = \sigma_0 \exp\left(-\frac{T_0}{T}\right)^{\left(\frac{1}{d+1}\right)} \quad (2.42)$$

Where T_0 is a characteristic temperature dependent on material properties, d is the dimensionality of the transport (1D, 2D, or 3D), and T is the absolute temperature. For three-dimensional (3D) transport (d = 3), the equation simplifies to **Equation (2.43)**.

$$\sigma_{dc} = \sigma_0 \exp\left(-\frac{T_0}{T}\right)^{\left(\frac{1}{4}\right)} \quad (2.43)$$

For two-dimensional (2D) transport (d = 2), the equation reduces to **Equation (2.44)**.

$$\sigma_{dc} = \sigma_0 \exp\left(-\frac{T_0}{T}\right)^{\left(\frac{1}{3}\right)} \tag{2.44}$$

At very low temperatures, Efros-Shklovskii modified the VRH Model as Coulomb interactions between localised charge carriers can modify the density of states, leading to the Efros-Shklovskii VRH model (**Equation (2.45)**) [65].

$$\sigma_{dc} = \sigma_0 \exp\left(-\frac{T_1}{T}\right)^{\frac{1}{2}} \tag{2.45}$$

where T_1 is another characteristic temperature associated with the Coulomb gap. This model is particularly important for highly disordered organic semiconductors where electron-electron interactions significantly influence transport properties.

2.3.3.c Marcus theory

Marcus' theory of charge transfer describes the mechanism of electron transfer in organic semiconductors, particularly in systems where charge carriers hop between localised states [66]. The rate of charge transfer between a donor and an acceptor is given by the Marcus rate equation (**Equation (2.46)**).

$$k_{ET} = \frac{2\pi}{\hbar} \frac{|V_{DA}|^2}{\sqrt{4\pi\lambda\ _B T}} \exp\left(-\frac{(\Delta G+\lambda)^2}{4\lambda k_B T}\right) \tag{2.46}$$

where k_{ET} is the electron transfer rate, $\hbar$ is the reduced Planck's constant, V_{DA} is the electronic coupling between donor and acceptor, λ is the reorganisation energy, k_B is the Boltzmann constant, T is the absolute temperature, and ΔG is the Gibbs free energy change associated with the transfer process. The reorganisation energy consists of internal (λ_{int}) and external (λ_{ext}) contributions (**Equation (2.47**)).

$$\lambda = \lambda_{int} + \lambda_{ext} \tag{2.47}$$

where λ_{int} arises from structural changes within the molecule, and λ_{ext} is due to polarization effects from the surrounding medium. The optimal condition for charge transfer occurs when $\Delta G = -\lambda$, leading to the fastest transfer rate. For highly exergonic reactions ($\Delta G \ll -\lambda$), the charge transfer rate decreases, a phenomenon known as the Marcus inverted region. This theory plays a crucial role in understanding charge transport in organic dye-based solar cells, OLEDs, and molecular electronic devices.

2.3.4 Activation energy

In organic semiconductors, activation energy refers to the energy required to move charge carriers, such as electrons or holes, through the material. Due to the disordered molecular structure of most organic semiconductors, charge transport occurs via a hopping mechanism between localised states rather than through a continuous conduction band. This process requires thermal energy to overcome barriers between these states, making the activation energy a key factor in determining electrical conductivity. Lower activation energy generally leads to better charge mobility and improved device performance in applications like organic light-emitting diodes (OLEDs) and organic solar cells.

2.3.4.a DC Activation Energy

Activation energy (E_a) is the minimum energy required for charge carriers to overcome potential barriers during charge transport. It plays a crucial role in determining the charge mobility and conductivity of organic semiconductors. The temperature dependence of conductivity (σ) in organic materials is typically described by an Arrhenius-type equation. Charge transport is influenced by E_a, as it governs the hopping or tunnelling of charge carriers between molecules in the organic dye and the semiconductor interface. A lower E_a indicates efficient charge transport, which enhances overall solar cell performance. Recombination kinetics are also affected, with higher activation energy suggesting that electron-hole recombination is thermally activated. This directly impacts the open-circuit voltage (V_{OC}) and device efficiency, with typical E_a values for recombination in DSSCs ranging from 0.5 to 1.2 eV. Lastly, exciton dissociation is a critical process where bound electron-hole pairs (excitons) must be separated into free charge carriers before recombination occurs. Activation energy determines the efficiency of this dissociation at the semiconductor/dye/electrolyte interface, influencing charge collection and overall energy conversion efficiency.

2.3.4.b AC Activation Energy

The AC conductivity (σ_{ac}) of organic dye-based cells provides insights into charge transport mechanisms, carrier mobility, and interfacial polarisation effects. It is typically studied using impedance spectroscopy, where an alternating voltage is applied, and the resulting current response is analysed. The σ_{ac} follows a power-law dependence on frequency, given by Jonscher's Universal Law, given by **Equation (2.48)**.

$$\sigma_{ac}(\omega) = \sigma_{dc} + A\omega^{s} \tag{2.48}$$

where σ_{dc} is the DC conductivity, Á is a temperature-dependent parameter, ω is the angular frequency, and s ($0 < s < 1$) represents the degree of charge carrier hopping. In DSSCs, charge transport occurs via thermally activated hopping mechanisms between localised states in the organic dye and the semiconductor interfaces. At lower frequencies, AC conductivity is dominated by electrode polarisation and space charge effects, while at higher frequencies, hopping conduction prevails. Studying AC conductivity helps in understanding recombination dynamics, trap states, and optimising materials for improved photovoltaic performance.

2.4 Different Nanoparticles and Nanotubes in Organic Devices and Their Properties

We have fabricated a range of organic dye-based devices, incorporating various nanoparticles and nanotubes, including Titanium-Dioxide Nanoparticles (TiO_2 NPs), Zinc-Oxide Nanoparticles (ZnO NPs), Single-Walled-Carbon-Nanotubes (SWCNTs), and Multi-Walled-Carbon-Nanotubes (MWCNTs). The characteristics and properties of these nanomaterials are analysed in the following subsections.

2.4.1 Titanium-Dioxide (TiO_2) Nanoparticles

Titanium dioxide (TiO_2) possesses a multitude of exceptional attributes, encompassing non-toxicity, resilience to photochemical and chemical degradation, and economic viability. These advantageous properties render TiO_2 indispensable in a wide array of applications, including self-cleaning surfaces, photovoltaic cells, chemical sensors, hydrogen evolution reactions, pigments, and environmental remediation [67]. The synthesis of oxide nanoparticles through diverse methodologies has garnered immense significance due to their superior electrical, optical, and magnetic characteristics compared to their bulk counterparts [68]. TiO_2 manifests

in three principal solid-phase polymorphs, anatase, rutile, and brookite, while also existing in both crystalline and amorphous configurations. A schematic representation of these three crystalline structures is illustrated in **Figure 2.4**.

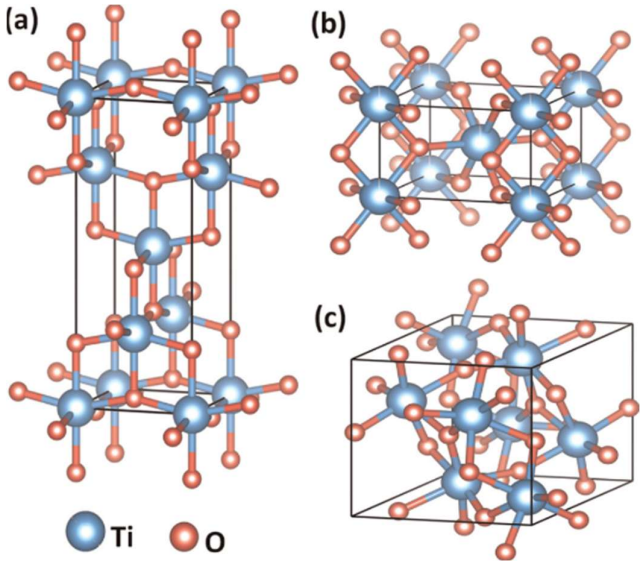

Figure 2.4: Crystal structures of TiO_2 (a) anatase (tetragonal), (b) rutile (tetragonal), and (c) brookite (orthorhombic) polymorphs

The extensive surface area, interconnected porosity, and high dye adsorption capacity of TiO_2 thin films make them a pivotal component in dye-sensitised solar cells (DSSCs). Notably, Grätzel et al. have already demonstrated a conversion efficiency surpassing 11% in laboratory-scale DSSCs [69]. The integration of high-performance TiO_2 nanoparticles in DSSC electrodes has been shown to significantly enhance device stability and energy conversion efficiency [70]. In our research, we have specifically employed anatase-phase TiO_2 due to its superior optoelectronic properties.

2.4.2 Zinc Oxide (ZnO) Nanoparticles

Zinc oxide (ZnO) is an inorganic compound that appears white at room temperature but turns yellow upon heating. It is insoluble in water [71,72]. ZnO can crystallise into three distinct structures: wurtzite, rocksalt, and zinc blende. A schematic representation of these crystal formations is illustrated in **Figure 2.5** [73]. However, under standard ambient conditions, the wurtzite structure remains the most thermodynamically stable configuration. The wurtzite-phase ZnO exhibits a hexagonal crystalline lattice with sp^3 hybridised covalent bonding and

tetrahedral coordination [73,74]. Recognised as a pivotal nanomaterial, wurtzite ZnO is extensively employed due to its wide bandgap and high excitonic binding energy.

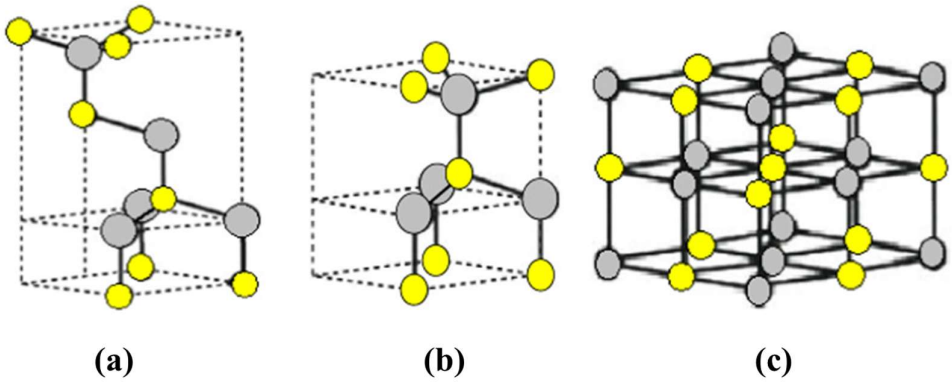

Figure 2.5: Schematic Diagram of (a) Zinc Blende, (b) Hexagonal Wurtzite and (c) Rock Salt Structure of ZnO. Yellow and Grey Spheres denote O and Zn atoms

Several intrinsic properties, including cost efficiency, superior electron mobility, exceptional electron affinity, and compatibility with low-temperature crystallisation, render ZnO nanoparticles highly advantageous as inorganic metal oxides for integration into organic electronic systems [75,76]. By mitigating charge recombination and prolonging charge carrier lifetimes, ZnO nanoparticles significantly augment the efficiency of organic devices.

2.4.3 Multi-Wall Carbon Nanotubes (MWCNT)

Multi-walled carbon nanotubes **(**MWCNTs**)** comprise multiple concentric graphene cylinders uniformly spaced around a central hollow core. **Figure 2.6** presents a schematic depiction of MWCNT architecture. The interlayer separation within MWCNTs typically falls within the range of 0.34 to 0.39 nm. Their inner diameters span from 0.4 nm to a few nanometers, whereas the outer diameters extend between 2 nm and 30 nm [77–79].

Axially, MWCNTs exhibit highly variable lengths, ranging from 1 μm to several centimetres. The termini of these nanotubes are generally sealed by pentagonal ring defects, effectively capping both ends. The presence of structural discontinuities in the pentagonal carbon network enables complete closure of the nanotube extremities [80]. Due to their multilayered architecture, MWCNTs exhibit superior tensile strength compared to single-walled carbon nanotubes (SWCNTs). Furthermore, the outermost graphene layers act as a protective barrier,

shielding the inner nanotube walls from environmental chemical interactions, thereby enhancing their structural robustness and stability.

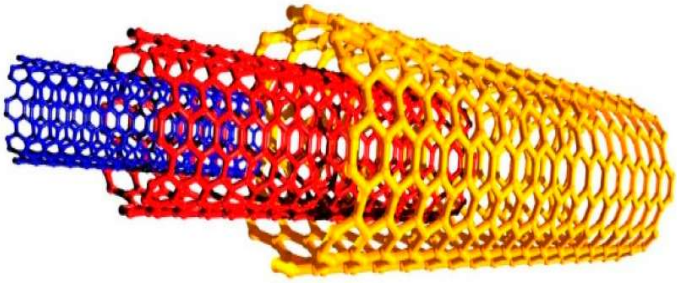

Figure 2.6: Structure of MWCNT

2.4.4 Single-Wall Carbon Nanotubes (SWCNT)

Carbon nanotubes (CNTs) have garnered substantial scientific interest since their initial discovery in 1991 by the Japanese physicist Sumio Iijima [81–83]. Their extraordinary physical, mechanical, and electrical properties have made them a subject of extensive research. Notably, CNTs exhibit exceptional electrical conductivity, comparable to that of copper (Cu). Structurally, CNTs are classified into two fundamental types: single-walled carbon nanotubes (SWCNTs) and multi-walled carbon nanotubes (MWCNTs). These nanostructures belong to the one-dimensional (1D) material class due to their unique geometrical confinement. SWCNTs consist of a solitary graphene layer rolled into a cylindrical form, as schematically represented in **Figure 2.7**. Their atomic arrangement follows an sp^2-hybridized carbon network, akin to graphite, leading to the formation of hexagonal carbon rings. Typically, SWCNTs possess an ultrathin wall thickness—only one atom in width—while their circumference comprises approximately ten atoms. Due to their exceedingly high length-to-diameter aspect ratio (~1000), they exhibit an effectively one-dimensional electronic structure [81,84]. At cryogenic temperatures, SWCNTs manifest quantum mechanical phenomena, such as Coulomb blockade and single-electron charging effects, akin to those observed in quantum dots and nanowires. These quantum properties facilitate the fabrication of nanoscale electronic and optoelectronic devices with unprecedented miniaturisation. Typically, SWCNTs exhibit diameters below 4 nm, while their lengths extend to the micrometre scale. Depending on the

specific manner in which the graphene sheet is rolled into a tubular structure, SWCNTs adopt one of three distinct chiral configurations: armchair, zigzag, or chiral.

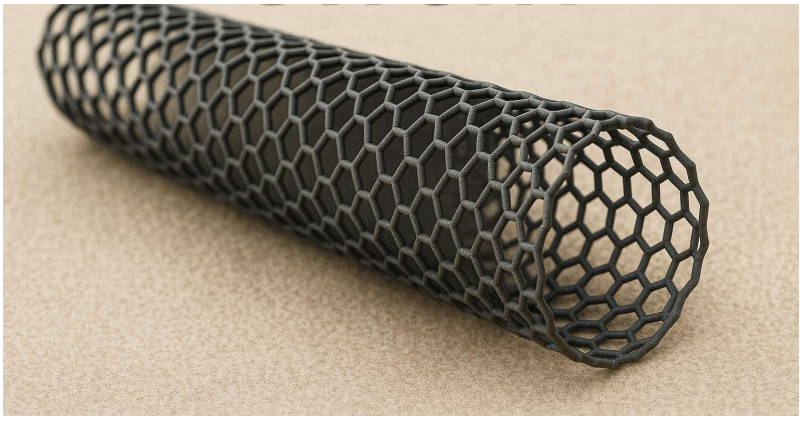

Figure 2.7: Structure of SWCNT

2.5 Conclusion

This chapter explores various parameters influencing the charge injection mechanism, including trap concentration, interfacial barrier, depletion layer width, band bending, image force barrier lowering, and barrier inhomogeneities at the metal-organic semiconductor junction. Additionally, it examines how materials such as ZnO, TiO_2, SWCNT, and MWCNT impact these parameters. To analyze these aspects, the fundamental working principles of organic devices are discussed alongside different charge injection models, including the Richardson-Schottky thermionic emission model, the drift-diffusion charge injection model, the hopping charge injection model, and the Fowler-Nordheim tunneling model. The influence of trapping effects on charge carriers and the exponential distribution of traps are also considered. The parameters affecting charge carrier injection can be determined using steady-state I-V and C-V characteristics. Furthermore, the chapter reviews specific properties of ZnO, TiO_2, SWCNT, and MWCNT, which have been integrated into various organic dye-based devices.

2.6 References:

[1] A. Eatemadi, H. Daraee, H. Karimkhanloo, M. Kouhi, N. Zarghami, A. Akbarzadeh, M. Abasi, Y. Hanifehpour, S.W. Joo, Carbon nanotubes: Properties, synthesis, purification, and medical applications, Nanoscale Res Lett 9 (2014) 1–13. https://doi.org/10.1186/1556-276X-9-393.

[2] S. Antohe, S. Iftimie, L. Hrostea, V.A. Antohe, M. Girtan, A critical review of photovoltaic cells based on organic monomeric and polymeric thin film heterojunctions, Thin Solid Films 642 (2017) 219–231. https://doi.org/10.1016/j.tsf.2017.09.041.

[3] N. Saifuddin, A.Z. Raziah, A.R. Junizah, Carbon nanotubes: A review on structure and their interaction with proteins, J Chem (2013). https://doi.org/10.1155/2013/676815.

[4] H. Ishii, K. Sugiyama, E. Ito, K. Seki, Energy level alignment and interfacial electronic structures at organic/metal and organic/organic interfaces, Advanced Materials 11 (1999) 605–625. https://doi.org/10.1002/(SICI)1521-4095(199906)11:8<605::AID-ADMA605>3.0.CO;2-Q.

[5] C.N. Gannett, L. Melecio-Zambrano, M.J. Theibault, B.M. Peterson, B.P. Fors, H.D. Abruña, Organic electrode materials for fast-rate, high-power battery applications, Materials Reports: Energy 1 (2021). https://doi.org/10.1016/j.matre.2021.01.003.

[6] R. Otero, A.L. Vázquez de Parga, J.M. Gallego, Electronic, structural and chemical effects of charge-transfer at organic/inorganic interfaces, Surf Sci Rep 72 (2017) 105–145. https://doi.org/10.1016/j.surfrep.2017.03.001.

[7] A.I. Hofmann, E. Cloutet, G. Hadziioannou, Materials for Transparent Electrodes: From Metal Oxides to Organic Alternatives, Adv Electron Mater 4 (2018). https://doi.org/10.1002/aelm.201700412.

[8] N. Koch, A. Kahn, J. Ghijsen, J.J. Pireaux, J. Schwartz, R.L. Johnson, A. Elschner, Conjugated organic molecules on metal versus polymer electrodes: Demonstration of a key energy level alignment mechanism, Appl Phys Lett 82 (2003) 70–72. https://doi.org/10.1063/1.1532102.

[9] Khalil Ebrahim Jasim, Seamas Cassidy, Feryad Zaki Henari, Akil Aziz Dakhel, Curcumin Dye-Sensitized Solar Cell, Journal of Energy and Power Engineering 11 (2017). https://doi.org/10.17265/1934-8975/2017.06.006.

[10] A.S. Polo, N.Y. Murakami Iha, Blue sensitizers for solar cells: Natural dyes from Calafate and Jaboticaba, Solar Energy Materials and Solar Cells 90 (2006) 1936–1944. https://doi.org/10.1016/j.solmat.2006.02.006.

[11] H. Naarmann, The development of electrically Conducting Polymers, Advanced Materials 2 (1990) 345–348. https://doi.org/10.1002/adma.19900020802.

[12] M. Irimia-Vladu, E.D. Gåowacki, P.A. Troshin, G. Schwabegger, L. Leonat, D.K. Susarova, O. Krystal, M. Ullah, Y. Kanbur, M.A. Bodea, V.F. Razumov, H. Sitter, S. Bauer, N.S. Sariciftci, Indigo - A natural pigment for high performance ambipolar organic field effect transistors and circuits, Advanced Materials 24 (2012) 375–380. https://doi.org/10.1002/adma.201102619.

[13] E.D. Glowacki, L. Leonat, G. Voss, M. Bodea, Z. Bozkurt, M. Irimia-Vladu, S. Bauer, N.S. Sariciftci, Natural and nature-inspired semiconductors for organic electronics, Organic Semiconductors in Sensors and Bioelectronics IV 8118 (2011) 81180M. https://doi.org/10.1117/12.892467.

[14] M. Irimia-Vladu, P.A. Troshin, M. Reisinger, G. Schwabegger, M. Ullah, R. Schwoediauer, A. Mumyatov, M. Bodea, J.W. Fergus, V.F. Razumov, H. Sitter, S. Bauer, N.S. Sariciftci, Environmentally sustainable organic field effect transistors, Org Electron 11 (2010) 1974–1990. https://doi.org/10.1016/j.orgel.2010.09.007.

[15] C.J. Bettinger, Z. Bao, Organic thin-film transistors fabricated on resorbable biomaterial substrates, Advanced Materials 22 (2010) 651–655. https://doi.org/10.1002/adma.200902322.

[16] M. Irimia-Vladu, P.A. Troshin, M. Reisinger, L. Shmygleva, Y. Kanbur, G. Schwabegger, M. Bodea, R. Schwödiauer, A. Mumyatov, J.W. Fergus, V.F. Razumov, H. Sitter, N.S. Sariciftci, S. Bauer, Biocompatible and biodegradable materials for organic field-effect transistors, Adv Funct Mater 20 (2010) 4069–4076. https://doi.org/10.1002/adfm.201001031.

[17] W.R. Klaus Hunger, Peter Mischke, Azo Dyes, 1. General, Ullmann's Encyclopedia of Industrial Chemistry (2012). https://doi.org/10.1002/14356007.a03.

[18] SETFOS_Webinar_Notice_250408_143030, (n.d.).

[19] J. Wilson, J. Zhang, A. Song, Analytical Theory of Thin-Film Schottky Diodes, ACS Appl Electron Mater 1 (2019) 1570–1580. https://doi.org/10.1021/acsaelm.9b00324.

[20] E.W. Lim, R. Ismail, Conduction mechanism of valence change resistive switching memory: A survey, Electronics (Switzerland) 4 (2015) 586–613. https://doi.org/10.3390/electronics4030586.

[21] P.N. Murgatroyd, H.H. Wills, Theory of space-charge-limited current enhanced by Frenkel effect, 1969.

[22] M. Soylu, B. Abay, Analysing space charge-limited conduction in Au/n-InP Schottky diodes, Physica E Low Dimens Syst Nanostruct 43 (2010) 534–538. https://doi.org/10.1016/j.physe.2010.09.012.

[23] C.R. Crowbll, THE RICHARDSON CONSTANT FOR THERMIONIC EMISSION IN SCHOTTKY BARRIER DIODES, 1965.

[24] C.P.Y. Wong, C. Troadec, A.T.S. Wee, K.E.J. Goh, Gaussian Thermionic Emission Model for Analysis of Au/Mo S2 Schottky-Barrier Devices, Phys Rev Appl 14 (2020). https://doi.org/10.1103/PhysRevApplied.14.054027.

[25] C.Y. Wu, Interfacial layer-thermionic-diffusion theory for the Schottky barrier diode, J Appl Phys 53 (1982) 5947–5950. https://doi.org/10.1063/1.331384.

[26] F.C. Chiu, A review on conduction mechanisms in dielectric films, Advances in Materials Science and Engineering 2014 (2014). https://doi.org/10.1155/2014/578168.

[27] J. Pospisil, O. Zmeskal, S. Nespurek, J. Krajcovic, M. Weiter, A. Kovalenko, Density of bulk trap states of hybrid lead halide perovskite single crystals: temperature modulated space-charge-limited-currents, Sci Rep 9 (2019). https://doi.org/10.1038/s41598-019-40139-y.

[28] C.P. Kwan, M. Street, A. Mahmood, W. Echtenkamp, M. Randle, K. He, J. Nathawat, N. Arabchigavkani, B. Barut, S. Yin, R. Dixit, U. Singisetti, C. Binek, J.P. Bird, Space-charge limited conduction in epitaxial chromia films grown on elemental and oxide-based metallic substrates, AIP Adv 9 (2019). https://doi.org/10.1063/1.5087832.

[29] J.H. Werner, H.H. Güttler, Temperature dependence of Schottky barrier heights on silicon, J Appl Phys 73 (1993) 1315–1319. https://doi.org/10.1063/1.353249.

[30] J.H. Werner, H.H. Güttler, Barrier inhomogeneities at Schottky contacts, J Appl Phys 69 (1991) 1522–1533. https://doi.org/10.1063/1.347243.

[31] A. Rose, Space-Charge-Limited Currents in Solids, 1955.

[32] S. Heo, G. Seo, Y. Lee, D. Lee, M. Seol, J. Lee, J.B. Park, K. Kim, D.J. Yun, Y.S. Kim, J.K. Shin, T.K. Ahn, M.K. Nazeeruddin, Deep level trapped defect analysis in CH3NH3PbI3 perovskite solar cells by deep level transient spectroscopy, Energy Environ Sci 10 (2017) 1128–1133. https://doi.org/10.1039/c7ee00303j.

[33] M. Campos, J.A. Giacometti, M. Silver, Deep exponential distribution of traps in naphthalene, Appl Phys Lett 34 (1979) 226–228. https://doi.org/10.1063/1.90739.

[34] M.A. Lampert, Theory of Space-Charge-Limited Currents in an Insulator with Traps, 1956.

[35] P. Mark, W. Helfrich, Space-charge-limited currents in organic crystals, J Appl Phys 33 (1962) 205–215. https://doi.org/10.1063/1.1728487.

[36] D. Joung, A. Chunder, L. Zhai, S.I. Khondaker, Space charge limited conduction with exponential trap distribution in reduced graphene oxide sheets, Appl Phys Lett 97 (2010). https://doi.org/10.1063/1.3484956.

[37] S.K. Tripathi, M. Sharma, Analysis of the forward and reverse bias I-V and C-V characteristics on Al/PVA:n-PbSe polymer nanocomposites Schottky diode, J Appl Phys 111 (2012). https://doi.org/10.1063/1.3698773.

[38] H. Sheng, S. Muthukumar, N.W. Emanetoglu, Y. Lu, Schottky diode with Ag on (11$\bar{2}$0) epitaxial ZnO film, Appl Phys Lett 80 (2002) 2132–2134. https://doi.org/10.1063/1.1463700.

[39] R. Nouchi, Extraction of the Schottky parameters in metal-semiconductor-metal diodes from a single current-voltage measurement, J Appl Phys 116 (2014). https://doi.org/10.1063/1.4901467.

[40] L. Changshi, A Forward Current-Voltage-Temperature Method for Extraction of Intrinsic Schottky Barrier Height, ECS Journal of Solid State Science and Technology 9 (2020) 064007. https://doi.org/10.1149/2162-8777/aba4f3.

[41] O.C. Olawole, D.K. De, Theoretical studies of thermionic conversion of solar energy with graphene as emitter and collector, J Photonics Energy 8 (2018) 1. https://doi.org/10.1117/1.jpe.8.018001.

[42] K. Sarpatwari, O.O. Awadelkarim, M.W. Allen, S.M. Durbin, S.E. Mohney, Extracting the Richardson constant: IrOx /n-ZnO Schottky diodes, Appl Phys Lett 94 (2009). https://doi.org/10.1063/1.3156031.

[43] C.R. Crowell, The Richardson constant for thermionic emission in Schottky barrier diodes, Solid State Electronics 8 (1965) 395–399. https://doi.org/10.1016/0038-1101(65)90116-4.

[44] W.A. Harrison, A. Goebel, P.A. Clifton, Effective-mass theory of metal-semiconductor contact resistivity, Appl Phys Lett 103 (2013). https://doi.org/10.1063/1.4818265.

[45] H. Schroeder, Poole-Frenkel-effect as dominating current mechanism in thin oxide films - An illusion?!, J Appl Phys 117 (2015). https://doi.org/10.1063/1.4921949.

[46] M.M. El-Samanoudy, Modified Poole-Frenkel mechanisms in Ge 25 Bi x Sb 15-x S 60 thin films, Appl Surf Sci 207 (2003) 219–226. https://doi.org/10.1016/S0169-4332(02)01365-X.

[47] O.W. Richardson, Sulla radiazione negativa del platino caldo, Philosophical of the Cambridge Philosophical Society 11 (1901) 286–295.

[48] I.P. Batra, E. Tekman, S. Ciraci, THEORY OF SCHOTTKY BARRIER AND METALLIZATION, 1991.

[49] S. Acar, S. Karadeniz, N. Tuğluoğlu, A.B. Selçuk, M. Kasap, Gaussian distribution of inhomogeneous barrier height in Ag/p-Si (1 0 0) Schottky barrier diodes, Appl Surf Sci 233 (2004) 373–381. https://doi.org/10.1016/j.apsusc.2004.04.011.

[50] A. Dey, S. Middya, R. Jana, M. Das, J. Datta, A. Layek, P.P. Ray, Light induced charge transport property analysis of nanostructured ZnS based Schottky diode, Journal of Materials Science: Materials in Electronics 27 (2016) 6325–6335. https://doi.org/10.1007/s10854-016-4567-5.

[51] S. Chand, J. Kumar, On the existence of a distribution of barrier heights in Pd 2 Si / Si Schottky diodes, 288 (2014).

[52] J.H. Werner, H.H. Güttler, Barrier inhomogeneities at Schottky contacts, J Appl Phys 69 (1991) 1522–1533. https://doi.org/10.1063/1.347243.

[53] N.A. Al-Ahmadi, Schottky barrier inhomogeneities at the interface of different epitaxial layer thicknesses of n-GaAs/Ti/Au/Si: Al0.33Ga0.67As, Heliyon 6 (2020) e04852. https://doi.org/10.1016/j.heliyon.2020.e04852.

[54] H.G. Çetinkaya, M. Yıldırım, P. Durmuş, Altındal, Correlation between barrier height and ideality factor in identically prepared diodes of Al/Bi4Ti3O12/p-Si (MFS) structure with barrier inhomogeneity, J Alloys Compd 721 (2017) 750–756. https://doi.org/10.1016/j.jallcom.2017.06.037.

[55] H. Cetin, B. Şahin, E. Ayyildiz, A. Türüt, The barrier-height inhomogeneity in identically prepared H-terminated Ti/p-Si Schottky barrier diodes, Semicond Sci Technol 19 (2004) 1113–1116. https://doi.org/10.1088/0268-1242/19/9/007.

[56] B.H. Moon, G.H. Han, H. Kim, H. Choi, J.J. Bae, J. Kim, Y. Jin, H.Y. Jeong, M.K. Joo, Y.H. Lee, S.C. Lim, Junction-Structure-Dependent Schottky Barrier Inhomogeneity and Device Ideality of Monolayer MoS2 Field-Effect Transistors, ACS Appl Mater Interfaces 9 (2017) 11240–11246. https://doi.org/10.1021/acsami.6b16692.

[57] R.T. Tung, Electron transport at metal-semiconductor interfaces: General theory, Phys Rev B 45 (1992) 13509–13523.

[58] V. Coropceanu, J. Cornil, D.A. da Silva Filho, Y. Olivier, R. Silbey, J.L. Brédas, Charge transport in organic semiconductors, Chem Rev 107 (2007) 926–952. https://doi.org/10.1021/cr050140x.

[59] K.A. Ayala, Study of Charge Carrier Transport in Organic Semiconductors, 2013.

[60] M. Capone, W. Stephan, M. Grilli, Small-polaron formation and optical absorption in Su-Schrieffer-Heeger and Holstein models, 1997.

[61] A. Zhugayevych, S. Tretiak, Theoretical description of structural and electronic properties of organic photovoltaic materials, Annu Rev Phys Chem 66 (2015) 305–330. https://doi.org/10.1146/annurev-physchem-040214-121440.

[62] I.G. Austin, N.F. Mott, Polarons in Crystalline and Non-crystalline Materials, Adv Phys 18 (1969) 41–102. https://doi.org/10.1080/00018736900101267.

[63] H.Q. Lin, J.E. Hirsch, Two-dimensional Hubbard model with nearest-and next-nearest-neighbor hopping, n.d.

[64] R.M. Hill, Variable-Range Hopping 60 I phys, 1976.

[65] D.N. Tsigankov, A.L. Efros, Variable Range Hopping in Two-Dimensional Systems of Interacting Electrons, Phys Rev Lett 88 (2002) 4. https://doi.org/10.1103/PhysRevLett.88.176602.

[66] N. Lu, L. Li, W. Banerjee, P. Sun, N. Gao, M. Liu, Charge carrier hopping transport based on Marcus theory and variable-range hopping theory in organic semiconductors, J Appl Phys 118 (2015). https://doi.org/10.1063/1.4927334.

[67] F. Hamidi, F. Aslani, Tio2-based photocatalytic cementitious composites: Materials, properties, influential parameters, and assessment techniques, Nanomaterials 9 (2019). https://doi.org/10.3390/nano9101444.

[68] M.T. Aminzai, M. Yildirim, E. Yabalak, Metallic nanoparticles unveiled: Synthesis, characterization, and their environmental, medicinal, and agricultural applications, Talanta 280 (2024). https://doi.org/10.1016/j.talanta.2024.126790.

[69] A. Sen, M.H. Putra, A.K. Biswas, A.K. Behera, A. Groβ, Insight on the choice of sensitizers/dyes for dye sensitized solar cells: A review, Dyes and Pigments 213 (2023). https://doi.org/10.1016/j.dyepig.2023.111087.

[70] M. Shobana, P. Balraju, N. Muthukumarasamy, D. Velauthapillai, Glycerol-supportive Y3+ infused TiO2 nanoparticles: An electrode material for dye sensitized solar cell and supercapacitor applications, J Energy Storage 73 (2023). https://doi.org/10.1016/j.est.2023.108943.

[71] S. Raha, M. Ahmaruzzaman, ZnO nanostructured materials and their potential applications: progress, challenges and perspectives, Nanoscale Adv 4 (2022) 1868–1925. https://doi.org/10.1039/d1na00880c.

[72] E.A.S. Dimapilis, C.S. Hsu, R.M.O. Mendoza, M.C. Lu, Zinc oxide nanoparticles for water disinfection, Sustainable Environment Research 28 (2018) 47–56. https://doi.org/10.1016/j.serj.2017.10.001.

[73] H. Rai, Prashant, N. Kondal, A review on defect related emissions in undoped ZnO nanostructures, in: Mater Today Proc, Elsevier Ltd, 2021: pp. 1320–1324. https://doi.org/10.1016/j.matpr.2021.08.343.

[74] N. Abbas Shah, M. Gul, M. Abbas, M. Amin, Synthesis of Metal Oxide Semiconductor Nanostructures for Gas Sensors, n.d. www.intechopen.com.

[75] Z.U. Zango, A. Garba, F.B. Shittu, S.S. Imam, A. Haruna, M.U. Zango, I.A. Wadi, U. Bello, H. Adamu, B.E. Keshta, D.O. Bokov, O. Baigenzhenov, A. Hosseini-Bandegharaei, A state-of-the-art review on green synthesis and modifications of ZnO nanoparticles for organic pollutants decomposition and CO2 conversion, Journal of Hazardous Materials Advances 17 (2025). https://doi.org/10.1016/j.hazadv.2024.100588.

[76] A. Nawaz, A. Farhan, F. Maqbool, H. Ahmad, W. Qayyum, E. Ghazy, A. Rahdar, A.M. Díez-Pascual, S. Fathi-karkan, Zinc oxide nanoparticles: Pathways to micropollutant adsorption, dye removal, and antibacterial actions - A study of mechanisms, challenges, and future prospects, J Mol Struct 1312 (2024). https://doi.org/10.1016/j.molstruc.2024.138545.

[77] A.T. Krasley, E. Li, J.M. Galeana, C. Bulumulla, A.G. Beyene, G.S. Demirer, Carbon Nanomaterial Fluorescent Probes and Their Biological Applications, Chem Rev 124 (2024) 3085–3185. https://doi.org/10.1021/acs.chemrev.3c00581.

[78] Y.H. Gonfa, A. Bachheti, A. Husen, R.K. Bachheti, Carbon-Based Smart Nanomaterials: An Overview, in: 2024: pp. 1–17. https://doi.org/10.1007/978-981-97-0240-4_1.

[79] J.S. Bulmer, A. Kaniyoor, J.A. Elliott, A Meta-Analysis of Conductive and Strong Carbon Nanotube Materials, Advanced Materials 33 (2021). https://doi.org/10.1002/adma.202008432.

[80] N. De Jonge, M. Doytcheva, M. Allioux, M. Kaiser, S.A.M. Mentink, K.B.K. Teo, R.G. Lacerda, W.I. Milne, Cap closing of thin carbon nanotubes, Advanced Materials 17 (2005) 451–455. https://doi.org/10.1002/adma.200400266.

[81] S. Rathinavel, K. Priyadharshini, D. Panda, A review on carbon nanotube: An overview of synthesis, properties, functionalization, characterisation, and the application, Materials Science and Engineering: B 268 (2021). https://doi.org/10.1016/j.mseb.2021.115095.

[82] R. Kulkarni, L.P. Lingamdinne, J.R. Koduru, R.R. Karri, S.K. Kailasa, N.M. Mubarak, Y.Y. Chang, M.H. Dehghani, Exploring the recent cutting-edge applications of CNTs in energy and environmental remediation: Mechanistic insights and remarkable performance advancements, J Environ Chem Eng 12 (2024). https://doi.org/10.1016/j.jece.2024.113251.

[83] A. Aqel, K.M.M.A. El-Nour, R.A.A. Ammar, A. Al-Warthan, Carbon nanotubes, science and technology part (I) structure, synthesis and characterisation, Arabian Journal of Chemistry 5 (2012) 1–23. https://doi.org/10.1016/j.arabjc.2010.08.022.

CHAPTER 3

Effect of Titanium-Dioxide Nanoparticles on the Barrier Distribution for the Brilliant Blue Dye-based Metal-Semiconductor Contact Cells.

Table of Contents

3.1 Introduction

In the previous chapter, we discussed the fundamental working principles of organic devices and essential parameters influencing conductivity, including interfacial barrier height distribution, the Richardson constant, activation energy, and polaron hopping models. It also tracked their chronological evolution of the theories. Additionally, the chapter described the features of various nanoparticles that will be used in organic dye-based systems.

In this chapter, we will discuss about the modification of Barrier-Height-Inhomogeneity (BHI) at the interface by the incorporation of Titanium-Dioxide (TiO_2) nanoparticles. The charge flow at the metal-organic (M/O) contact, where an organic dye is sandwiched between two metal electrodes with different work functions, greatly impacts the performance of organic electronic devices. Interfacial band structure is vital for organic device functionality and performance enhancement. Interfacial band bending at metal-inorganic semiconductor junctions limits the current injection at the interface. The limited charge carrier flow through the M/O junction is recognised as a key factor in the low conductivity of these devices [1–4].

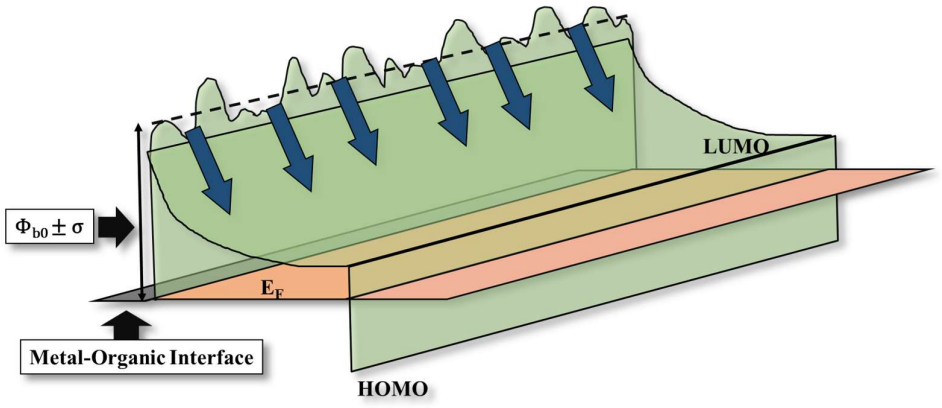

Figure 3.1: Energy band diagram to show the presence of BHI at the interface

The performance of M/O contacts is influenced by barrier height inhomogeneity (BHI), which refers to the uneven distribution of the energy barrier at the interface. This inhomogeneity can arise from various sources, such as differences in the surface chemistry of the metal and organic material, interfacial defects, and variations in the organic layer's thickness [5–9]. BHI can cause fluctuations in carrier concentration and mobility across the contact, leading to irregular current

flow, as illustrated in **Figure 3.1**. Consequently, this can degrade device performance, reducing both efficiency and reliability. Here we use Brilliant-Blue (BB) dye for the experiment, a synthetic organic molecule known as Brilliant-Blue FCF (Blue 1) is extensively employed as a blue colourant for processed foods, pharmaceuticals, nutritional supplements, and cosmetics [10]. It is classified as a triarylmethane dye and is recognised by various names, including acid blue 9 and FD&C Blue No. 1. Its E-number is E133, and its colour index is 42090. It appears as a blue powder and can be dissolved in glycerol and water [10]. It is acknowledged as one of the safest and least harmful colour additives ever approved by the FDA. Brilliant blue FCF, a synthetic dye, is created through the condensation of a suitable aniline and 2-formyl-benzene sulfonic acid and subsequent oxidation [11]. Typically, it exists as a disodium salt, with the CAS number of the diammonium salt being 2650-18-2. Salts of calcium and potassium are also permissible. Additionally, it can be presented as an aluminium lake. The resulting compound has the chemical composition $C_{37}H_{34}N_2Na_2O_9S_3$. **Figure 3.2(b)** displays the chemical composition of the BB dye. Blue No. 1 is mostly used to correct or enhance natural colouring, as well as to give colourless substances a vibrant hue, like many other colour additives [12]. Brilliant blue FCF is the more commonly used of the two approved blue dyes in the United States (the other being Indigo carmine, or FD&C Blue #2). It is found in various food and drink products such as cotton candy, ice cream, canned processed peas, packet soups, bottled food colourings, icings, ice pops, blueberry flavoured products, children's medications, dairy products, and soft drinks, including Blue Curaçao liqueur. Additionally, it is used in hygiene and cosmetics applications, including soaps, shampoos, and mouthwash. Additionally, the BB dye is a popular organic semiconductor dye in the triphenylmethane family with a HOMO-LUMO gap of 1.56 eV [13,14]. The conjugation of the BB dye's molecular structure and the presence of two sulfonic groups and three nitrogen centres may explain its intense colour and great interactivity with protein and macromolecules [15]. Thus, BB dye was used for protein visualisation [15–17], haemoglobin probing [18], and forensic fingerprint analysis [19]. This dye also shows dye-synthesised solar cell photovoltaic performance [20,21]. Marwa S. Salem et.al. recommended that the BB dye combined with p-Si substrate can be considered a strong candidate for photodetector applications [22].

On the other hand, TiO_2 NPs have been extensively studied due to their high photocatalytic activity, biocompatibility, and low toxicity. TiO_2 NPs have been employed in various applications, including drug delivery, biosensing, and environmental remediation. In addition, TiO_2 NPs have shown promising results in improving the performance of dye-sensitised solar

cells and light-emitting diodes [23–25]. Rutile, anatase, and brookite are the three polymorphs of TiO_2 that can form crystals. The metastable phase of anatase can only be generated under certain growth circumstances. While the rutile phase is the most prevalent and thermodynamically stable, the brookite phase can only be produced under extremely difficult synthesis circumstances [26,27]. **Figure 3.2 (a), (b), and (c)** represent the chemical makeup of TiO_2 NPs in the anatase, rutile, and brookite phases, respectively.

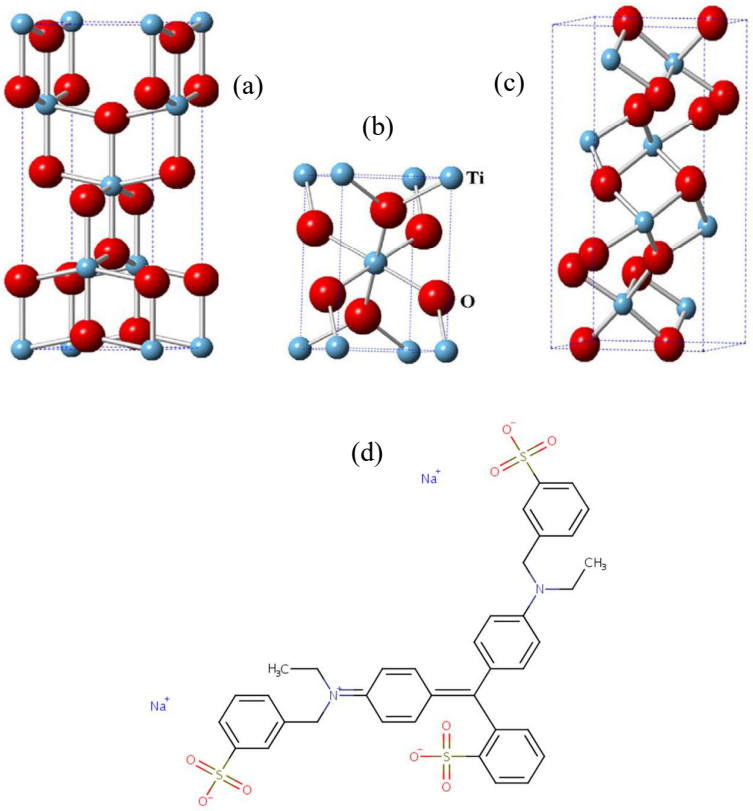

Figure 3.2: Chemical structure of TiO_2 NPs in (a) anatase phase. (b) rutile phase. (c) brookite phase. (d) Chemical structure of Brilliant-Blue.

We hypothesise that the addition of TiO_2 nanoparticles to the BB fruit dye-based cells can reduce the inhomogeneous distribution of barrier height and improve the device's performance. To investigate the stated hypothesis, a BB dye-based Schottky device structure was employed, consisting of an indium-tin-oxide-coated glass (ITO) front electrode and a copper plate (Cu) back electrode. The active layer of the device was composed of a blend of dye and nanoparticles (NPs) at a 1:1 ratio, which was positioned between the two electrodes. The device was

characterised using a Keithley-2400 source meter to measure the current-voltage-temperature (I-V-T) relationship, with the temperature ranging from 288K to 333K. Furthermore, the capacitance-voltage-frequency (C-V-F) characteristics of the device were evaluated using an Agilent 4649A LCR meter with a frequency range of 0.5 kHz to 100 kHz.

3.2 Experiment

This section provides a detailed overview of the experimental techniques, including the materials employed, instruments utilised, and related procedures.

3.2.1 Materials

Titanium dioxide (TiO_2) nanoparticles (99% purity), Brilliant Blue (BB) dye, Polyvinyl alcohol (PVA), a water-soluble polymer, act as a binding matrix to enhance the dispersion of TiO_2 nanoparticles and improve film-forming properties, Deionized (DI) water is used as a solvent for dissolving PVA and preparing uniform dispersions of TiO_2 and BB. Acetic acid may be used for surface modification of TiO_2, enhancing its compatibility with the dye. Additionally, ultrasonication equipment is necessary for achieving uniform dispersion of nanoparticles, while glass substrates such as ITO-coated glass are used as a base for thin-film deposition.

3.2.2 Instruments

This section highlights the key features and functions of the instruments used in our measurements, emphasising their relevance to the experimental procedures.

3.2.2.a Spin Coater

A spin coating unit is a device used to apply uniform thin films to flat substrates, as shown in **Figure 3.3**. In this research work, I used the EZspin-A1 from Apex Instruments for spin coating. The EZspin-A1 is a highly reliable and precise spin coating unit designed for uniform thin-film deposition. It operates by placing a small amount of coating solution on the substrate, which is then rapidly spun to spread the solution evenly across the surface due to centrifugal force. The speed and duration of the spin can be finely controlled to achieve the desired film thickness and uniformity. This unit is particularly suited for fabricating perovskite films, ensuring consistent and high-quality coatings essential for device performance.

Figure 3.3: Spin coating setup for the development of a thin film.

3.2.2.b Field Emission Scanning Electron Microscopy (FESEM) and Energy Dispersive X-ray Spectroscopy (EDX)

FESEM and EDX are essential tools in material science for detailed surface and compositional analysis of samples. FESEM, specifically the FEI INSPECT F50 model, operates by emitting a focused beam of high-energy electrons from a field emission source onto the surface of a sample.

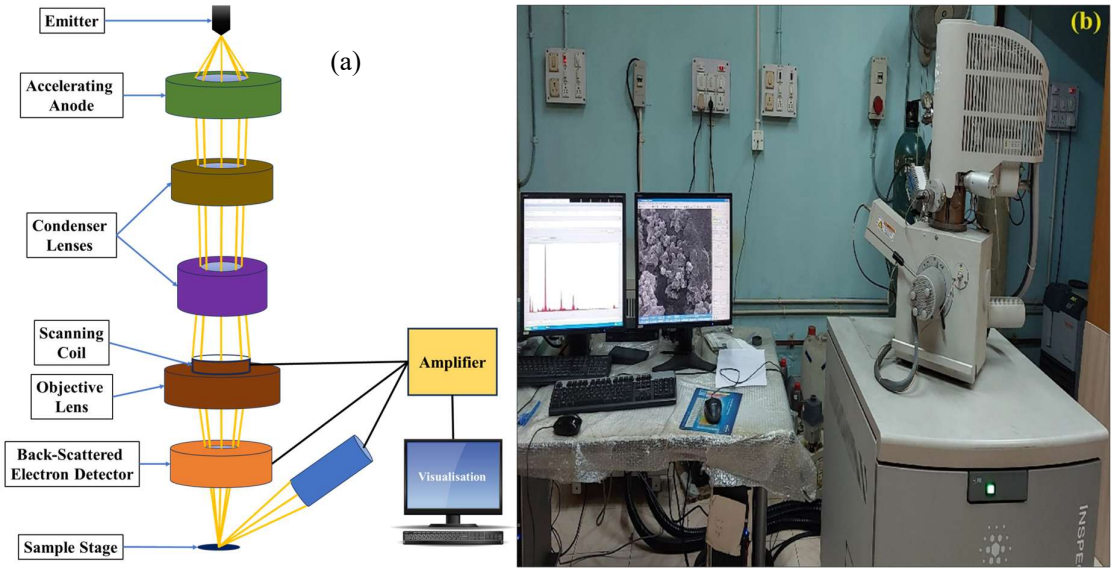

Figure 3.4: (a) Components of a FESEM, (b) digital image of FESEM FEI INSPECT F50

This interaction produces secondary and backscattered electrons as shown in **Figure 3.4(a)**, which are collected to form highly detailed images with superior resolution and depth of field, allowing for the examination of surface morphology and microstructure. In my research, the sample was prepared on a glass slide and coated with a thin layer of gold using the Quorum

Q150R ES coating system to enhance conductivity and imaging quality. The digital image of laboratory FESEM instruments is shown in **Figure 3.4(b)**. EDX, using the Bruker Quantax 200 detector, complements FESEM by providing an elemental analysis of the sample. As the electron beam from the FESEM interacts with the sample, it excites atoms within the material, causing them to emit characteristic X-rays. The EDX detector captures these X-rays and generates a spectrum that identifies and quantifies the elemental composition of the sample. Together, FESEM and EDX offer comprehensive insights into both the structural and compositional aspects of materials, making them invaluable for research in material science, including the development and analysis of new materials, quality control, and failure analysis.

3.2.2.c LCR Meter

An LCR meter is an electronic instrument used to measure the inductance (L), capacitance (C), and resistance (R) of electronic components and materials. In our work, we used the Hioki LCR Q meter (IM3536) (**Figure 3.5**) to measure the impedance spectra of samples.

Figure 3.5: Hioki LCR Q meter (IM3536)

The working mechanism of an LCR meter involves applying an alternating current (AC) signal to the sample and measuring the resulting voltage and current. The LCR meter then calculates the impedance (Z) and phase angle (θ) from these measurements. The impedance is a complex quantity that encompasses resistance (real part) and reactance (imaginary part), which is determined by the inductance and capacitance of the sample. By varying the frequency of the AC signal, the LCR meter can produce an impedance spectrum, showing how impedance changes with frequency.

3.2.2.d Keithley 2400 source Meter

The Keithley 2400 Source Measure Unit (SMU) is a versatile instrument used for precision electrical measurements, providing both sourcing and measuring capabilities in a single device. In our research, we utilised the Keithley 2400 SMU to perform accurate electrical characterisation of our samples. **Figure 3.6** shows the laboratory Keithley 2400 SMU setup used to measure electrical characterisation.

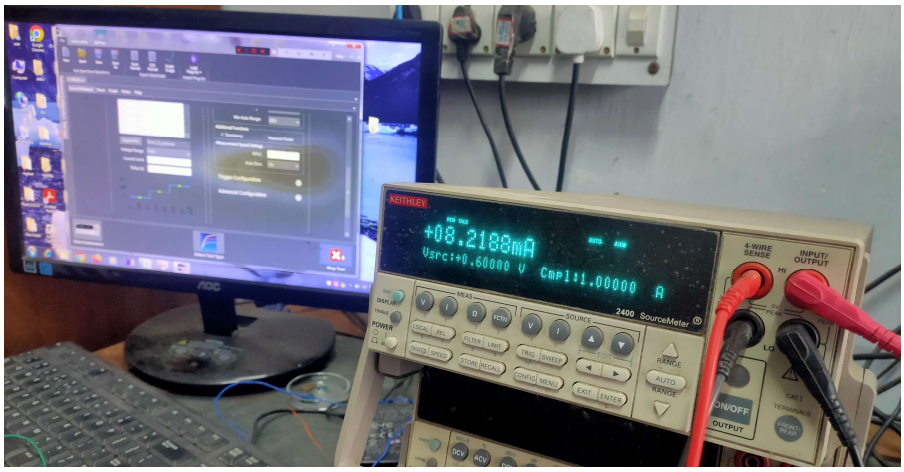

Figure 3.6: Keithley 2400 SMU with computer interface for the electrical measurements

The working mechanism of the Keithley 2400 SMU involves its ability to function as both a voltage source and a current source, as well as a voltmeter and an ammeter. It can source and measure current and voltage simultaneously, allowing for comprehensive analysis of electrical properties. The SMU can be programmed to sweep through a range of voltages or currents while continuously measuring the corresponding current or voltage, respectively. This dual functionality enables detailed characterisation of current-voltage (I-V) relationships, resistance, and other electrical parameters.

3.2.2.e Glove Box

A glove box is a sealed enclosure with built-in gloves, allowing researchers to handle materials in a controlled atmosphere, typically inert gases like nitrogen or argon, to prevent contamination or oxidation.

Figure 3.7: Self-designed laboratory glove box setup

In our research, a self-designed glove box equipped with a nitrogen (N_2) cylinder was used to synthesise lead-free tin-based perovskites. This setup is critical to ensure the integrity of the samples and prevent oxidation of tin during synthesis. The glove box setup of our laboratory is shown in **Figure 3.7**. The importance of using a glove box in material science, particularly for synthesising lead-free tin-based perovskites, lies in its ability to provide a controlled environment free from oxygen and moisture. This ensures the purity and stability of the synthesised materials, allowing for accurate characterisation and reliable results. By conducting the synthesis process in a glove box, researchers can achieve precise control over experimental conditions, leading to the development of high-quality materials with desired properties.

3.2.2.f Ultrasonic Sonicator

An ultrasonic sonicator is a high-frequency sound wave device used for dispersion, homogenization, and emulsification of particles in liquid media. It operates by generating ultrasonic waves, typically in the range of 20 kHz to several hundred kHz, which create rapid pressure changes in the liquid. These fluctuations lead to acoustic cavitation, where microscopic bubbles form, grow, and collapse violently, producing intense localised energy. This energy helps break down agglomerates of nanoparticles, ensuring uniform dispersion in solutions such as nanocomposites, colloids, and emulsions. Ultrasonic sonication is widely used in material science, chemistry, and biotechnology for tasks like nanoparticle synthesis, degassing, and breaking cell membranes in biological applications.

Figure 3.8: Ultrasonic Sonicator

In the preparation of Brilliant Blue TiO_2 PVA nanocomposites, an ultrasonic sonicator ensures the homogeneous distribution of TiO_2 nanoparticles and dye molecules in the PVA matrix, preventing sedimentation and aggregation, which is crucial for achieving a stable and uniform film.

3.2.3 Cell Preparation

This section outlines the detailed procedures involved in cell preparation, including the materials, methods, and conditions used to assemble and fabricate the cell.

3.2.1.a Electrode Cleaning Process

First, two pieces of copper and glass plates coated with Indium-Tin-Oxide (ITO) are swabbed with a mild detergent. They are rinsed with DI water after soaking in the detergent at 60°C for ten minutes. The electrodes are sonicated with DI water, 2-propanol, and acetone for 10 minutes before being placed in a nitrogen atmosphere to dry. Before being spin-coated, the sample is exposed to UV ozone for ten minutes.

3.2.1.b Preparation of Functionalised TiO_2-PVA Solution

To make the 30% PVA solution, 1 g of PVA is combined with 30 ml of deionised water using a Dhona-100DS measurement device, then stirred for an hour with a magnetic stirrer at 313K. In this process, PVA is employed as an inert binder [28]. TiO_2 nanoparticles are first dispersed in anhydrous ethanol using ultrasonication for 30 minutes to achieve uniform distribution. The dispersion is then centrifuged to eliminate aggregates. Next, 4-Phenylene di-isothiocyanate

(PDITC) is dissolved in ethanol, and the TiO_2 suspension is introduced dropwise under continuous stirring for 12-24 hours. This process allows the isothiocyanate groups of PDITC to form covalent bonds with the hydroxyl groups on the TiO_2 surface. The functionalized nanoparticles are rigorously washed with ethanol and acetone, centrifuged, and dried in a vacuum oven at 60-80°C.

3.2.1.c Preparation of Dye-TiO_2-PVA Composite

A BB dye solution is prepared by dissolving the dye in deionised water. The functionalised TiO_2 nanoparticles are then dispersed into this dye solution and ultrasonicated for 30 minutes, followed by continuous stirring for 6-12 hours to form a stable composite. The resulting TiO_2-dye composite is separated via centrifugation, washed with deionised water or ethanol to remove residual dye, and dried in a vacuum oven at 60°C until completely free of moisture.

3.2.1.d Fabrication of ITO/Dye-TiO_2/CU Schottky Cell

For device fabrication, the prepared samples are spin-coated at 1500 rpm using an APEX spin coater onto pre-cleaned ITO glass slides, which have been semi-dried in a vacuum desiccator.

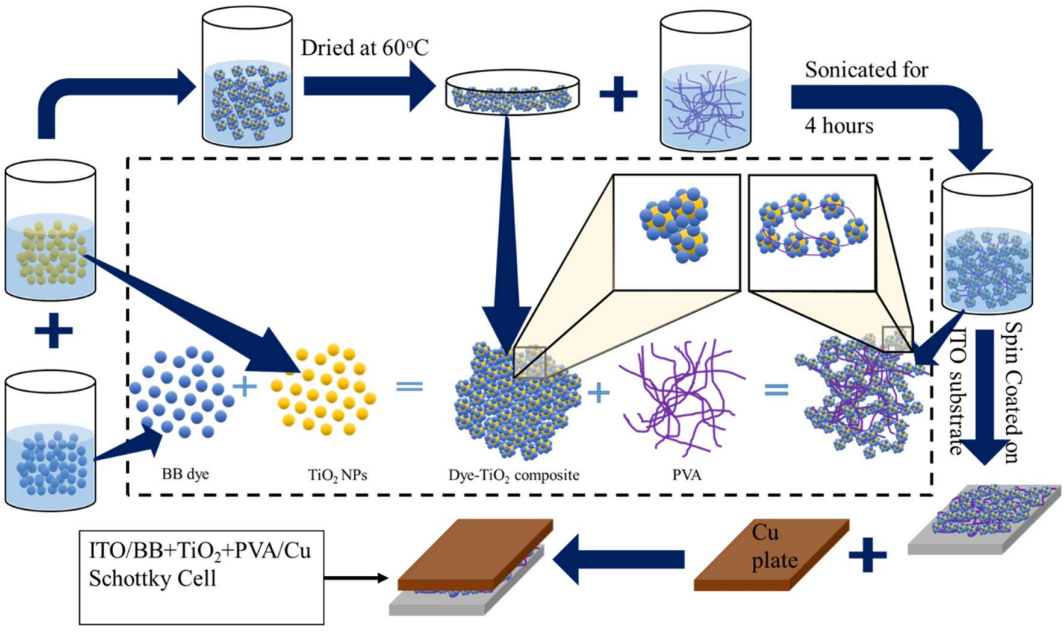

Figure 3.9: Schematic diagram of the cell preparation.

A Metal-Dye-Metal (MDM) structure is then formed by attaching a Cu plate as the back electrode. The assembled devices are stored in a vacuum under dark conditions for 12 hours to ensure complete drying before undergoing characterisation. A schematic diagram of the cell fabrication process is shown in **Figure 3.9**.

3.2.4 Characterisation

Figure 3.10(a) represents the SEM image of the prepared thin film. We can see that the composite is well-formed and well-distributed on the electrode. **Figure 3.10(b)** represents the cross-sectional SEM image. The thickness of this film was found to be approximately 950 nm.

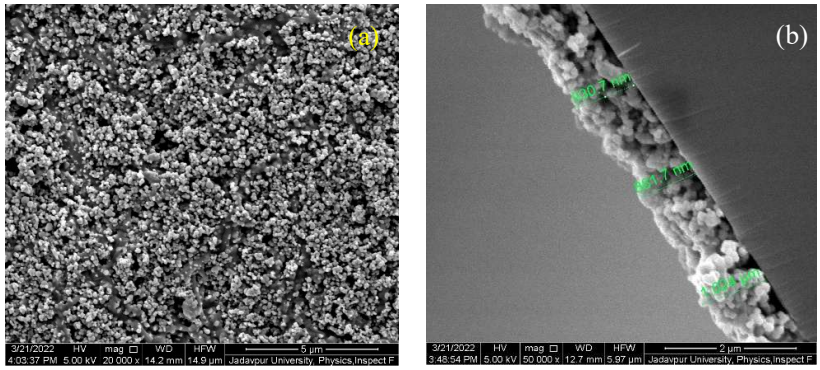

Figure 3.10:(a) SEM image of the thin film for BB-Dye incorporated with NPs. (b) Cross-sectional SEM image for the thickness of the thin film.

3.3 Result and Discussion

This section presents the results of the experiments and provides a detailed discussion and analysis of the findings, highlighting their significance and implications.

3.3.1 Dark Current-Voltage-Temperature Characteristics

The dark current-voltage-temperature (I-V-T) properties of the cells have been observed using a Keithley 2400 source unit and a Regulated Heat Source unit. An image of the thin film with an average thickness is 9.81 nm is shown with the electrode. The temperature is raised from 286K to 333 K simultaneously.

Throughout the test, the bias voltage is adjusted from 0V to 5V in 0.5V increments with a 1500 ms delay. The experiment's straightforward circuit diagram is depicted in **Figure 3.11(a)**. The

experiment was conducted in a glove box that was free of dust and at ambient temperature. The I-V-T characteristics of the prepared cells are depicted in **Figures 3.11(b)** and **3.11(c)** for dye without and with nanoparticles, respectively. An increase in conduction current is observed with rising temperature and with the incorporation of TiO_2 nanoparticles.

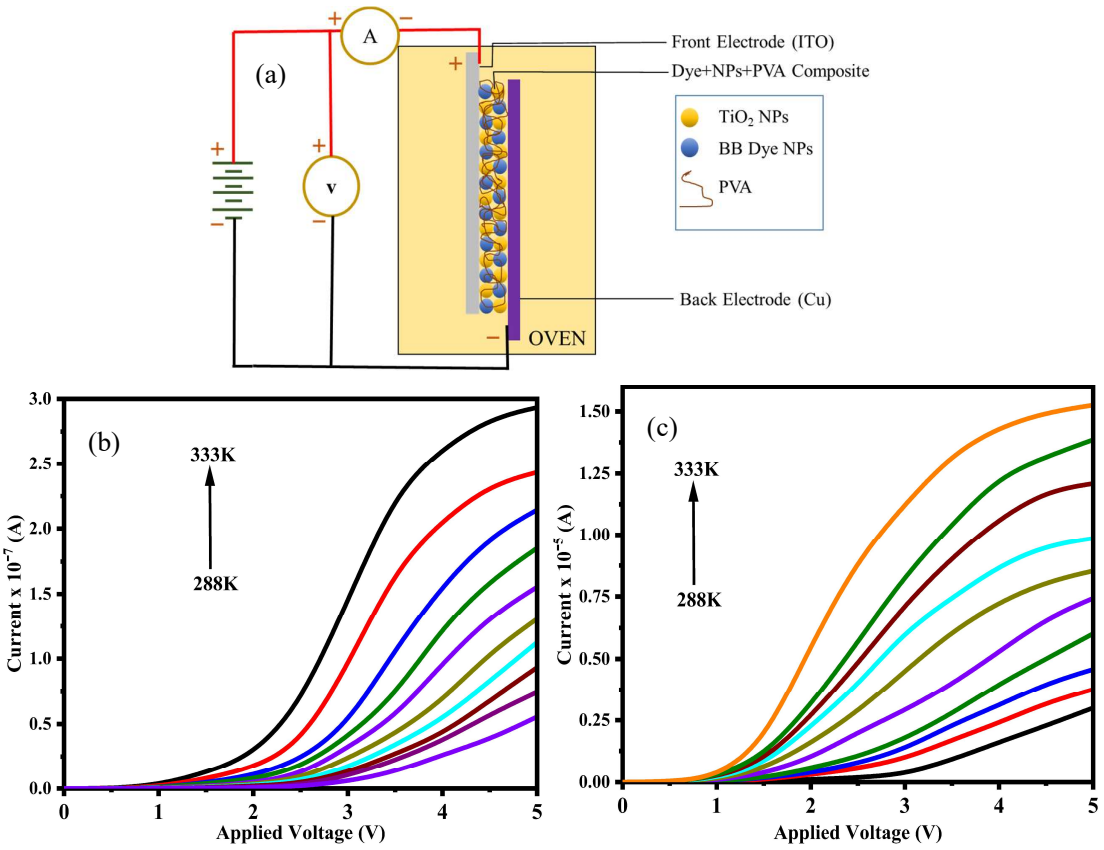

Figure 3.11: (a) Schematic circuit diagram of temperature-dependent I-V-T characteristics. I-V-T characteristics of (b) BB dye, (c) BB dye with TiO_2.

In inhomogeneous Schottky-barrier diodes (SBD), the total area contributing to current transport is dependent on temperature and bias. TiO_2 nanoparticles offer a high surface area-to-volume ratio, creating a substantial interface for dye adsorption. The increased surface area allows for a greater attachment of dye molecules, thereby enhancing device efficiency. Furthermore, TiO_2 nanoparticles exhibit excellent electron transport properties owing to their high electron mobility and low recombination rates. Electrons injected into the conduction band of TiO_2 can swiftly traverse the nanoparticle network to the electrode, minimising charge losses and, thus, amplifying overall device performance. The Richardson-Schottky thermionic

emission theory was employed to investigate the current flow [29]. A Schottky diode's forward-bias I-V-T relation can be written from the previous chapter as **Equation (2.6).**

$$I = \left[AA^*_{eff}T^2 \exp\left(\frac{-q\phi_b^{eff}}{kT}\right)\right] \exp[\frac{qV}{nkT}] \tag{3.1}$$

where q denotes the charge carrier, k the Boltzmann constant, T the temperature in Kelvin, n the ideality factor, which indicates how well a diode complies with the ideal diode equation, A the device's area, ϕ_b^{eff} the zero-bias junction's barrier height, and A^*_{eff} the effective Richardson constant. Consider I_0 as the reverse saturation current, which can be written from Equation (3.1) as. **Figure 3.12(a)** represents the variation of I_0 with respect to temperature for dye and dye with NPs, respectively.

$$I_0 = AA^*_{eff}T^2 \exp\left(\frac{-q\phi_b^{eff}}{kT}\right) \tag{3.2}$$

Taking 'ln' in Equation (3.2), we have:

$$\ln\left(\frac{I_0}{AT^2}\right) = \ln(A^*_{eff}) - q\frac{\phi_b^{eff}}{kT} \tag{3.3}$$

Figure 3.12(b) depicts the Richardson plot comparison of our cells. The extracted values of the A^*_{eff} for the BB dye in both configurations are different from the conventional value of n-type and p-type semiconductors. A reduction in the Effective Richardson Constant (A^*_{eff}) is observed from 55.59×10^{-7} $Am^{-2}K^{-2}$ to 14.87×10^{-7} $Am^{-2}K^{-2}$ by incorporation of TiO_2 nanoparticles. The modification of the Richardson Constant indicates the improvement of barrier inhomogeneity at the interface by incorporation of nanoparticles. Greater uniformity of charge flow through the junction is a result of the improvement of the inhomogeneity of the barrier potential. From Equation (3.3), we have the following **Equation (3.4)** to estimate the dependency of ϕ_{b0} with the temperature.

$$\phi_b^{eff} = \frac{kT}{q}\ln\left(\frac{AA^*_{eff}T^2}{I_0}\right) \tag{3.4}$$

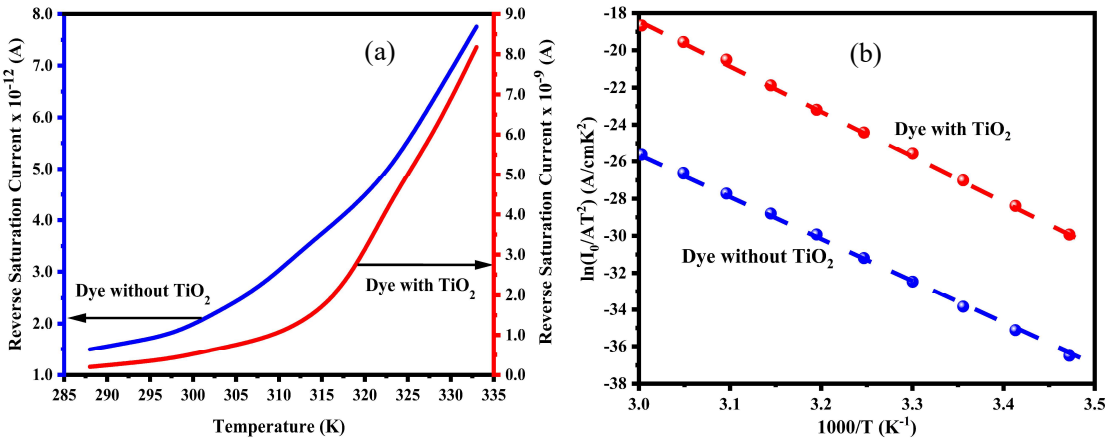

Figure 3.12: (a) The extracted plot of Dependency of I_0 with temperature and (b) Richardson plot comparison.

From Equation (3.1), we have the following **Equation (3.5)** represents the dependency of the ideality factor with the temperature.

$$n = \frac{q}{kT}\left(\frac{dV}{d\ln I}\right) \tag{3.5}$$

Figures 3.13(a) and **3.13(b)** below represent the lnI versus V plot of dye without and with nanoparticles, respectively. We can see that with a temperature rise, the barrier height rises for both devices. As the temperature drops from 333 K to 288 K, the value of ϕ_{b0} also drops from 0.77 eV to 0.73 eV for dye without nanoparticles and 0.68 eV to 0.59 eV for dye incorporated with nanoparticles. Also, the value of the ideality factor decreases with an increase in temperature. At low temperatures, electrons dominate current transport because they can overcome lower barriers, which suggests the tunnelling mechanism. The current transport across the junction is due to the thermally activated charge carriers; electrons are allowed to accumulate around the lower barrier at low temperatures causing a charge flow through the patches. **Figures 3.14(a)** and **3.14(b)** depict the dependency of ϕ_b^{eff} and n with temperature for BB dye and BB dye incorporated with TiO_2 nanoparticles respectively. As a result, we get a high ideality factor and low barrier height at low-temperature regions according to the discussion of our previous article [29,32–34]. As we increase the temperature, more and more electrons are getting thermally excited and allowed to accumulate around the higher barrier, hence we have a higher barrier height at higher temperature regions. The large values of the ideality factor are due to the deviation from thermionic emission theory in the current transport mechanism, due to the series resistance effect. There are several causes for greater ideality

factors, like the formation of a small oxide layer at the interface [35–38]. The observed variation in Figures 3.14(a) and 3.14(b) is due to the non-uniformity of interfacial charges [39].

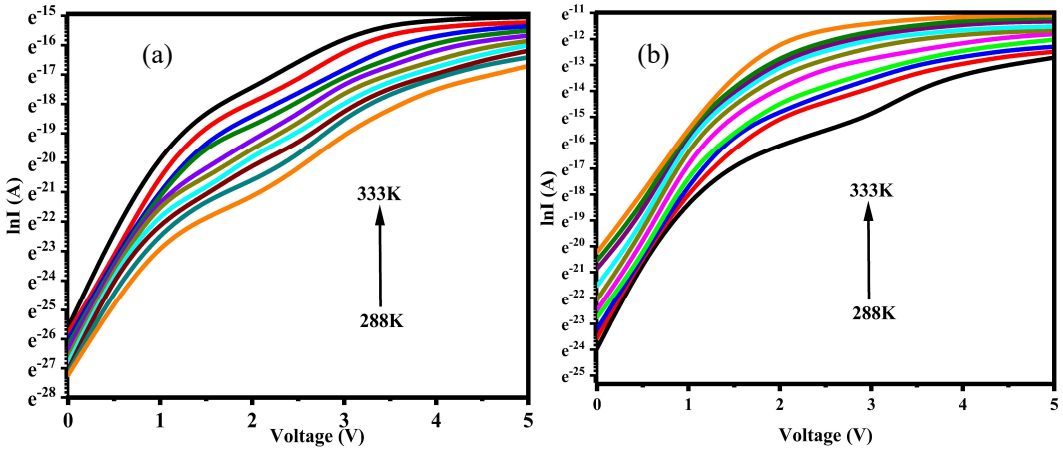

Figure 3.13: The lnI-V plot of (e) BB dye and (f) BB dye incorporated with TiO_2.

The non-uniformity of charge flow at the interface can be a cause of inhomogeneity in the barrier height at the interface. **Figure 3.14(c)** represents the graphical representation of BHI at the metal-organic contact. We can see that by the incorporation of nanoparticles, the inhomogeneity is modified, as well as the average barrier height decreases. The decrease of barrier height and ideality factor at all the temperature ranges due to the incorporation of TiO_2 nanoparticles is another crucial observation of the study. We can infer an improvement in the charge injection process in the presence of nanoparticles, which can be due to the filling of traps. By filling the traps, charge flow gets improved due to the presence of TiO_2 nanoparticles, which will also result in potential barrier lowering at the metal-organic contact. Also, we found an improvement in the ideality factor for the BB dye-based device in the presence of TiO_2 nanoparticles. The device with nanoparticles shows more ideal behaviour than the device without nanoparticles. Modification of barrier inhomogeneity at the interface can be the cause of the modification of barrier height and ideality factor in the presence of nanoparticles.

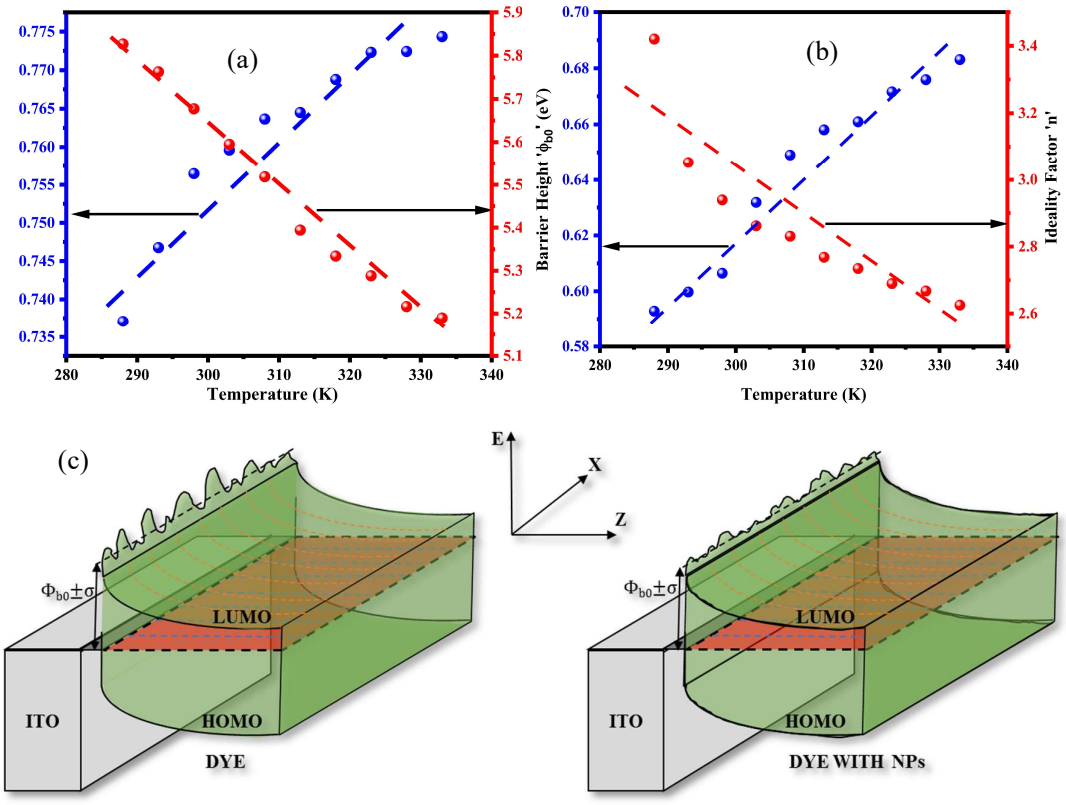

Figure 3.14: Dependency of ϕ_{b0} and n with temperature for BB dye (a) without TiO_2 nanoparticles. (b) with TiO_2 nanoparticles. (c) Representation and modification of BHI at the junction.

3.3.2 Capacitance-Voltage-Frequency Characteristics

The capacitance-voltage measurements provide knowledge about the fixed charge concentration, the potential difference between the bottom of the conduction band to the Fermi level, the built-in potential, the dielectric constant of the material, the carrier mobility, and the height of the contact junction barrier. **Figure 3.15(a)** and **3.15(b)** represent the C^{-2} versus V plot of dye without and with nanoparticles, respectively. where $€_s$ represents the dielectric constant of the dye, N_d is the donor concentration, and V_{bi} is the built–in potential. As per Equation (3.6), the C^{-2}–V plot (Figure 3.15(a) and 3.15(b)) at different frequencies will be a straight line, and by linear fitting the plot, we get the value of V_{bi} as the intercept and N_d as the slope. The C–V measurement is carried out at a sufficiently high frequency where the charge at the interface cannot follow an AC signal. Therefore, the depletion region capacitance is written as [40,41]

$$\frac{1}{C^2} = \frac{2(V_{bi}+V)}{A^2 €_s q N_d} \tag{3.6}$$

Table 3.1 below represents the frequency-dependent dielectric constant ($€_s$) and donor concentration (N_d) for the prepared devices. **Figure 3.15(c)** represents the variation of V_{bi} with respect to frequency. The built-in potential is the energy difference between the Fermi level of the metal and the Fermi level of the organic substance of a metal-organic contact. **Figure 3.16** below represents how the built-in potential develops in a metal-semiconductor junction. In our case, we consider the ITO as the metal and the BB dye with and without nanoparticles as the organic substance. From Figure 3.13(c), we can observe an increase in the V_{bi} as we increase the applied frequency of the devices. Also, we can see a decrease in the V_{bi} in the presence of TiO_2 nanoparticles for all the frequency ranges.

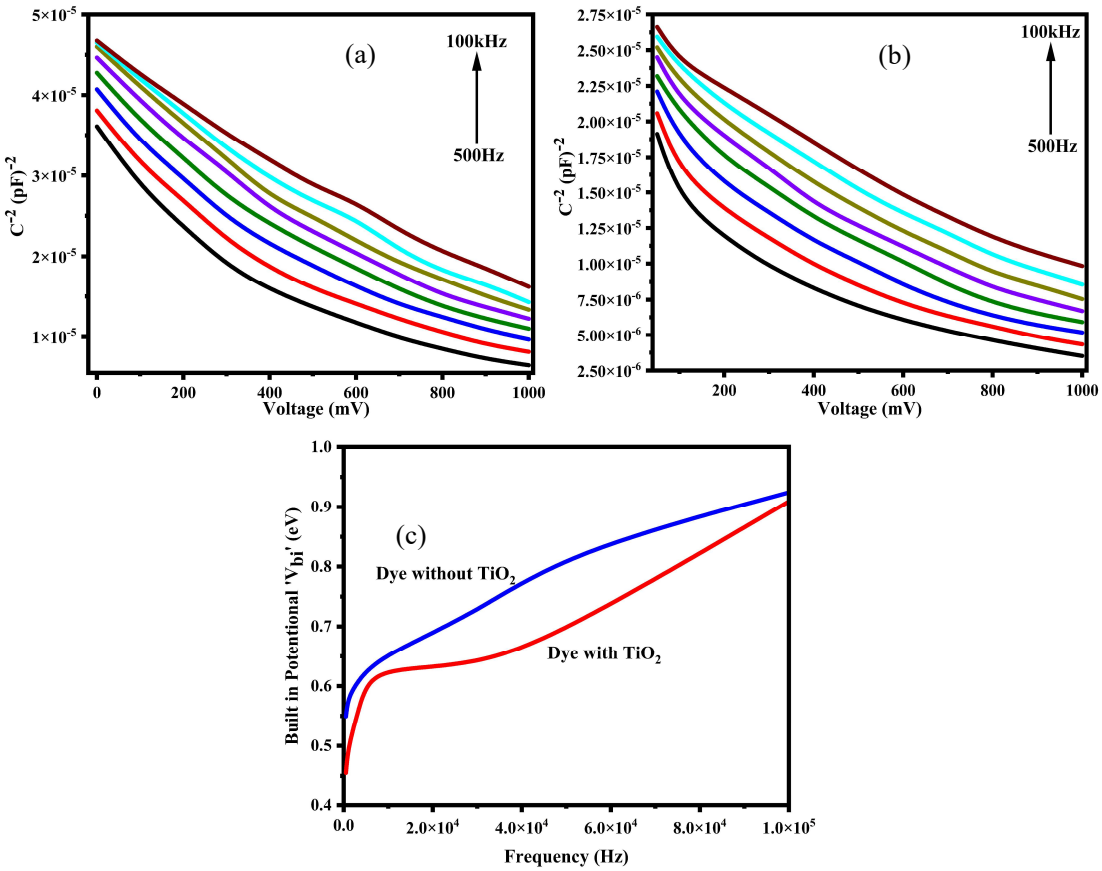

Figure 3.15: C^{-2}-V plot of (a) BB dye and (b) BB dye with TiO_2 with different frequencies. (c) Comparison of the dependency of built-in potential with respect to frequency between BB dye and BB dye with TiO_2.

Table 3.1: Dependency of $€_s$ and N_d with the frequency for BB dye with and without TiO_2 nanoparticles.

Frequency (KHz)	BB Dye without TiO_2		BB Dye With TiO_2	
	$€_s$	$N_d \times 10^{27}$ (m^{-3})	$€_s$	$N_d \times 10^{27}$ (m^{-3})
0.5	5.71	4.93	7.75	7.15
1	5.14	5.28	7.03	7.26
3	4.73	5.48	6.61	7.11
5	4.49	5.54	6.17	7.23
10	4.27	5.61	5.77	7.57
30	4.02	5.92	5.45	7.99
50	3.91	6.17	5.12	8.56
100	3.67	6.94	4.84	9.35

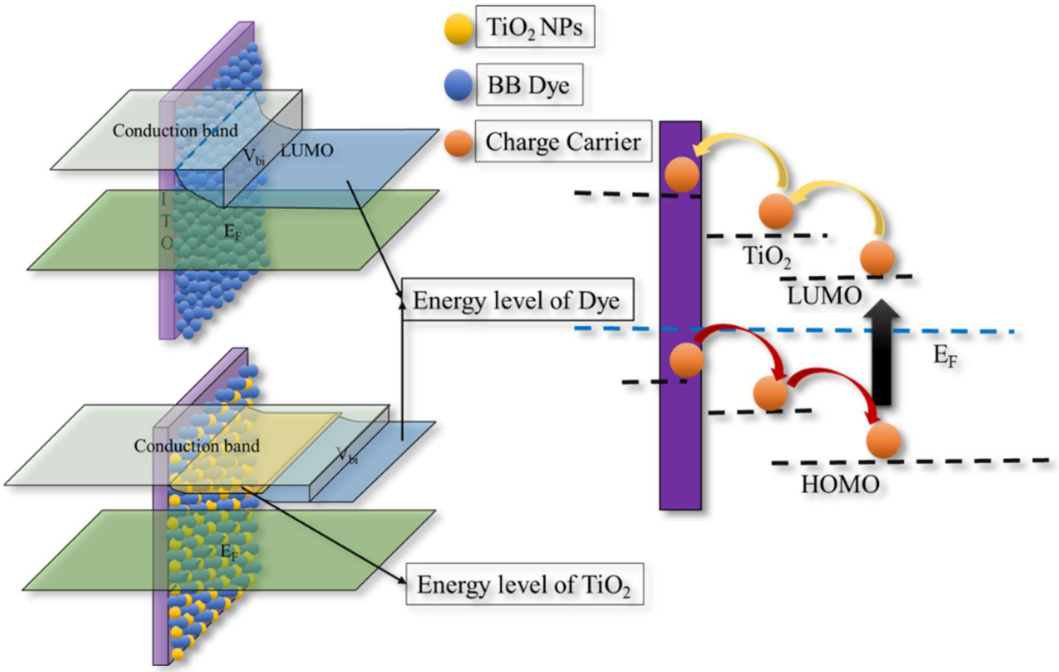

Figure 3.16: Formation of built-in potential and charge transfer process at the metal-organic interface

This can be attributed to the reduction of depletion layer width at the interface causes more electrons to overcome the barrier as we incorporate nanoparticles. The relation between the image barrier lowering ϕ_i and the maximum electric field E_m is given by **Equation 3.7** below.

$$\phi_i = \left(\frac{qE_m}{4\pi€_s}\right)^{\frac{1}{2}} \tag{3.7}$$

Again E_m can be written as

$$E_m = \left(\frac{2qV_0N_d}{4\pi\epsilon_s}\right)^{\frac{1}{2}} \quad (3.8)$$

Where V_0 is related to the V_{bi} with the following relation

$$V_{bi} = V_0 + \frac{kT}{q} \quad (3.9)$$

The depletion layer width W_L can be calculated by using the relation [40]

$$W_L = \sqrt{\frac{2\epsilon_s(V_{bi}+V)}{qN_dA^2}} \quad (3.10)$$

Figure 3.17(a) below represents the variation of E_m with frequency for with and without TiO_2 nanoparticles, and **Figure 3.17(b)** represents the dependency of W_L with the frequency for BB dye with and without TiO_2 nanoparticles. The increase in the maximum electric field with the frequency results in more charge accumulation at the interface, hence resulting in a lowering of the depletion layer with the frequency. The incorporation of nanoparticles also causes an increase in the electric field and causes a reduction of the depletion layer at the interface. The band bending in this device is completely dominated by the contacts. According to the frontier molecular orbital (FMO) theory of chemical reactivity, the transition of electrons occurs due to the interaction between the highest occupied molecular orbital (HOMO) and lowest unoccupied molecular orbital (LUMO) [42]. Band bending (V_i) can be estimated from **Equation (3.11)** as follows [1]:

$$V_i = \frac{1}{4}\left[\frac{\phi_i n}{n-1}\right] \quad (3.11)$$

The value of V_i obtained using the above Equation (3.11) is 0.134 eV for the BB dye in the absence of TiO_2 nanoparticles and 0.127 eV for the BB dye in the presence of TiO_2 nanoparticles. Modification of the LUMO level of BB dye is the most prominent conclusion for the lowering of the band bending by incorporation of TiO_2 nanoparticles. This modification is leading to an increase in the career injection at the barrier. The barrier height can also be written as **Equation 3.12** below [43]

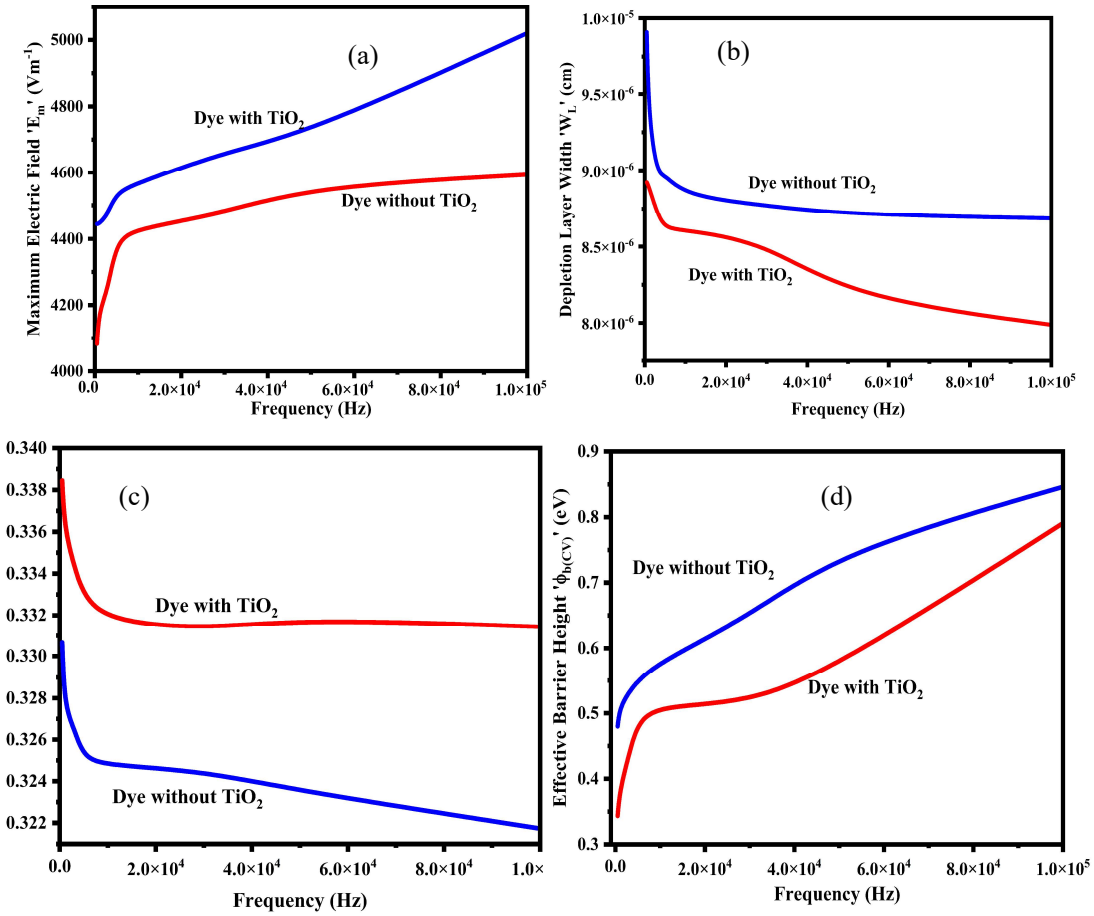

Figure 3.17: Comparison of dependency of (a) Maximum electric field and (b) depletion layer with respect to frequency between BB dye and BB dye with TiO_2 nanoparticles. Comparison of frequency-dependent (c) activation energy (V_n), (d) barrier height ($\phi_{b(CV)}$) of BB dye and BB dye with TiO_2.

$$\phi_{b(CV)} = V_{bi} + V_n - \phi_i \tag{3.12}$$

Where V_n is the potential difference between the bottom of the conduction energy level to the Fermi level, which is also known as the activation energy. The expression for the V_n is given below [44].

$$V_n = \frac{kT}{q}\ln\left(\frac{N_C}{N_d}\right) \tag{3.13}$$

Where N_c is the density of states of the conduction band of BB dye, which is given by

$$N_C = 4.20 \times 10^{15} T^{\frac{3}{2}} \left(\frac{m_e^*}{m_0}\right)^{\frac{3}{2}} \quad (3.14)$$

Where m_e^* is the effective mass of the electron and m_0 is the rest mass of the electron. The relation between m_e^* with the effective Richardson constant (A_{eff}^*) is given below [45].

$$A_{eff}^* = \frac{4\pi q m_e^* k^2}{h^3} \quad (3.15)$$

The value of N_C was found to be 2.23 × 10^{22} cm^{-3} for dye and 6.63 × 10^{24} cm^{-3} for dye incorporated with TiO_2 nanoparticles. By replacing the value of N_C and $N_d$we have calculated the value of V_n for different frequencies, and the variation of V_n with frequency is given in the following **Figure 3.17(c)**. Considering the concentration of N_d is constant over the whole area, we obtained to calculate the barrier height value using the C^2-V plot (Figure 3.15(a) and 3.15(b)) and by using Equation (3.13), we have calculated the $\phi_{b(CV)}$for different frequencies, and the dependency is depicted in **Figure 3.17(d)**.

3.3.3 Analysis of Barrier Inhomogeneity Parameters

It has been established that BHI can have a considerable impact on estimates of A_{eff}^* as well as the extracted barrier height and ideality factor [29,35,46,47]. Considering that barrier height inhomogeneity has a Gaussian distribution with a mean barrier height ϕ_b we can write the following expression for the Gaussian distribution of barrier heights as **Equation (3.16)** below [35,48,49],

$$\phi_{b0} = \phi_b - \frac{q\zeta^2}{2kT} \quad (3.16)$$

The slope and intersection from the plot of ϕ_{b0} with $\frac{1000}{T}$ give us the value of σ and, ϕ_b respectively. **Figure 3.18** represents the dependency of ϕ_{b0} with $\frac{1000}{T}$ for BB dye and BB dye incorporated with TiO_2, which is extracted from the I-V-T measurement. By linear fitting the plot, we get the value of the mean barrier height ϕ_b as the intercept and the standard deviation σ as the slope. The value of ϕ_b and σ are depicted in **Table 3.2** below. The standard deviation measures the inhomogeneity of the barrier and shows that there are Gaussian distributions of

barrier heights at the ITO/Dye-TiO_2/Cu heterojunction contact. Particularly at low temperatures, the heterojunction's transport mechanism is modified by the Gaussian distributions of barrier heights and potential fluctuations. Also, we can observe the lowering of the mean barrier height ϕ_b by incorporation of TiO_2 nanoparticles. Now we know that barrier height is the slope of the Richardson plot. Thus we can write

$$\phi_{b0} = \phi_b - \left[\left(\frac{8C_1\beta\pi\zeta^4}{9}\right)\exp\left(\frac{q^2\beta^2\zeta^2}{2k^2T^2}\right)\right]\frac{q}{kT} \tag{3.21}$$

Comparing Equation (2.15) from the previous chapter with Equation (3.21) we can express the effective Richardson Constant as

$$\ln(A^*_{eff}) = \ln A^* + \left(\frac{q}{kT} - \frac{kT}{q\beta^2\zeta^2}\right)(\phi_{b0} - \phi_b) \tag{3.22}$$

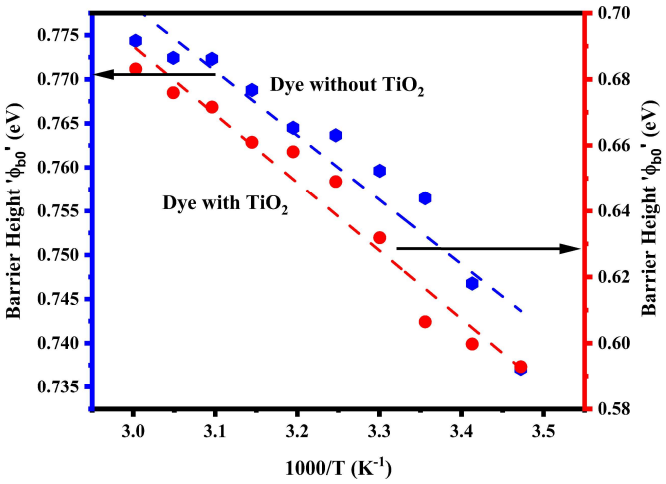

Figure 3.18: ϕ_{b0} versus $\frac{1000}{T}$ plot of BB dye and BB dye with TiO_2.

Table 3.2: Extracted value of patch parameter σ and mean barrier height ϕ_b for BB dye with and without TiO_2 nanoparticles.

Cell Configuration	Standard Deviation "ζ" (V)	Mean Barrier Height "ϕ_b" (eV)
Dye	0.18	0.89
Dye + TiO_2	0.11	0.75

Putting the values of ϕ_{b0}, ϕ_b, β, ζ, and A^*_{eff} in the above Equation (3.22), we have the value of the homogeneous Richardson constant for our prepared devices, and the values are depicted in **Table 3.3** below. We can see that the modified Richardson constant value is improved by the incorporation of TiO_2 nanoparticles. The TiO_2 nanoparticles carry a net negative charge on their surface, while the organic dye molecules typically have positive charges. This electrostatic interaction between the positively charged dye and the negatively charged TiO_2 surface aids in stabilising the dye molecules on the electrode. It improves the binding strength between the dye and the TiO_2, facilitating efficient charge transfer and reducing the barrier height as well as the inhomogeneity at the interface.

Table 3.3: Modified homogeneous A^* value of BB dye with and without TiO_2 nanoparticles.

Cell Configuration	**Homogeneous Richardson Constant (A^*) ($Am^{-2}K^{-2}$)**
DYE	81.63×10^{-5}
DYE + TiO_2	22.85×10^{-5}

3.4 Conclusion

This chapter investigates the barrier inhomogeneity of Brilliant-Blue dye, a natural fruit dye, both with and without titanium dioxide nanoparticles. The I-V-T characteristics show that as temperature increases, the zero-bias barrier height rises while the ideality factor decreases. The non-linear temperature dependence of the barrier height indicates inhomogeneity, with an average value of 0.89 eV. When nanoparticles are introduced, the mean barrier height decreases to 0.75 eV, as determined through a Gaussian distribution analysis. The reduction of standard deviation from 0.18 V to 0.11 V highlights an improvement in barrier inhomogeneity, facilitating greater charge injection at the metal-organic interface. The C^{-2}-V plot suggests the presence of interface state effects due to an increased slope. Using C-V-F and I-V-T measurements, the homogeneous Richardson constant is estimated via Tung's equation, showing enhancement with the incorporation of nanoparticles. This further confirms that nanoparticles improve barrier inhomogeneity, leading to higher conductivity. These findings are valuable for future studies on BB dye-based electronic devices.

3.5 References

[1] R. Nouchi, Extraction of the Schottky parameters in metal-semiconductor-metal diodes from a single current-voltage measurement, J Appl Phys 116 (2014). https://doi.org/10.1063/1.4901467.

[2] H. Sheng, S. Muthukumar, N.W. Emanetoglu, Y. Lu, Schottky diode with Ag on (11$\bar{2}$0) epitaxial ZnO film, Appl Phys Lett 80 (2002) 2132–2134. https://doi.org/10.1063/1.1463700.

[3] S.K. Tripathi, M. Sharma, Analysis of the forward and reverse bias I-V and C-V characteristics on Al/PVA:n-PbSe polymer nanocomposites Schottky diode, J Appl Phys 111 (2012). https://doi.org/10.1063/1.3698773.

[4] L. Changshi, A Forward Current-Voltage-Temperature Method for Extraction of Intrinsic Schottky Barrier Height, ECS Journal of Solid State Science and Technology 9 (2020) 064007. https://doi.org/10.1149/2162-8777/aba4f3.

[5] J.H. Werner, H.H. Güttler, Barrier inhomogeneities at Schottky contacts, J Appl Phys 69 (1991) 1522–1533. https://doi.org/10.1063/1.347243.

[6] N.A. Al-Ahmadi, Schottky barrier inhomogeneities at the interface of different epitaxial layer thicknesses of n-GaAs/Ti/Au/Si: Al0.33Ga0.67As, Heliyon 6 (2020) e04852. https://doi.org/10.1016/j.heliyon.2020.e04852.

[7] H.G. Çetinkaya, M. Yıldırım, P. Durmuş, Altındal, Correlation between barrier height and ideality factor in identically prepared diodes of Al/Bi4Ti3O12/p-Si (MFS) structure with barrier inhomogeneity, J Alloys Compd 721 (2017) 750–756. https://doi.org/10.1016/j.jallcom.2017.06.037.

[8] H. Cetin, B. Şahin, E. Ayyildiz, A. Türüt, The barrier-height inhomogeneity in identically prepared H-terminated Ti/p-Si Schottky barrier diodes, Semicond Sci Technol 19 (2004) 1113–1116. https://doi.org/10.1088/0268-1242/19/9/007.

[9] B.H. Moon, G.H. Han, H. Kim, H. Choi, J.J. Bae, J. Kim, Y. Jin, H.Y. Jeong, M.K. Joo, Y.H. Lee, S.C. Lim, Junction-Structure-Dependent Schottky Barrier Inhomogeneity and Device Ideality of Monolayer MoS2 Field-Effect Transistors, ACS Appl Mater Interfaces 9 (2017) 11240–11246. https://doi.org/10.1021/acsami.6b16692.

[10] aziza salah-eldin, D. Abd-Allah, Amerolative Influence of Chamomile (Matricaria recutita L.) on Synthetic Food Additive Induced Probable Toxicity in Male Albino Rats التأثير المخفف للبابونج علي السمية المحتملة للمضافات الغذائية الصناعية في ذكور الجرذان البيضاء, Journal of Food and Dairy Sciences 12 (2021) 161–170. https://doi.org/10.21608/jfds.2021.80037.1022.

[11] J.G.S. Ali, Mohammad Farhat Ali. Bassam M. EI, Handbook of Industrial Organic Chemistry, 1906.

[12] S.K. Singh, S. Kaur, Advances in Horticultural Crop Management and Value Addition, (2019).

[13] G.B. Smejkal, The Coomassie chronicles: Past, present and future perspectives in polyacrylamide gel staining, Expert Rev Proteomics 1 (2004) 381–387. https://doi.org/10.1586/14789450.1.4.381.

[14] P.S. Ganesh, S.Y. Kim, S. Kaya, R. Salim, G. Shimoga, S.H. Lee, Quantum chemical studies and electrochemical investigations of polymerized brilliant blue-modified carbon paste electrode for in vitro sensing of pharmaceutical samples, Chemosensors 9 (2021). https://doi.org/10.3390/chemosensors9060135.

[15] M. Maity, S. Dolui, N.C. Maiti, Hydrogen bonding plays a significant role in the binding of coomassie brilliant blue-R to hemoglobin: FT-IR, fluorescence and molecular dynamics studies, Physical Chemistry Chemical Physics 17 (2015) 31216–31227. https://doi.org/10.1039/c5cp04661k.

[16] Y. Cao, J. Zhao, Y.L. Xiong, Coomassie Brilliant Blue-binding: A simple and effective method for the determination of water-insoluble protein surface hydrophobicity, Analytical Methods 8 (2016) 790–795. https://doi.org/10.1039/c5ay02630j.

[17] Y.S. Li, Y.S. Ge, Y. Zhang, A.Q. Zhang, S.F. Sun, F.L. Jiang, Y. Liu, Interaction of coomassie brilliant blue G250 with human serum albumin: Probing of the binding mechanism and binding site by spectroscopic and molecular modeling methods, J Mol Struct 968 (2010) 24–31. https://doi.org/10.1016/j.molstruc.2010.01.015.

[18] A. Liang, Z. Lu, Q. Liu, X. Zhang, G. Wen, Z. Jiang, SERS quantitative analysis of trace HSA with a Coomassie brilliant blue G-250 molecular probe in nanogold sol substrate, RSC Adv 5 (2015) 5711–5715. https://doi.org/10.1039/c4ra11778f.

[19] E. Brunelle, A.M. Le, C. Huynh, K. Wingfield, L. Halámková, J. Agudelo, J. Halámek, Coomassie Brilliant Blue G-250 Dye: An Application for Forensic Fingerprint Analysis, Anal Chem 89 (2017) 4314–4319. https://doi.org/10.1021/acs.analchem.7b00510.

[20] P. Sanjay, K. Deepa, J.M. Shyla, J. Madhavan, S. Senthil, Performance of TiO 2 Based Dye-Sensitized Solar Cells Fabricated Using Coomassie Brilliant Blue in Acetonitrile Solution, 2019. www.sciencedirect.comwww.materialstoday.com/proceedings.

[21] P. Srivastava, L. Bahadur, Dye-sensitized solar cell based on nanocrystalline ZnO thin film electrodes combined with a novel light absorbing dye Coomassie Brilliant Blue in acetonitrile solution, Int J Hydrogen Energy 37 (2012) 4863–4870. https://doi.org/10.1016/j.ijhydene.2011.12.064.

[22] M.S. Salem, A.R. Wassel, M. Fedawy, A. Shaker, A.H. Al-Bagawia, G.M. Aleid, A.M. El-Mahalawy, Integration of biocompatible Coomassie Brilliant Blue dye on

silicon in organic/Inorganic heterojunction for photodetection applications, Journal of Physics and Chemistry of Solids 169 (2022). https://doi.org/10.1016/j.jpcs.2022.110890.

[23] A. Rózycka, K.A. Bogdanowicz, N. Górska, J. Rysz, M. Marzec, A. Iwan, R. Pich, A. Januszko, Influence of TiO2 nanoparticles on liquid crystalline, structural and electrochemical properties of (8z)-n- (4-((z)-(4-pentylphenylimino)methyl)benzylidene)- 4-pentylbenzenamine, Materials 12 (2019) 1–17. https://doi.org/10.3390/ma12071097.

[24] L.W. Zhang, H.B. Fu, Y.F. Zhu, Efficient TiO2 photocatalysts from surface hybridization of TiO2 particles with graphite-like carbon, Adv Funct Mater 18 (2008) 2180–2189. https://doi.org/10.1002/adfm.200701478.

[25] A. Rózycka, A. Iwan, K.A. Bogdanowicz, M. Filapek, N. Górska, D. Pociecha, M. Malinowski, P. Fryn, A. Hreniak, J. Rysz, P. Dabczynski, M. Marzec, Synthesis and characterization of two new TiO2-containing benzothiazole-based imine composites for organic device applications, Beilstein Journal of Nanotechnology 9 (2018) 721–739. https://doi.org/10.3762/bjnano.9.67.

[26] M.N. Solovan, P.D. Maryanchuk, V. V. Brus, O.A. Parfenyuk, Electrical and optical properties of TiO 2 and TiO 2:Fe thin films, Inorganic Materials 48 (2012) 1026–1032. https://doi.org/10.1134/S0020168512100123.

[27] S. Di Mo, W.Y. Ching, Electronic and optical properties of three phases of titanium dioxide: Rutile, anatase, and brookite, Phys Rev B 51 (1995) 13023–13032. https://doi.org/10.1103/PhysRevB.51.13023.

[28] Y.C. Tsai, J.D. Huang, C.C. Chiu, Amperometric ethanol biosensor based on poly(vinyl alcohol)-multiwalled carbon nanotube-alcohol dehydrogenase biocomposite, Biosens Bioelectron 22 (2007) 3051–3056. https://doi.org/10.1016/j.bios.2007.01.005.

[29] R.T. Tung, Electron transport at metal-semiconductor interfaces: General theory, Phys Rev B 45 (1992) 13509–13523.

[30] A. Kanti Karan, N.B. Manik, Estimation of Richardson Constant for Natural Organic dye Based Cells using Orange-lemon and Apple-green, 2021.

[31] A.K. Karan, D. Sahoo, S. Sen, N.B. Manik, Evaluation of Richardson Constant of Fruit dyes using Carmoisine and Tartrazine, International Journal of Innovative Research in Physics 3 (2022) 25–31. https://doi.org/10.15864/ijiip.3404.

[32] A. Gümüs, A. Türüt, N. Yalçin, Temperature dependent barrier characteristics of CrNiCo alloy Schottky contacts on n-type molecular-beam epitaxy GaAs, J Appl Phys 91 (2002) 245–250. https://doi.org/10.1063/1.1424054.

[33] R.T. Tung, Electron transport of inhomogeneous Schottky barriers, Appl Phys Lett 58 (1991) 2821–2823. https://doi.org/10.1063/1.104747.

[34] A.K. Karan, Effect of Titanium-Dioxide nanoparticle on Richardson Constant and Barrier Height of Tartrazine Dye based Schottky Device, Discov Mater (2023) 0–11. https://doi.org/10.1007/s43939-023-00040-y.

[35] J.H. Werner, H.H. Güttler, Barrier inhomogeneities at Schottky contacts, J Appl Phys 69 (1991) 1522–1533. https://doi.org/10.1063/1.347243.

[36] J.H. Werner, H.H. Güttler, Temperature dependence of Schottky barrier heights on silicon, J Appl Phys 73 (1993) 1315–1319. https://doi.org/10.1063/1.353249.

[37] Ş. Aydoğan, M. Sağlam, A. Türüt, On the barrier inhomogeneities of polyaniline/p-Si/Al structure at low temperature, Appl Surf Sci 250 (2005) 43–49. https://doi.org/10.1016/j.apsusc.2004.12.020.

[38] S.M. Sze, Semiconductor Device Development in the 1970's and 1980's—A Perspective, Proceedings of the IEEE 69 (1981) 1121–1131. https://doi.org/10.1109/PROC.1981.12127.

[39] M.H. Suhail, G.M. Rao, S. Mohan, Dc reactive magnetron sputtering of titanium-structural and optical characterization of TiO2 films, J Appl Phys 71 (1992) 1421–1427. https://doi.org/10.1063/1.351264.

[40] M. Sharma, S.K. Tripathi, Study of barrier inhomogeneities in I-V-T and C-V-T characteristics of Al/Al 2O 3/PVA:n-ZnSe metal-oxide-semiconductor diode, J Appl Phys 112 (2012). https://doi.org/10.1063/1.4737589.

[41] Ö. Güllü, Ş. Aydoğan, A. Türüt, High barrier Schottky diode with organic interlayer, Solid State Commun 152 (2012) 381–385. https://doi.org/10.1016/j.ssc.2011.12.007.

[42] K. Fukui, Theory of Orientation and Stereoselecdon, (n.d.).

[43] O. Pakma, N. Serin, T. Serin, On the energy distribution profile of interface states obtained by taking into account of series resistance in Al / TiO 2 / p – Si (MIS) structures, Physica B: Physics of Condensed Matter 406 (2011) 771–776. https://doi.org/10.1016/j.physb.2010.11.078.

[44] Y. Chen, C. Huang, J.S. Cells, T. Cheng, S. Lin, S. Nishida, J. Liang, Frequency and voltage dependence of electric and dielectric properties of Au / TiO 2 / type Schottky barrier diodes, (n.d.). https://doi.org/10.1088/0031-8949/90/9/095801.

[45] C.R. Crowell, The Richardson constant for thermionic emission in Schottky barrier diodes, Solid State Electronics 8 (1965) 395–399. https://doi.org/10.1016/0038-1101(65)90116-4.

[46] F. Roccaforte, F. La Via, V. Raineri, R. Pierobon, E. Zanoni, Richardson ' s constant in inhomogeneous silicon carbide Schottky contacts Richardson ' s constant in inhomogeneous silicon carbide Schottky contacts, 9137 (2012). https://doi.org/10.1063/1.1573750.

[47] S. Chand, J. Kumar, Effects of barrier height distribution on the behavior of a Schottky diode, 5005 (1998).

[48] A. Dey, S. Middya, R. Jana, M. Das, J. Datta, A. Layek, P.P. Ray, Light induced charge transport property analysis of nanostructured ZnS based Schottky diode, Journal of Materials Science: Materials in Electronics 27 (2016) 6325–6335. https://doi.org/10.1007/s10854-016-4567-5.

[49] S. Chand, J. Kumar, On the existence of a distribution of barrier heights in Pd 2 Si / Si Schottky diodes, 288 (2014).

CHAPTER 4

Modification Of Activation-Energy-Levels by the Incorporation of Zinc-Oxide Nanoparticles in Sunset Yellow Dye-Based Organic-Cell

Table of Contents

4.1 Introduction

In the previous chapter, we discussed about the barrier height, band bending, and how the inhomogeneous distribution of the barrier height affects the conductivity of the organic dye-based cell. Also, we have established a relation between the Richardson constant and the inhomogeneity parameter. We also learned how the incorporation of nanoparticles can reduce the inhomogeneity in the barrier height, causing an increase in the overall current.

In this chapter, we will discuss about the activation energy levels of organic dye-based cells and the behaviour of the Fermi energy state by the incorporation of nanoparticles. Here we have used Sunset-Yellow (SY) dye as an active material and Zinc-Oxide nanoparticles as an incorporating agent. SY dye is one of the azo dyes, which is a man-made compound distinguished by one (mono azo) or multiple intramolecular 'N=N' bonds. These dyes are commonly present in a diverse array of food items, including Cheetos, Sunkist soda beverages, cheese products, and confectioneries. In recent years, organic dyes have garnered significant attention due to their biocompatibility, cost-effectiveness, and ease of synthesis [1,2]. Their versatility in various processing methods, combined with excellent film-forming abilities, tunable colours, and high absorption coefficients in the visible spectrum, has attracted considerable interest from researchers [3–6]. However, as previously discussed, limited research exists on the conductivity of natural and organic dyes [1,7–14]. The primary challenge in using these dyes for electronic and optoelectronic applications is their low conductivity. A thorough analysis of the charge transport mechanism in organic dye-based devices is essential to improve conduction. As we have stated in our earlier chapter, integrating organic dyes with polymers and nanoparticles (NPs) can enhance the overall performance of such organic dye-based devices. Here we use Zinc-Oxide (ZnO) NPs, an n-type wide bandgap semiconductor known for its low production cost and high-temperature stability, as an incorporating material. ZnO NPs have been utilised to improve the morphology and efficiency of sandwiched organic devices [15–19]. Its chemical stability and biocompatibility make it useful in various applications like gas sensors, photocatalysis, and photovoltaic cells [20–25]. Incorporating such NPs can enhance light absorption, charge separation, and collection in these devices, but detailed analysis is necessary to further improve efficiency and charge transport. We have used a sandwich structure, with Indium-Tin-Oxide (ITO) coated glass as the front electrode, a copper plate as the back electrode, and a dye-NPs blend (1:1 ratio) between the electrodes. The structural property was confirmed by the X-ray diffraction (XRD) analysis and morphological

study by Field-emission-Scanning-electron-microscopy (FESEM) analysis. DC conductivity was measured using an Agilent-4294A Impedance spectrometer over a temperature range of 288K to 333K (15°C to 60°C). AC conductivity was also measured within the same temperature range, with frequencies varying between 500 Hz and 100 kHz. Capacitance Voltage property measurements were used to study the interfacial property analysis. Photosensitivity of the cell was studied to analyse the photo-voltaic effect of the cells.

4.2 Experiment

This section provides a detailed overview of the experimental techniques, including the materials employed, instruments utilised, and related procedures.

4.2.1 Materials

Sulfanilic acid ($C_6h_7NO_3S$) (99.99% purity), $NaNO_3$ (99%), Sodium Carbonate (Na_2CO_3) (99%), and Hydrochloric acid (HCl) (98%) were purchased from Sigma Aldrich. 2-Naphthol-6-sulfonic acid ($C_{10}H_8O_4S$) (>98%), Zinc-Oxide (ZnO) (99%), Dimethylformamide (DMF) (>98%), and Polyvinyl alcohol (PVA) (>98%) were purchased from Merck (India). All the chemicals were used without further purification. The deionised water used in the experiment was collected from the departmental Milli(Q) water plant.

4.2.2 Instruments

The instruments used in this work are mostly the same as those described in Chapter 3, with the exception of XRD and UV-Vis analysis. A detailed description of all the instruments can be found in Chapter 4. In the following section, a detailed description is provided only for XRD and UV-Vis.

4.2.2.a Bruker's X-ray Diffractometer (XRD)

XRD systems are advanced instruments used in material science to analyse the crystallographic structure of materials. The working principle involves directing X-rays at a material sample and measuring the intensity and angle of the X-rays that are diffracted by the crystal lattice within the sample. In Bruker's instruments, it operates by directing X-rays, with a wavelength of 1.5406 Å, at a powdered/film sample (**Figure 4.1(a)**). As the X-rays interact with the crystal lattice, they are diffracted at specific angles, creating a diffraction pattern unique to the material's atomic structure. The resulting data is used to identify phases, determine crystallite

size, and assess structural properties. In my research, all XRD measurements were performed using the Bruker D-8 Advance, complemented by high-resolution data from the PETRA III beamline P 2.2 at DESY, Germany, with a shorter wavelength of 0.2074 Å. This combination of instruments provides comprehensive and precise crystallographic information, essential for the development and characterisation of advanced materials. **Figure 4.1(b)** shows the digital photograph of the Bruker D-8 Advance diffractometer used in our study.

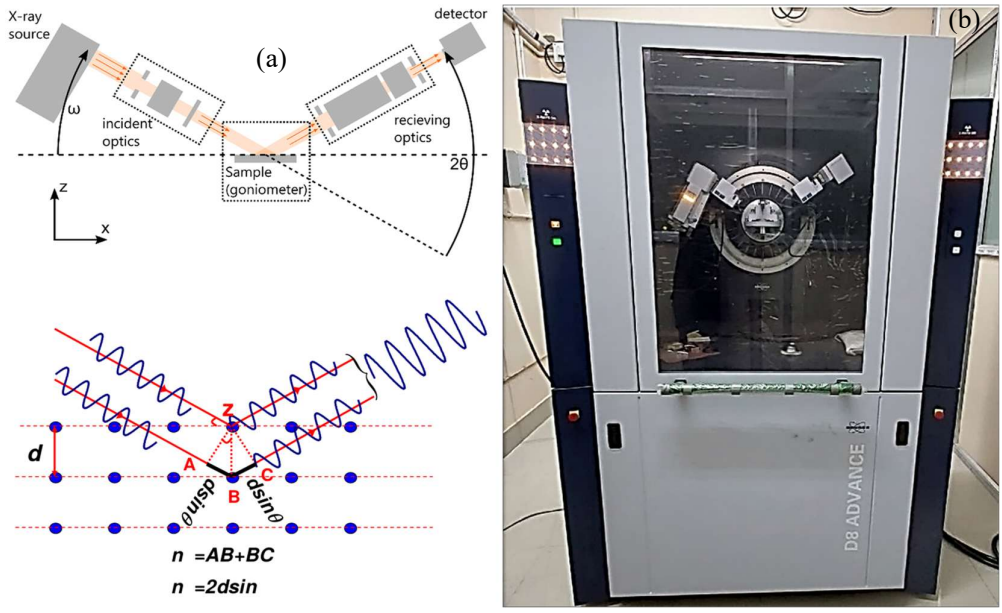

Figure 4.1: (a) Components of a diffractometer, (b) schematic diagram of the working of X-ray diffraction (XRD), (c) displays the X-ray powder diffractometer (Bruker D 8 Advance)

4.2.2.b UV-Vis. Spectrophotometer

UV-Vis. spectrophotometer is a widely used analytical technique in material science for investigating the optical properties of materials, particularly thin films. This method involves measuring the absorption and transmission of ultraviolet and visible light by a sample. In the case of the SHIMADZU Ultraviolet-Visible spectrophotometer (UV-1900, **Figure 4.2**) used in this work, the instrument directs a beam of light across the UV-Vis spectrum (typically 190-1100 nm) through the sample. The spectrophotometer then detects the amount of light absorbed or transmitted at each wavelength. The working mechanism involves a light source that emits a broad spectrum of UV and visible light. This light passes through a monochromator, which isolates individual wavelengths. The selected wavelength of light then passes through the

sample, and the detector measures the intensity of light that passes through. The difference in intensity between the incident light and the transmitted light is used to calculate the absorbance.

Figure 4.2: Shows the digital image of the UV-Vis spectrophotometer

In material science, UV-Vis. spectroscopy is essential for determining the optical band gap of semiconductors, analysing the composition and quality of thin films, and studying the electronic transitions within materials. It helps in understanding the interaction of light with the material, which is critical for applications in photovoltaics, sensors, and optoelectronic devices. Using the SHIMADZU UV-1900, precise measurements of thin films can be conducted to evaluate their optical properties, aiding in the development and optimisation of new materials.

4.2.3 Preparation of Cell

This section outlines the detailed procedures involved in cell preparation, including the materials, methods, and conditions used to assemble and fabricate the cell.

4.2.3.a Electrode Cleaning Process

The method of electrode cleaning the almost the same as we discussed in Chapter 3. Initially, two copper sheets and glass substrates coated with Indium-Tin-Oxide (ITO) are cleaned using a mild detergent. After soaking in the detergent at 60°C for ten minutes, they are rinsed thoroughly with deionised (DI) water. The electrodes then undergo ultrasonic cleaning in DI water, 2-propanol, and acetone, each for 10 minutes. Following this, they are dried under a nitrogen atmosphere. Just before spin-coating, the samples are treated with UV ozone for ten minutes.

4.2.3.b Synthesis and Purification of SY dye

The synthesis of azo dyes involves coupling an aromatic diazonium salt with electron-rich aromatic compounds. This coupling reaction can be conducted under basic, neutral, or weakly acidic conditions. The synthesis of this dye involves a two-step process [26]. Initially, 4-aminobenzenesulfonic acid undergoes conversion to 4-sulfobenzenediazonium. **Figure 4.3(a)** elucidates the chemical reaction for SY dye synthesis, while **Figure 4.3(b)** illustrates the schematic diagram for dye preparation.

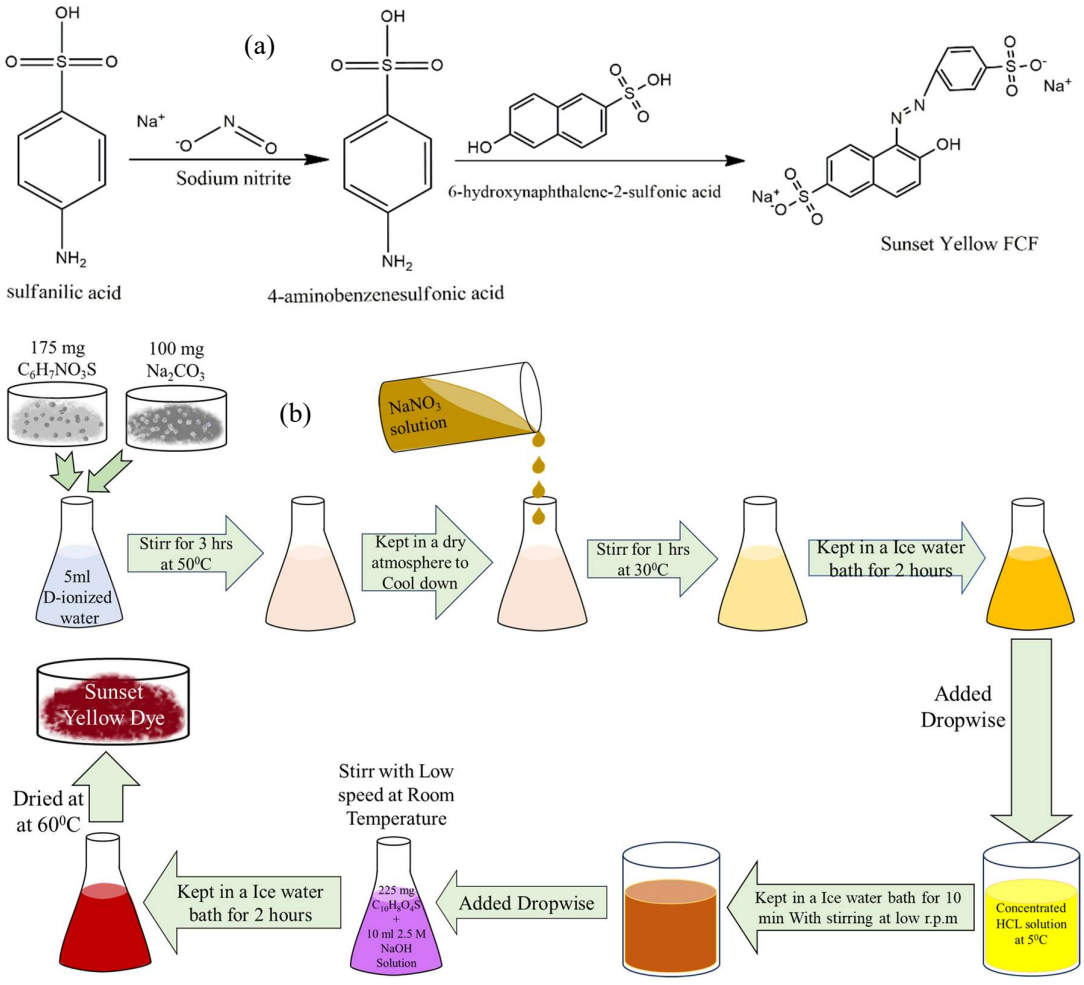

Figure 4.3: (a) Chemical reaction and (b) Schematic diagram of dye synthesis process

Subsequently, this diazonium salt reacts with 6-hydroxynaphthalene-2-sulfonic acid to yield Yellow 6, an intense orange-yellow azo dye. The synthesis commences by stirring 175mg of Sulfanilic acid and 100mg of sodium carbonate in 5mL of de-ionized water at 50°C for 3 hours

in a 50mL Erlenmeyer flask. After dissolution, the mixture is cooled to room temperature in a dry environment. Simultaneously, a solution containing 100mg of sodium nitrate and 1 mL of water is prepared in a test tube. This $NaNO_3$ solution is subsequently combined with the prior solution at room temperature and cooled in an ice water bath for 2 hours. We also observe the effect of ZnO nanoparticles on the device. The ZnO nanoparticles were obtained from Sigma-Aldrich (St Louis, MO, USA). The ZnO nanoparticles are 50 nm in size, with a surface area greater than 10.8 m^2/g.

4.2.3.c Synthesis of Dye-NPs nanocomposite

The preparation of the ZnO-organic dye composite begins with the formation of a ZnO suspension. A schematic flowchart illustrating the sample preparation process is shown in **Figure 4.4**. First, 10 mg of ZnO nanoparticles (99%) (Sigma-Aldrich, St. Louis, MO, USA) is dispersed in 50 ml of deionised (DI) water (obtained from the departmental Milli-Q water plant). After stirring for 30 minutes, 1 ml of acetic acid solution is added, followed by an additional 30 minutes of stirring to ensure uniform dispersion and surface modification.

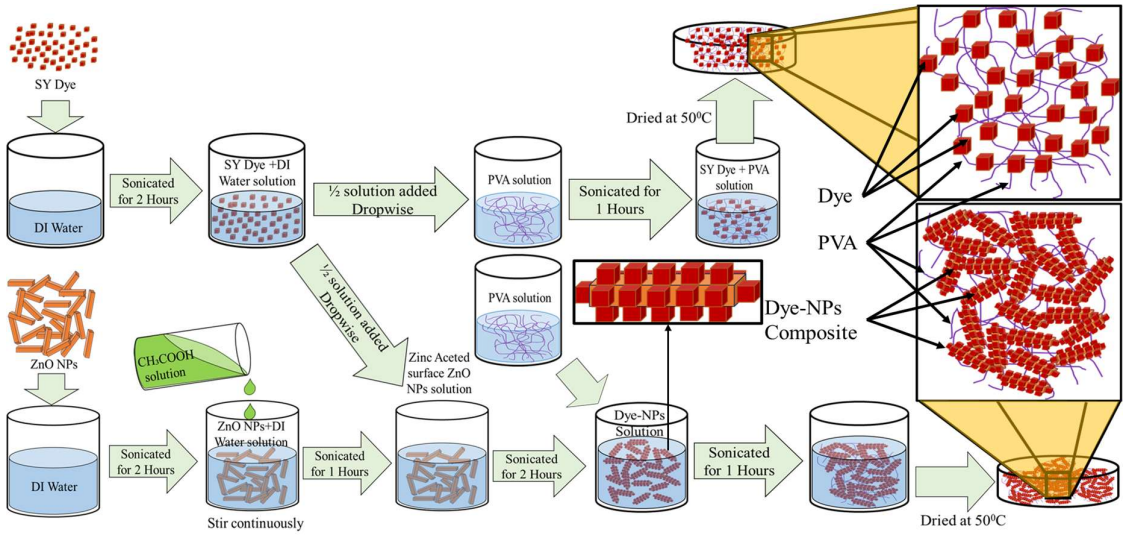

Figure 4.4: Schematic flowchart for the sample synthesis process.

This process functionalizes the ZnO nanoparticles by forming zinc acetate on their surface, enhancing their interaction with the organic dye. Separately, 10 mg of SY dye is dissolved in 50 ml of DI water and stirred for 30 minutes. Once both solutions are prepared, the dye solution is gradually added dropwise to the ZnO-acetic acid suspension while stirring continuously for several hours to facilitate thorough mixing and interaction. After complete mixing, the

composite solution is allowed to age to ensure full integration of ZnO nanoparticles with dye molecules. Finally, the solution is dried and ground into a fine powder.

4.2.3.d Preparation of ITO/Dye-ZnO/Cu Schottky Cell

In two separate clean beakers, 2 mg of SY dye and a mixture of SY dye with nanoparticles are each blended with 2 ml of polyvinyl alcohol (PVA) solution using ultrasonic sonication. The prepared samples are then independently spin-coated onto pre-cleaned ITO glass slides at 2000 rpm. Once partially dried, a cleaned Cu plate is positioned as the back electrode, and the assembled structure is heated on a controlled hotplate at 60°C for 1 hour.

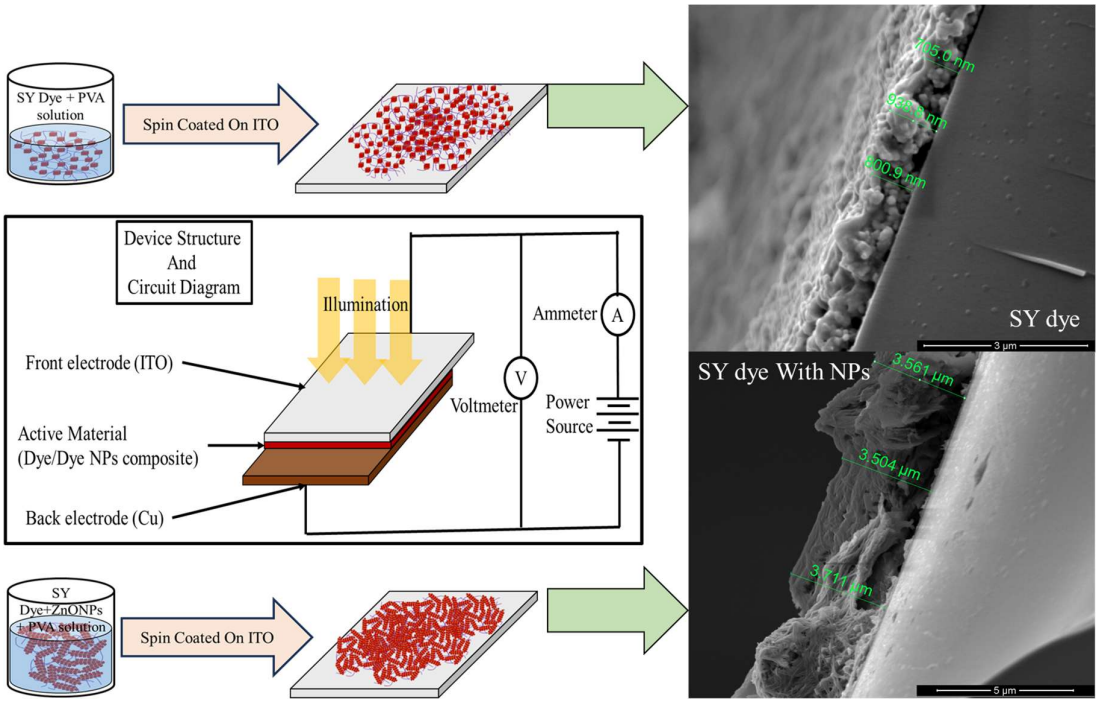

Figure 4.5: Flow chart for the device synthesis process. (Inset) SEM image for the thickness of the prepared devices.

A schematic diagram depicting the cell configuration is shown in **Figure 4.5**. SEM image for the thickness of the film is depicted in the inset of **Figure 4.5** indicating the overall thickness of the films is 800 nm for dye only and 3.50 µm for dye with NPs.

4.2.4 Characterisation

This section focuses on the characterisation of the materials and devices used in the study. It details the techniques and methods employed to analyse their structural, optical, and electrical

properties, providing insights into their performance and suitability for the intended application.

4.2.4.a UV-Vis analysis

A comparison of optical spectroscopy between dye with and without nanoparticles is presented in **Figure 4.6**. It's observed that the peak intensity diminishes upon ZnO NPs incorporation. However, the peak's position remains consistent (468 nm), aligning with our prior findings, indicative of an optical bandgap calculated at 2.34 eV. This represents that there is no influence of the NPs on optical absorption for the device.

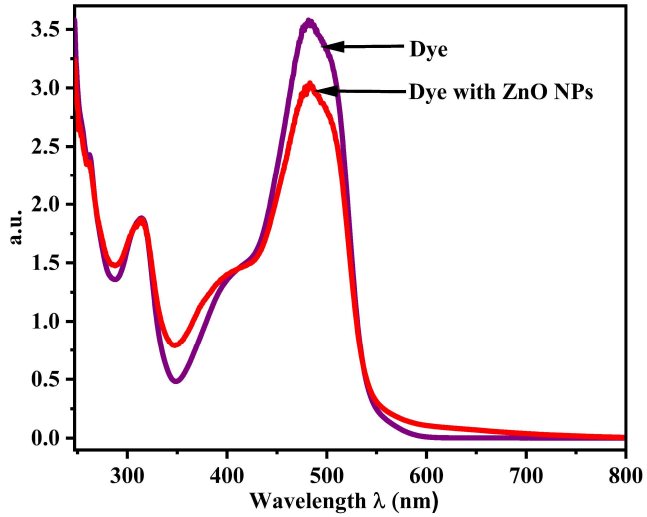

Figure 4.6: Absorption spectroscopy comparison of SY dye with and without NPs.

4.2.4.b X-Ray Diffraction Analysis

The diffraction pattern depicted in **Figure 4.7(a)** suggests the polycrystalline nature of the SY powder due to the presence of multiple diffraction peaks with varying intensities. Structural analysis was carried out on the powder sample by the measurement of Powder-X-ray-Diffraction (PXRD) using a Bruker D8 SWAX diffractometer with Cu-Kα radiation of wavelength 1.5404 Å which is operated at 35 kV and 35 mA at room temperature.

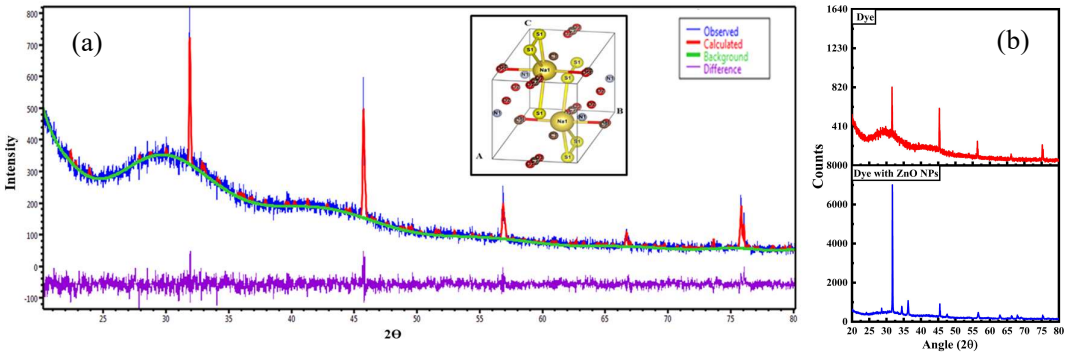

Figure 4.7: (a) XRD analysis of SY dye. (Inset) Possible crystal structure of the dye. (b) XRD comparison for dye without and with NPs.

Table 4.1: Crystallographic information of SY dye with and without TiO_2.

Parameter	SY dye
Lattice Type	p
Space Group Name	p 2/m
Space Group Number	10
a [å]	7.89500
b [å]	5.60565
c [å]	5.95340
α [°]	90.0000
β [°]	109.6890
γ [°]	90.0000

To get better diffraction peaks, the measurement was performed in the 2-theta range of 20–80° at a scan rate of 0.5/min. The rotation of the sample holder was set to 10 rpm to ensure all the possible peak information could be obtained. We used Expo2014 software to refine PXRD data. The plausible structure of the SY dye is depicted in the inset of **Figure 4.7(a)**. **Table 4.1** below represents the plausible crystallographic information of the prepared dye. **Figure 4.7(b)** illustrates the comparison of the XRD patterns for the dye, and the blend of dye with ZnO NPs.

The XRD pattern for ZnO NPs aligns with the JCPDS file using reference code 01-084-1285 [27]. The presence of diffraction peaks corresponding to both the dye and NPs in the composite's XRD pattern confirms the successful composition of the blend.

4.2.4.c FESEM Analysis

Figure 4.8(a) displays SEM images of SY dye in powdered form from various angles, revealing numerous crystallised cubic like nanoparticles (NPs) within the SY dye.

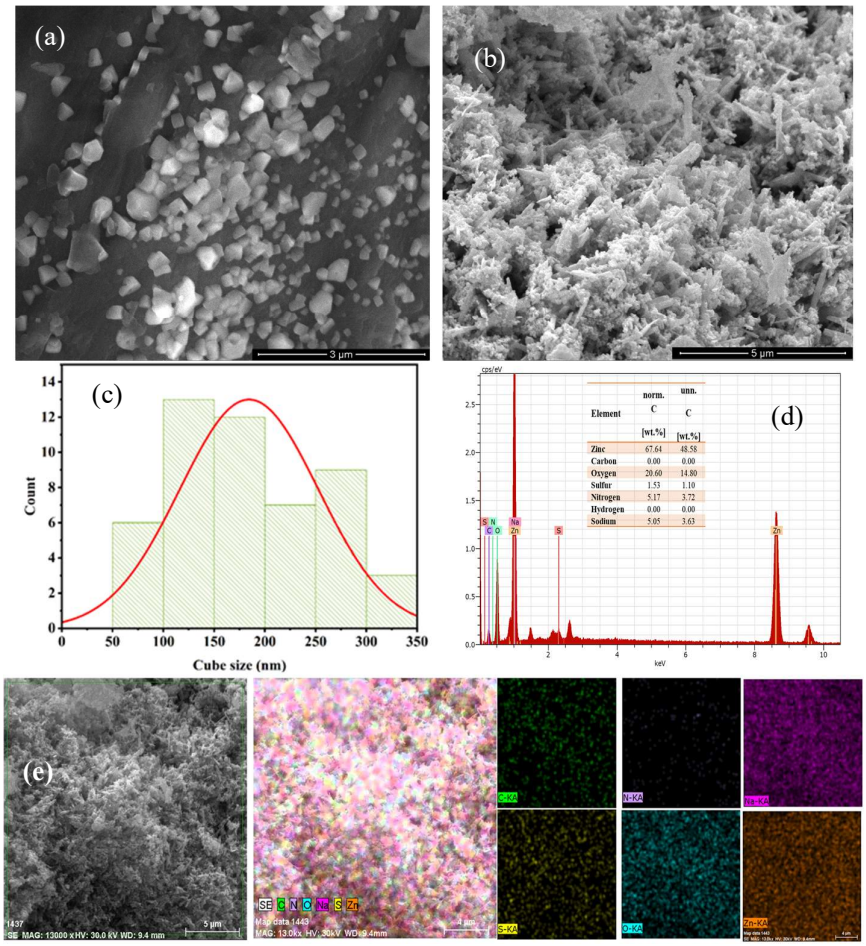

Figure 4.8: (a) SEM image of SY dye shows the cubic structure of dye NPs. (b) Particle size distribution plot of dye. (c) SEM image of Dye-NPs nanocomposite. (d) EDX spectra of Dye-NPs nanocomposite. (e) EDX mapping of dye-NPs nanocomposite.

The crystalline nature of the particles may facilitate electron conduction. **Figure 4.8(b)** depicts the particle size distribution, indicating an average size of approximately 175nm. The SEM

image of the composite structure is depicted in **Figure 4.8(c),** revealing the significant agglomeration of ZnO NPs with the SY dye, affecting NP characteristics and reducing their number in nanocomposites at constant filler concentration [28]. Agglomeration increases with higher ZnO NP concentrations, potentially enhancing charge injection and flow through the device. Notable voids and pores are visible on the surface. **Figure 4.8(d)** presents the EDX data confirming the presence of all elements in the SY dye. Weight percentages of each element are detailed in the table Inset of **Figure 4.8(d)**. **Figure 4.8(e)** EDX-Mapping of the dye-NPs represents the corresponding presence of all the elements in the composite.

4.3 Result and Discussion

This section presents the experimental results along with a detailed discussion and analysis of the findings. It highlights the significance of the observed outcomes and explores their broader implications in the context of the study.

4.3.1 Interfacial Property Analysis

To study the interfacial properties, we have examined the current-voltage-temperature (I-V-T) characteristics for both devices. **Figures 4.9(a)** and **4.9(b)** represent the I-V-T relation of dye without and with NPs, respectively. **Figure 4.9(c)** and **4.9(d)** represent the comparison of zero bias barrier height (Φ_{b0}) and ideality factor (η) for both devices, respectively. We can see that the variation of Φ_{b0} is nonlinear, resulting in a nonhomogeneous distribution of barrier height. The comparison of the Richardson constant for the dye with and without NPs is depicted in **Figure 4.9(e)**. It is observable that the Richardson constant of the device has been modified by the incorporation of NPs. According to our previously published article, the equation for the thermionic emission in the MS junction can be written by the following (**Equation (4.1)**) (symbols have their usual meanings) after considering the inhomogeneity parameters.

$$\ln(A^*_{eff}) = \ln A^* + \left(\frac{q}{kT} - \frac{kT}{q\beta^2\zeta^2}\right)(\phi_{b0} - \phi_b) \tag{4.1}$$

To evaluate β and ζ to evaluate the homogeneous Richardson constant, we have measured the capacitance-voltage-frequency (C-V-F) dependency of both devices (**Figure 4.10(a)** and **4.10(b)**). **Table 4.2** below represents the other calculated parameters. It illustrates a noticeable trend wherein the reverse bias voltage (V_{bi}) increases with the applied frequency of the devices, while a decrease in V_{bi} is observed in the presence of ZnO nanoparticles across all frequency ranges. This

decline can be attributed to the reduction in the width of the depletion layer at the interface, facilitating greater electron passage over the barrier upon nanoparticle integration, as evident in the comparison of depletion layer widths (W_L) in Table 1.

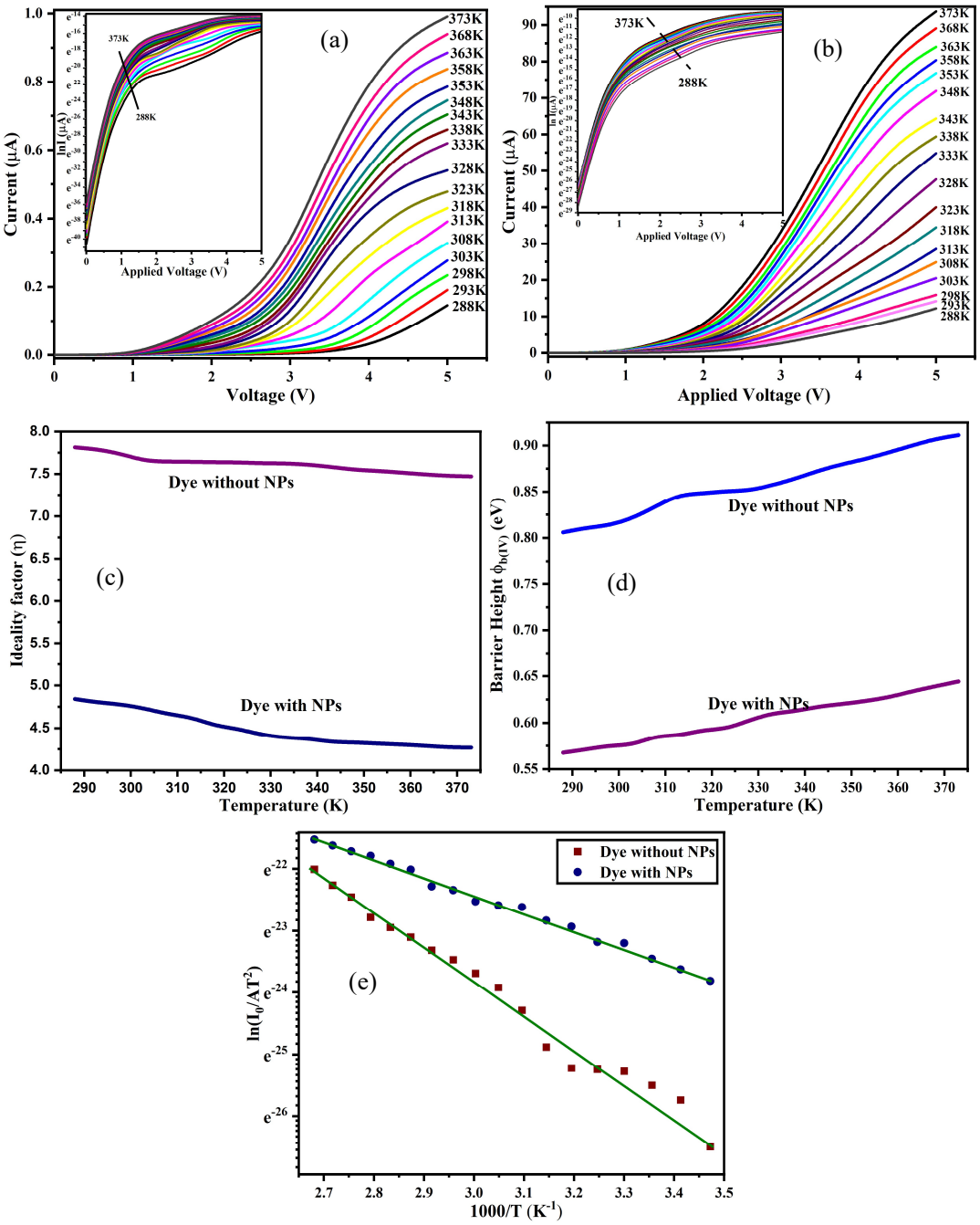

Figure 4.9: Temperature-dependent I-V characteristics of (a) dye and (b) dye with NPs. (Inset) lnI-V-T plot of (a) dye and (b) dye with NPs. Dependency of (c) Φ_{b0} and (d) η with temperature. (e) Comparison of the Richardson plot.

Additionally, there is a discernible rise in the maximum electric field with frequency and after nanoparticle integration, leading to increased charge accumulation at the interface and subsequently reducing the depletion layer with frequency and nanoparticle integration. Utilising Equation (4.1), the homogeneous Richardson constant was calculated, yielding values of 30.55 x 10^{-3} $Am^{-2}K^{-2}$ and 26.43 x 10^{-2} $Am^{-2}K^{-2}$ for dye without and with nanoparticles, respectively.

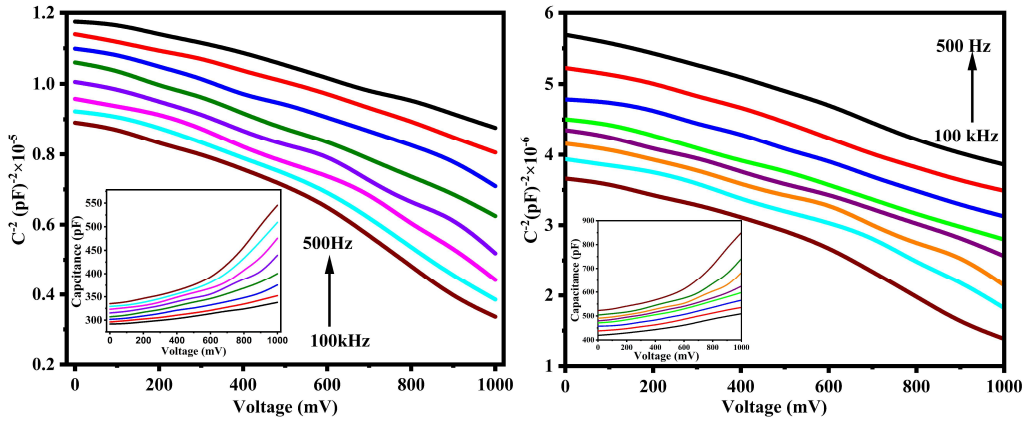

Figure 4.10: $C^{-2} - V$ plot of (a) SY dye and (b) SY dye with NPs for different frequencies. (Inset) C-V-F plot of (f) SY dye and (g) SY dye with NPs.

Table 4.2: Extracted junction parameters of SY dye with and without NPs.

Frequency (KHz)	Dye Without NPs						Dye With NPs					
	ε_S	V_{bi} (eV)	N_d × 10^{27} (m^{-3})	E_m × 10^2 (Vm^{-1})	W_L (cm)	$\phi_{b(CV)}$ × 10^{-1} (eV)	ε_S	V_{bi} (eV)	N_d × 10^{27} (m^{-3})	E_m × 10^3 (Vm^{-1})	W_L × 10^{-3} (cm)	$\phi_{b(CV)}$ × 10^{-1} (eV)
0.5	9.298	0.386	1.068	7.201	0.018	1.655	4.263	0.3	1.970	19.338	5.521	1.418
1	9.442	0.345	0.983	7.762	0.017	1.983	4.252	0.286	2.034	19.795	5.314	1.724
3	9.615	0.295	0.865	8.692	0.016	2.201	4.305	0.276	2.115	22.139	5.009	1.939
5	9.789	0.248	0.742	9.702	0.015	2.485	4.359	0.257	2.082	23.582	4.725	2.138
10	10.052	0.220	0.668	11.046	0.014	2.592	4.501	0.246	2.023	25.752	4.413	2.319
30	10.299	0.198	0.608	13.136	0.013	2.953	4.598	0.218	1.798	28.945	4.044	2.703
50	10.494	0.178	0.542	15.378	0.012	3.454	4.649	0.196	1.635	36.946	3.736	2.830
100	10.682	0.165	0.507	17.199	0.011	3.867	4.762	0.3	18.408	39.984	3.534	2.858

4.3.2 DC Conductivity Analysis

The variation of DC conductivity concerning temperature is depicted in **Figures 4.11(a)** and **4.11(b)**, along with the corresponding Arrhenius plots shown in the insets of both figures, respectively. In both scenarios, conductivity rises with increasing temperature, notably enhanced when ZnO NPs are introduced. This enhancement suggests increased transfer of π-electrons across the barrier due to ZnO NPs incorporation [29]. Analysis of the DC conduction mechanism in both devices is conducted using the Arrhenius exponential law equation (**Equation (4.2)**) [30,31], where symbols retain their conventional meanings.

$$\sigma = \sigma_{01} e^{-\Delta E_1 / k_B T} + \sigma_{02} e^{-\Delta E_2 / k_B T} \tag{4.2}$$

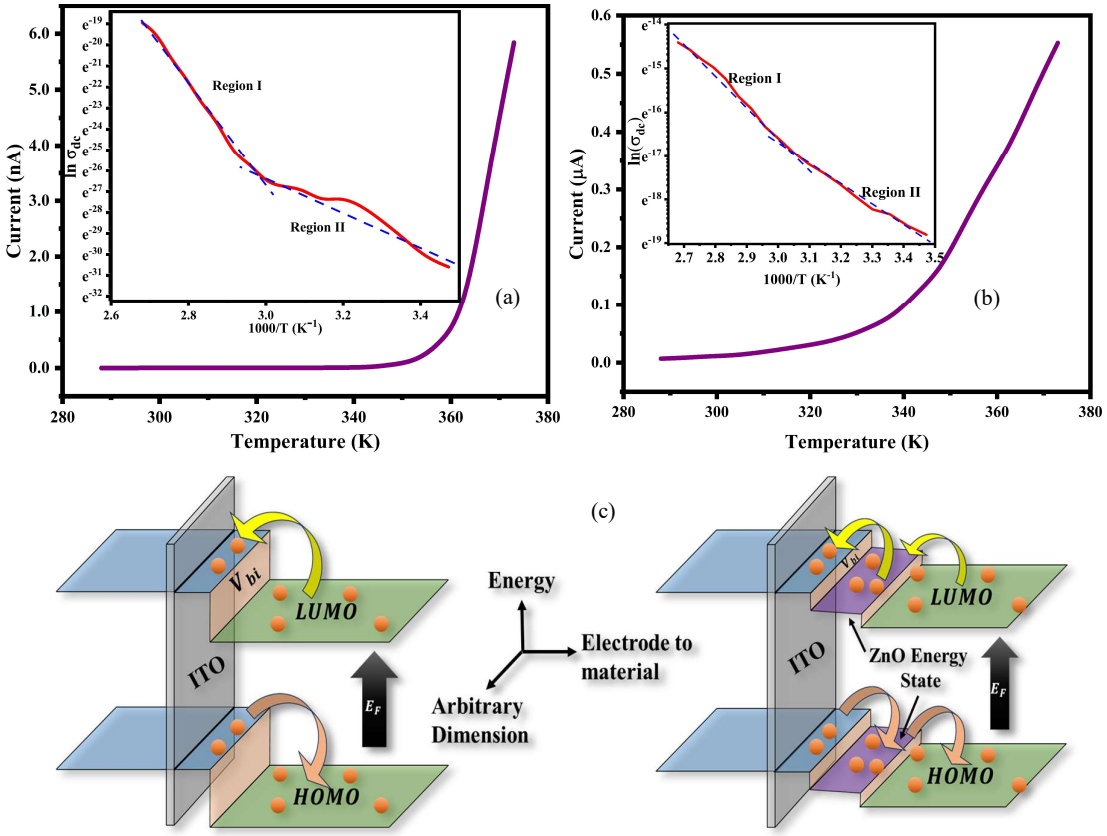

Figure 4.11: (a) Dependency of DC conductivity with temperature for SY dye without NPs. (Inset) Arrhenius plot of SY dye without ZnO NPs. (b) Dependency of DC conductivity for SY dye with NPs. (Inset) Arrhenius plot of SY dye with ZnO NPs. (c) Representation of energy band diagram of the Sy dye-based cells and the position of mobility stated introduced by ZnO NPs.

The activation energy plots depicted in the inset of **Figure 4.10(a)** and **4.10(b)** reveal distinct conduction mechanisms in both scenarios. However, a slight decrease in the transition between region I and region II is observed for the dye with NPs. Incorporation of ZnO NPs results in a modification of both low-temperature activation energy (from 0.683 eV to 0.528 eV) and high-temperature activation energy (from 0.466 eV to 0.340 eV). The presence of surface states and defects in ZnO nanoparticles serves as trapping sites for carriers, altering the electronic structure and surface reactivity, thus reducing the activation energy. Furthermore, a modification in the low and high-temperature conductivity limits is observed from $6.18 \times 10^{-8}\ (\Omega - m)^{-1}$ to $7.70 \times 10^{-7}\ (\Omega - m)^{-1}$, and from $1.01 \times 10^{-8}\ (\Omega - m)^{-1}$ to $8.34 \times 10^{-7}\ (\Omega - m)^{-1}$ respectively in the presence of NPs. It is visible that by the application of ZnO NPs, the hopping length becomes smaller. As a possible explanation, we can say that ZnO NPs, with their high electron mobility, enhance overall charge carrier mobility in composite materials and form a percolation network, which facilitates direct charge transport, minimising the distance charge carriers need to hop. These nanoparticles provide continuous and efficient pathways, enabling faster and more direct movement of charge carriers (**Figure 4.11(c)**).

4.3.3 AC Conductivity Analysis

The dependency of ΔE(ω) with the frequency for dye without and with NPs is shown in **Figures 4.12(a)** and **12(b),** respectively, with and without NPs. The temperature-dependent $\sigma_{AC}(\omega)$of SY dye with and without ZnO NPs are shown in the inset of **Figures 4.12(a)** and **4.12(d)**, respectively. Equation (4.3) can be utilised to represent the $\sigma_{AC}(\omega)$ of the respective devices [32]. Symbols have their usual notations [33]. The activation energy (ΔE(ω)) for different frequency ranges is calculated using the following Arrhenius equation [34–36] (**Equation (4.4)**) (Symbols have their usual meanings).

$$\sigma_{TotalAC}(\omega) = \sigma_{AC}(\omega) + \sigma_{DC}(\omega \to 0) \tag{4.3}$$

$$\sigma_{AC}(\omega) = \sigma_0 e^{\frac{-\Delta E(\omega)}{k_B T}} \tag{4.4}$$

It's evident that ΔE(ω) declines with rising frequency. Both cells exhibit less reliance of $\sigma_{AC}(\omega)$ on frequency at lower temperature ranges, yet display increased dependency at higher temperatures. Particularly, the AC conductivity notably rises upon NP incorporation,

accompanied by heightened frequency-dependent $\sigma_{AC}(\omega)$ at elevated temperatures compared to dye without NPs. A significant finding is the diminishing variation of activation energy in dye-NP blends with increasing frequency, contributing to lowered activation energy values. This phenomenon suggests enhanced electrical conductivity due to increased charge carrier localisation, influenced by space charge contribution, crucial for charge transfer [37,38]. The following equation (**Equation (4.5)**) is used to explain the AC conductivity of both cells [32,39]. The relation between the barrier, s-parameter and the polaron hopping length can be explained with the following **Equations (4.6)** and **(4.7)**.

$$\sigma_{AC}(\omega) = A\omega^{s} \tag{4.5}$$

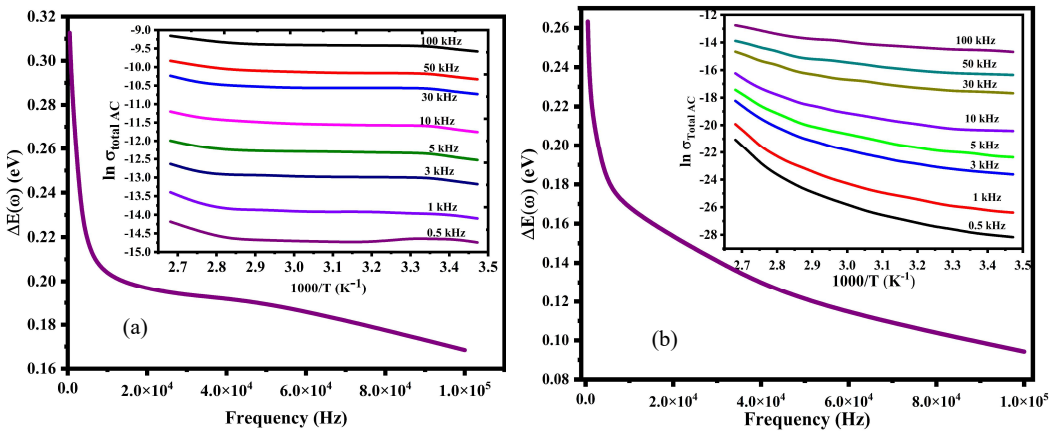

Figure 4.12: (a) Dependency of frequency-dependent ΔE(ω) for SY dye without NPs. (Inset) Temperature-dependent AC conductivity of SY dye without NPs. (b) Dependency of ΔE(ω) for SY dye with NPs. (Inset) Temperature-dependent AC conductivity of SY dye with NPs

$$W = W_m - \frac{ne^2}{\pi\varepsilon_1(\omega)\varepsilon_0 R} \tag{4.6}$$

$$1 - s = \frac{6k_B T}{W_m} \tag{4.7}$$

The parameter s determines the specific model applicable for elucidating the conduction mechanism. The observed dependency of the s-parameter for both devices aligns with that of the Correlated-Barrier-Hopping (CBH) model, among various other models [40–43].

4.3.4 Charge Transport Property Analysis

Furthermore, for a detailed analysis of the charge transport mechanism, we have considered the log-log plot of the I-V-T relation of both the cells (**Figure 4.13(a)** and **4.13(b)**). Both figures exhibit two distinct regions: region I, characterised by a slope (m) around 1, and region II, featuring a slope greater than or equal to 2 ($m \geq 2$). A slope of 2 or higher indicates the presence of a space-charge-limited current (SCLC) mechanism, while a slope of less than or equal to 1 ($m < 1$) suggests an ohmic characteristic. Typically, organic materials are susceptible to trapping, wherein localised energy states within their energy bandgap result from defects and impurities. These traps serve as recombination centres for charge carriers, influencing the overall device performance.

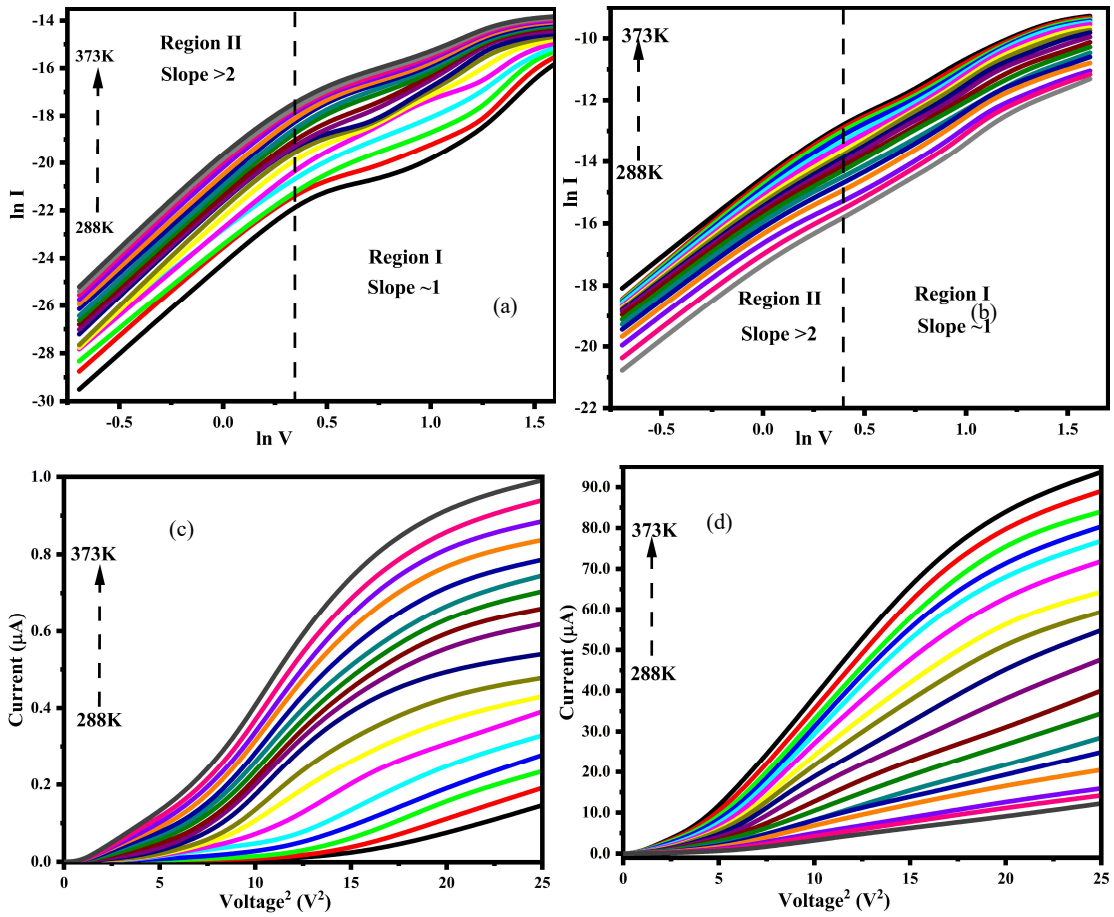

Figure 4.13: lnI-lnV plot for (a) Dye without NPs and (b) Dye with NPs. I-V^2 plot for (c) Dye without NPs and (d) Dye with NPs.

Using the Mott-Gurney relation (**Equation (4.8)**) in the SCLC region, we can calculate the charge transport parameters of both cells, which are depicted in **Table 4** below [44]. Equations 4.9-4.11 can also be used to calculate the diffusion length ι_d, transit time (τ), and diffusion coefficient (D) from the Einstein-Smoluchowski equation (**Equation (4.11)**) [45]. **Figures 4.13(c)** and **4.13(d)** represent the I-V^2 plot of the cells.

Table 4.3: Calculated SCLC parameters

Temperature	**Dye Without NPs**				**Dye With NPs**			
(K)	$\mu_{eff} \times 10^{-4}$ ($m^2V^{-1}s^{-1}$)	$\tau \times 10^{-3}$ (s)	$D \times 10^{-6}$ (m^2s^{-1})	ι_d (µm)	$\mu_{eff} \times 10^{-4}$ ($m^2V^{-1}s^{-1}$)	$\tau \times 10^{-4}$ (s)	$D \times 10^{-4}$ (m^2s^{-1})	ι_d (µm)
288	2.80356	5.21	6.96405	2.69402	1.66799	9.13244	0.53661	8.69166
293	3.45216	4.2	8.72403	2.70702	1.99081	9.63932	0.63188	8.78
298	3.47757	3.55	10.3579	2.71322	2.24117	10.2221	0.70168	8.86508
303	3.63109	3.25	11.3284	2.71512	2.93187	10.7359	0.90529	8.94412
308	3.77976	2.84	12.985	2.71485	3.4784	11.2497	1.05904	9.02613
313	3.92945	2.52	14.6657	2.71823	3.9315	12.1665	1.18004	9.10965
318	4.00536	2.62	14.1019	2.7204	4.7947	13.6215	1.41845	9.18715
323	4.02993	2.59	14.3931	2.73159	5.59197	14.9506	1.6302	9.26776
328	4.20593	2.54	14.7616	2.74007	6.75668	16.7573	1.9406	9.36417
333	4.33477	2.71	14.078	2.76236	7.90714	19.6433	2.23693	9.44313
338	4.42501	2.83	13.6368	2.78017	8.8155	23.7847	2.45589	9.52378
343	4.67775	2.99	13.0908	2.79689	9.65758	27.8119	2.64883	9.60647
348	4.888	3.13	12.6241	2.81285	10.8007	34.0466	2.91578	9.6945
353	4.9016	3.28	12.1948	2.82857	11.6539	38.239	3.09586	9.73308
358	5.14153	3.33	12.1331	2.84285	12.1885	45.2773	3.18532	9.79208
363	5.16647	3.46	11.834	2.8599	12.787	59.5972	3.28657	9.89064
368	5.21795	3.59	11.5251	2.87552	13.528	67.3112	3.41869	9.97477
373	5.43251	3.73	11.1878	2.88877	14.2358	80.9877	3.53618	10.08281

$$J = \frac{9\mu_{eff}\varepsilon_0\varepsilon_r}{8}\left(\frac{V^2}{d^3}\right) \quad (4.8)$$

$$\tau = \frac{9A\varepsilon_0\varepsilon_r}{8d}\left(\frac{V}{I}\right) \quad (4.9)$$

$$\mu_{eff} = \frac{qD}{kT} \quad (4.10)$$

$$\iota_d = \sqrt{2D\tau} \quad (4.11)$$

Where μ_{eff} is effective mobility, $\varepsilon_0$and ε_r are the permittivity of free space and the relative dielectric constant of the material, and J is the current density. We can see that the ι_d, τ and D have been improved by the incorporation of NPs. We can conclude a reduction in the trap sites by the incorporation of NPs, causing the improvement of the above charge conduction parameters, resulting in an overall increase in the charge conduction of the cell.

4.4 Photoelectric Study

Figure 4.14(a) represents the room temperature current-voltage characteristics of the cells without and with NPs, respectively, in illuminated conditions (illumination intensity P_{in}=100 W/cm^2).

The increase in the photocurrent in the presence of NPs is a notable observation. Reduction in the trap states, as discussed earlier, can be a good explanation for that outcome. The kinetics of the photocurrent rise and fall for the cell are given in **Figure 4.14(b)**. We can see that the peak current is stable for every cycle of the illuminated condition, along with the rising and declining time of the current being also low. Also, the stability (**Figure 4.14(c)** and **4.14(d)**) of the current is sustained for a longer time for the cell containing NPs. As we discussed earlier, the presence of ZnO NPs exhibits high electron mobility, enabling efficient charge separation and transport, thereby reducing charge carrier recombination and leading to a more stable and sustained photocurrent. Additionally, ZnO NPs passivate trap states and defects within the organic dye matrix, minimising recombination events at these sites and further stabilising the photocurrent. Also, they improve the interface barrier properties between the dye and the electrode, facilitating effective charge transfer and reducing interfacial losses, thereby maintaining a steady photocurrent.

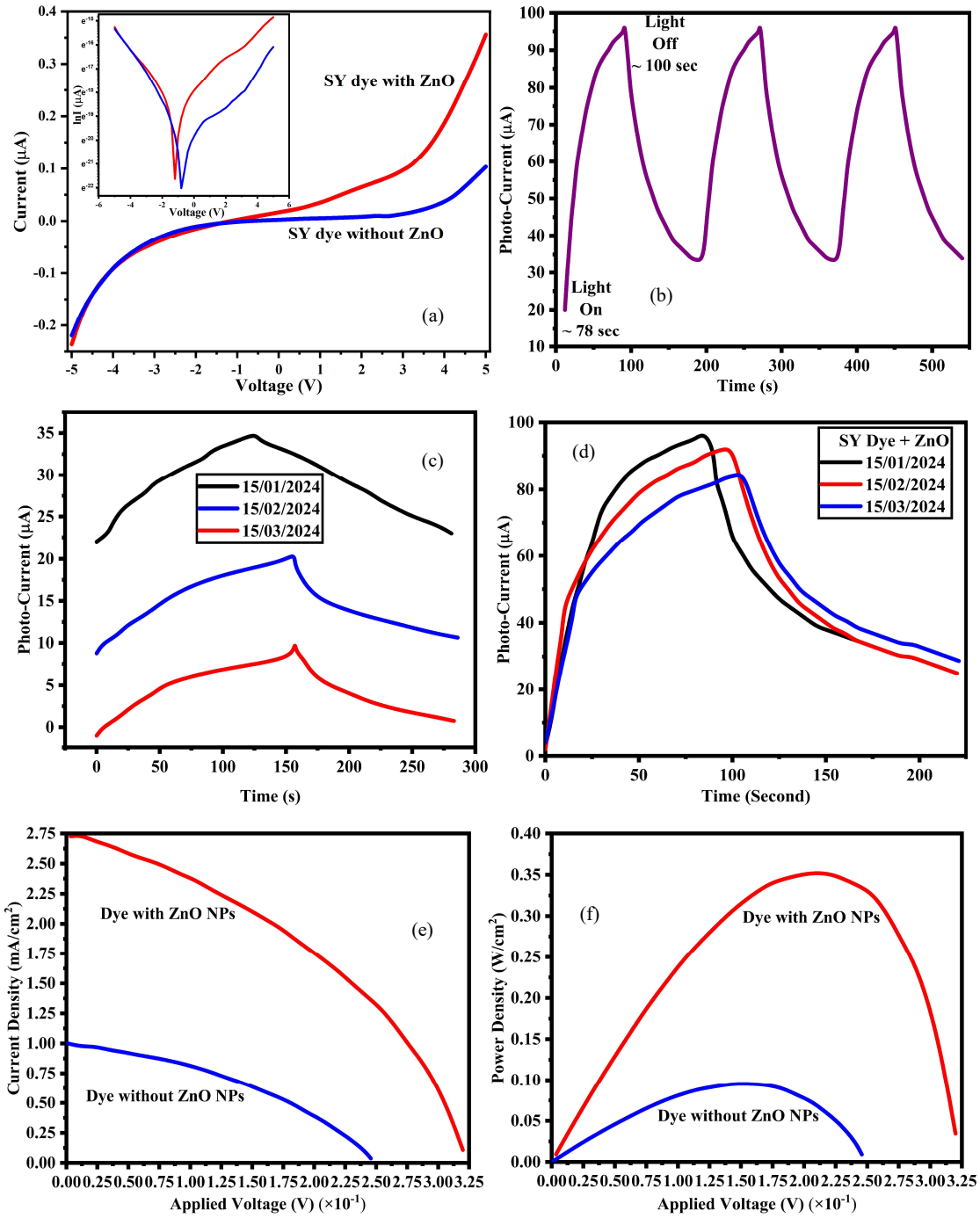

Figure 4.14: (a) Current-Voltage characteristics of dye with and without ZnO NPs in illuminated condition. (b) Photo response plot of Dye with NPs. Photo-Current Stability of (c) Dye and (d) Dye with ZnO NPs. (e) Current density vs Voltage plot. (f) Variation of power density with the applied voltage.

The comparison of the current density–voltage (J-V) characteristics of the prepared solar cells under illumination is presented in **Figure 4.14(e)**. The plot demonstrates the photovoltaic

behaviour of the fabricated cells, evidenced by the presence of short-circuit current density (J_{sc}) at zero bias voltage and open-circuit voltage (V_{oc}) at zero current density. **Figure 4.14(f)** illustrates the power density (P = JV) versus voltage plot, from which the maximum power (P_m), corresponding to maximum current density (J_m) and maximum voltage (V_m), is determined and listed in **Table 4.4**. Using these values, the Fill Factor (F_F) and efficiency (κ) of the cell were calculated and are also provided in **Table 4.4**. The responsivity (s) of the cell, which measures the effectiveness of light-to-electricity conversion, were calculated using **Equation (4.14)**, validating the cell's potential for further optoelectronic applications.

$$F_F = \frac{J_m V_m}{J_{sc} V_{oc}} \tag{4.12}$$

$$\kappa = \frac{J_{sc} V_{oc}}{P_{in}} F_F \times 100\% \tag{4.13}$$

$$S = \frac{J_{sc}}{P_{in}} \tag{4.14}$$

The responsivity of the cell was found to increase with the incorporation of ZnO NPs, which indicates a modification in the monomolecular recombination mechanism in the cell containing NPs.

Table 4.4: Calculated photoelectric parameters

Cell Configuration	V_{oc} (V)	J_{sc} (mAm^{-2})	V_m (V)	J_m (mAm^{-2})	F_F	κ	S (AW^{-1})
Dye Without NPs	0.319	1.003	0.149	0.641	0.298	0.095	0.010
Dye With NPs	0.245	2.726	0.209	1.684	0.526	0.351	0.027

4.5 Conclusion

This study compares the conduction mechanisms and photo response of Sunset Yellow (SY) dye with and without ZnO nanoparticles (NPs). The addition of ZnO NPs increases the device's DC electrical conductivity. The activation energies at low and high temperatures decrease from 0.683 eV to 0.532 eV and from 0.466 eV to 0.351 eV, respectively, due to the introduction of impurity energy states by the NPs. ZnO NPs introduce surface states and defect levels that act as electron traps, reducing the energy barrier and enhancing charge mobility. AC conductivity analysis indicates that the CBH model is the dominant charge transport mechanism, with the incorporation of NPs significantly reducing the hopping length and improving charge transport. Devices with and without ZnO NPs were prepared using a spin-coating technique, and their I-V-T characteristics were studied over a temperature range of 288K to 333K. The incorporation of NPs modifies the Richardson constant and barrier height, improving charge injection and conduction current due to reduced barrier inhomogeneity. The J-V characteristics of SY dye cells with ZnO NPs were examined under various illumination intensities, revealing a monomolecular recombination mechanism in these sensitised solar cells. This research provides valuable insights into the effects of nanoparticle incorporation on the performance of organic dye-based devices.

4.6 Reference

[1] H. Naarmann, The development of electrically Conducting Polymers, Advanced Materials 2 (1990) 345–348. https://doi.org/10.1002/adma.19900020802.

[2] G.F. Salem, E.A.A. El-Shazly, A.A.M. Farag, I.S. Yahia, Optical and microelectronic analysis of rhodamine B-based organic Schottky diode: a new trend application, Appl Phys A Mater Sci Process 124 (2018) 1–12. https://doi.org/10.1007/s00339-018-2151-y.

[3] D. Mulati, N. Timonah, W. Bjorn, The absorption spectra of natural dyes and their suitability as a sensitiser in organic solar cell application, Jagst 14 (2012).

[4] K.U. Isah, U. Ahmadu, A. Idris, M.I. Kimpa, U.E. Uno, M.M. Ndamitso, N. Alu, Betalain pigments as natural photosensitizers for dye-sensitised solar cells: The effect of dye pH on the photoelectric parameters, Mater Renew Sustain Energy 4 (2015) 5–9. https://doi.org/10.1007/s40243-014-0039-0.

[5] A.R. Hernández-Martínez, M. Estévez, S. Vargas, R. Rodríguez, Stabilized conversion efficiency and Dye-Sensitized solar cells from Beta vulgaris pigment, Int J Mol Sci 14 (2013) 4081–4093. https://doi.org/10.3390/ijms14024081.

[6] D. Chen, Z.M. Wu, H. Zhang, Study on extraction and purification process of capsicum red pigment, Proceedings of the Fibre Society 2009 Spring Conference 1 (2009) 1450–1452. https://doi.org/10.5539/jas.v1n2p94.

[7] Khalil Ebrahim Jasim, Seamas Cassidy, Feryad Zaki Henari, Akil Aziz Dakhel, Curcumin Dye-Sensitised Solar Cell, Journal of Energy and Power Engineering 11 (2017). https://doi.org/10.17265/1934-8975/2017.06.006.

[8] A.S. Polo, N.Y. Murakami Iha, Blue sensitisers for solar cells: Natural dyes from Calafate and Jaboticaba, Solar Energy Materials and Solar Cells 90 (2006) 1936–1944. https://doi.org/10.1016/j.solmat.2006.02.006.

[9] M. Irimia-Vladu, E.D. Gåowacki, P.A. Troshin, G. Schwabegger, L. Leonat, D.K. Susarova, O. Krystal, M. Ullah, Y. Kanbur, M.A. Bodea, V.F. Razumov, H. Sitter, S. Bauer, N.S. Sariciftci, Indigo - A natural pigment for high-performance ambipolar organic field effect transistors and circuits, Advanced Materials 24 (2012) 375–380. https://doi.org/10.1002/adma.201102619.

[10] E.D. Glowacki, L. Leonat, G. Voss, M. Bodea, Z. Bozkurt, M. Irimia-Vladu, S. Bauer, N.S. Sariciftci, Natural and nature-inspired semiconductors for organic electronics, Organic Semiconductors in Sensors and Bioelectronics IV 8118 (2011) 81180M. https://doi.org/10.1117/12.892467.

[11] M. Irimia-Vladu, P.A. Troshin, M. Reisinger, G. Schwabegger, M. Ullah, R. Schwoediauer, A. Mumyatov, M. Bodea, J.W. Fergus, V.F. Razumov, H. Sitter, S.

Bauer, N.S. Sariciftci, Environmentally sustainable organic field effect transistors, Org Electron 11 (2010) 1974–1990. https://doi.org/10.1016/j.orgel.2010.09.007.

[12] C.J. Bettinger, Z. Bao, Organic thin-film transistors fabricated on resorbable biomaterial substrates, Advanced Materials 22 (2010) 651–655. https://doi.org/10.1002/adma.200902322.

[13] M. Irimia-Vladu, P.A. Troshin, M. Reisinger, L. Shmygleva, Y. Kanbur, G. Schwabegger, M. Bodea, R. Schwödiauer, A. Mumyatov, J.W. Fergus, V.F. Razumov, H. Sitter, N.S. Sariciftci, S. Bauer, Biocompatible and biodegradable materials for organic field-effect transistors, Adv Funct Mater 20 (2010) 4069–4076. https://doi.org/10.1002/adfm.201001031.

[14] W.R. Klaus Hunger, Peter Mischke, Azo Dyes, 1. General, Ullmann's Encyclopedia of Industrial Chemistry (2012). https://doi.org/10.1002/14356007.a03.

[15] K. Suhailath, P. Jayakrishnan, B. Naufal, P. Periyat, V.C. Jasna, M.T. Ramesan, Synthesis by In Situ-Free Radical Polymerisation, Characterisation, and Properties of Poly (n-butyl methacrylate)/Samarium-Doped Titanium Dioxide Nanoparticles Composites, Advances in Polymer Technology 37 (2018) 1114–1123. https://doi.org/10.1002/adv.21770.

[16] K. Suhailath, M.T. Ramesan, Effect of neodymium-doped titanium dioxide nanoparticles on the structural, mechanical, and electrical properties of poly(butyl methacrylate) nanocomposites, Journal of Vinyl and Additive Technology 25 (2019) 9–18. https://doi.org/10.1002/vnl.21673.

[17] K. Suhailath, M.T. Ramesan, Investigations on the structural, mechanical, thermal, and electrical properties of Ce-doped TiO 2 /poly(n-butyl methacrylate) nanocomposites, J Therm Anal Calorim 135 (2019) 2159–2169. https://doi.org/10.1007/s10973-018-7285-9.

[18] K. Suhailath, M.T. Ramesan, Effect of Nano-Ce-Doped TiO2 on AC Conductivity and DC Conductivity Modelling Studies of Poly (n-Butyl Methacrylate), J Electron Mater 47 (2018) 6484–6493. https://doi.org/10.1007/s11664-018-6556-3.

[19] M.T. Ramesan, T. Sampreeth, Synthesis, characterisation, material properties and sensor application study of polyaniline/niobium doped titanium dioxide nanocomposites, Journal of Materials Science: Materials in Electronics 28 (2017) 16181–16191. https://doi.org/10.1007/s10854-017-7519-9.

[20] A. Rózycka, K.A. Bogdanowicz, N. Górska, J. Rysz, M. Marzec, A. Iwan, R. Pich, A. Januszko, Influence of TiO2 nanoparticles on liquid crystalline, structural and electrochemical properties of (8z)-n- (4-((z)-(4-pentylphenylimino)methyl)benzylidene)- 4-pentylbenzenamine, Materials 12 (2019) 1–17. https://doi.org/10.3390/ma12071097.

[21] L.W. Zhang, H.B. Fu, Y.F. Zhu, Efficient TiO2 photocatalysts from surface hybridisation of TiO2 particles with graphite-like carbon, Adv Funct Mater 18 (2008) 2180–2189. https://doi.org/10.1002/adfm.200701478.

[22] A. Rózycka, A. Iwan, K.A. Bogdanowicz, M. Filapek, N. Górska, D. Pociecha, M. Malinowski, P. Fryn, A. Hreniak, J. Rysz, P. Dabczynski, M. Marzec, Synthesis and characterisation of two new TiO2-containing benzothiazole-based imine composites for organic device applications, Beilstein Journal of Nanotechnology 9 (2018) 721–739. https://doi.org/10.3762/bjnano.9.67.

[23] S.A. Aal, D. Awadh, The effect of anchoring group on the performances of metal-free phthalocyanine and metallophthalocyanine dye/titanium dioxide interface for dye-sensitised solar cells, Surfaces and Interfaces 32 (2022). https://doi.org/10.1016/j.surfin.2022.102089.

[24] A. Aboulouard, B. Gultekin, M. Can, M. Erol, A. Jouaiti, B. Elhadadi, C. Zafer, S. Demic, Dye sensitised solar cells based on titanium dioxide nanoparticles synthesised by flame spray pyrolysis and hydrothermal sol-gel methods: A comparative study on photovoltaic performances, Journal of Materials Research and Technology 9 (2020) 1569–1577. https://doi.org/10.1016/j.jmrt.2019.11.083.

[25] D. Ziental, B. Czarczynska-Goslinska, D.T. Mlynarczyk, A. Glowacka-Sobotta, B. Stanisz, T. Goslinski, L. Sobotta, Titanium dioxide nanoparticles: Prospects and applications in medicine, Nanomaterials 10 (2020). https://doi.org/10.3390/nano10020387.

[26] A.K. Karan, D. Sahoo, N.B. Manik, Enhanced electrical conductivity and charge conduction mechanisms in Nano-cubical Sunset Yellow dye incorporated with titanium dioxide nanoparticles, Physica B Condens Matter 674 (2024). https://doi.org/10.1016/j.physb.2023.415570.

[27] J.K. Burdett, T. Hughbanks, G.J. Miller, J. V. Smith, J.W. Richardson, Structural-Electronic Relationships in Inorganic Solids: Powder Neutron Diffraction Studies of the Rutile and Anatase Polymorphs of Titanium Dioxide at 15 and 295 K, J Am Chem Soc 109 (1987) 3639–3646. https://doi.org/10.1021/ja00246a021.

[28] M.A. Ashraf, W. Peng, Y. Zare, K.Y. Rhee, Effects of Size and Aggregation/Agglomeration of Nanoparticles on the Interfacial/Interphase Properties and Tensile Strength of Polymer Nanocomposites, Nanoscale Res Lett 13 (2018). https://doi.org/10.1186/s11671-018-2624-0.

[29] F. Yakuphanoglu, I. Erol, A novel organic semiconducting material: 2-(3-mesityl-3-methylcyclobutyl)- 2-keto-ethyl methacrylate (MCKEMA), Physica B Condens Matter 352 (2004) 378–382. https://doi.org/10.1016/j.physb.2004.08.018.

[30] E. Schmidbauer, P. Schmid-Beurmann, Electrical conductivity and thermopower of Fe-phosphate compounds with the lazulite-type structure, J Solid State Chem 177 (2004) 207–215. https://doi.org/10.1016/j.jssc.2003.07.006.

[31] S.L. K., S. Roy, K.U. Rao, Evaluation of Activation Energy (Ea) Profiles of Nanostructured Alumina Polycarbonate Composite Insulation Materials, International Journal of Materials, Mechanics and Manufacturing 2 (2014) 96--100. https://doi.org/10.7763/ijmmm.2014.v2.108.

[32] S.R. Elliott, A.c. conduction in amorphous chalcogenide and pnictide semiconductors, Adv Phys 36 (1987) 135–217. https://doi.org/10.1080/00018738700101971.

[33] A.K. Karan, S. Bhunia, N.B. Manik, Study on the Conductivity of a Sunset Yellow Dye - Based Natural Organic Device, J Electron Mater (2022). https://doi.org/10.1007/s11664-022-09954-4.

[34] S.M. Reda, Electric and dielectric properties of some luminescent solar collectors based on phthalocyanines and hematoporphyrin doped PMMA, Dyes and Pigments 75 (2007) 526–532. https://doi.org/10.1016/j.dyepig.2006.06.031.

[35] F. Yakuphanoglu, E. Evin, M. Okutan, The dielectrical and alternating current conductivity properties of 40Cu+20Co+40Y2O3 ceramic, Physica B Condens Matter 382 (2006) 285–289. https://doi.org/10.1016/j.physb.2006.03.001.

[36] S.R. Lukić, S.J. Skuban, F. Skuban, D.M. Petrović, A.S. Tver'yanovich, DC and AC conductivities of (As2S3)100-x(AsSe0.5Te0.5I)x chalcogenide glasses, Physica B Condens Matter 403 (2008) 2578–2583. https://doi.org/10.1016/j.physb.2008.01.038.

[37] P.A. FARTODE, S.S. YAWALE, S.P. YAWALE, Study of Transport and Electrical Properties of PEO : PVP : NaClO 2 Based Polymer Electrolyte, International Journal of Chemical and Physical Sciences 4 (2015) 60–64.

[38] R. Divya, M. Meena, C.K. Mahadevan, C.M. Padma, Formation and Properties of ZnO Nanoparticle Dispersed PVA Films, 3 (2014) 722–727.

[39] S. Bhattacharyya, S.K. Saha, M. Chakravorty, B.M. Mandal, D. Chakravorty, K. Goswami, Frequency-dependent conductivity of interpenetrating polymer network composites of polypyrrole-poly(vinyl acetate), J Polym Sci B Polym Phys 39 (2001) 1935–1941. https://doi.org/10.1002/polb.1168.

[40] A. Ghosh, Frequency-dependent conductivity in bismuth-vanadate glassy semiconductors, 1990.

[41] A. Ghosh, Transport properties of vanadium germanate glassy semiconductors, 1990.

[42] A. R. Long, Frequency-dependent loss in amorphous semiconductors, Adv Phys 31 (1982) 553–637.

[43] D. Schoemaker, C.T. Shirkey, G.E. Pike, ac Conductivity of Scandium Oxide and a New Hopping Model for Conductivity*, n.d.

[44] S. Mahato, D. Biswas, L.G. Gerling, C. Voz, J. Puigdollers, Analysis of temperature-dependent current-voltage and capacitance-voltage characteristics of an Au/V2O5/ n -Si Schottky diode, AIP Adv 7 (2017). https://doi.org/10.1063/1.4993553.

[45] A. Dey, A. Layek, A. Roychowdhury, M. Das, J. Datta, S. Middya, D. Das, P.P. Ray, Investigation of charge transport properties in less defective nanostructured ZnO based Schottky diode, RSC Adv 5 (2015) 36560–36567. https://doi.org/10.1039/c4ra16828c.

CHAPTER 5

Modification of Hopping Parameters for Carmoisine dye-based cell doped with Multi-wall Carbon Nanotubes

Table of Contents

5.1 Introduction

In previous chapters, we have discussed about the effect of the nanoparticles on the barrier distribution and activation energy. In this chapter, we will examine how the carbon nanotubes will affect the polaron hopping mechanism to enhance the conductivity. Here we used Carmoisine (CS) dye as the active material and Multi-Wall-Carbon-Nanotube (MWCNT) as the incorporating material. It has been described previously that organic dyes (ODs) exhibit electrical conductivity [1–9]. But in most cases, the conductivity and efficiency are very low. Research works are ongoing to enhance the conductivity of different (ODs) for the future application of sustainable electronic applications. Basically, the polaron hopping mechanism is indispensable for augmenting the conductivity of ODs-based cells, particularly in applications such as organic photovoltaics (OPVs) and organic light-emitting diodes (OLEDs). Polaron hopping, which entails the transit of charge carriers (electrons or holes) between localised states within a disordered matrix, is especially salient in organic materials where the inherently amorphous structure often impedes efficient charge transport [10–13]. This mechanism allows for more effective movement of charge carriers through these localised states, which is vital in organic dye-based cells, where charge carrier mobility is otherwise severely constrained by the disordered nature of the material. The improved transport is paramount for achieving higher electrical conductivity. Additionally, polaron hopping mitigates the recombination losses that typically limit the efficiency of such cells by facilitating swifter charge transport, thereby reducing the duration that charge carriers reside within the active layer and minimising the likelihood of recombination. This mechanism directly enhances the material's electrical conductivity, a particularly significant improvement in organic materials that naturally exhibit lower conductivity relative to their inorganic counterparts. Moreover, effective polaron hopping bolsters the long-term stability of organic dye-based cells by preventing the accumulation of space charge and diminishing the formation of charge traps, which can otherwise degrade device performance over time. This enhanced charge transport ensures better charge collection at the electrodes, thereby improving the overall efficiency of the device. In summation, the polaron hopping mechanism is critical for elevating the conductivity and efficiency of organic dye-based cells, playing a pivotal role in the performance and reliability of these devices by facilitating charge transport, curbing recombination losses, and augmenting electrical conductivity.

Several research articles suggest that incorporating different nanoparticles with organic dyes is an effective strategy to enhance the conductivity and efficiency of organic dye-based devices

[14–18]. MWCNTs, with their exceptional electrical conductivity and high aspect ratio, can be good materials in this context [19–23]. MWCNTs provide efficient charge transport pathways, reducing the material's resistance. A sandwich architecture was utilised, comprising Indium-Tin-Oxide (ITO) coated glass as the front electrode, and a copper plate as the rear electrode, with a 1:1 blend of dye and MWCNTs serving as the interlayer. Structural properties were validated via X-ray diffraction (XRD) analysis, while morphological characteristics were scrutinised through Field-emission Scanning Electron Microscopy (FESEM). DC conductivity measurements were conducted using an Agilent-4294A Impedance Spectrometer across a temperature span of 288K to 333K (15°C to 60°C). Additionally, AC conductivity was evaluated within the identical temperature range, spanning frequencies from 500 Hz to 100 kHz. Capacitance-voltage measurements were employed to investigate interfacial properties, and the photosensitivity of the cells was assessed to determine their photovoltaic response. KEITHELY 2400 source meter and an SMU-Solar simulator are used to measure the photoconductivity and photo response of the prepared sample.

5.2 Experiment

This section provides a detailed overview of the experimental techniques, covering the materials used, the instruments employed, and the procedures followed throughout the study.

5.2.1 Materials

Sulfanilic acid ($C_6h_7NO_3S$) (99.99% purity) (Sigma Aldrich). $NaNO_3$ (99%) (Sigma Aldrich). Sodium Carbonate (Na_2CO_3) (99%) (Sigma Aldrich). 2-Naphthol-6-sulfonic acid ($C_{10}H_8O_4S$) (>98%) (Merck (India)). Dimethylformamide (DMF) (>98%) (Merck (India)). Hydrochloric acid (HCl) (98%) (Sigma Aldrich). Multiwall Carbon-Nanotube (MWCNT) (99%) (Merck (India)). Polyvinyl alcohol (PVA) (>98%) (Merck (India)). All the chemicals were used without further purification. The deionised water used in the experiment was collected from the departmental Milli(Q) water plant.

5.2.2 Instruments

The instruments used for this section are the same as we have discussed in the previous Chapters 3 and 4. A detailed description of all the instruments can be found in Chapters 3 and 4.

5.2.3 Preparation of Cell

This section outlines the detailed procedures involved in cell preparation, including the materials, methods, and conditions used to assemble and fabricate the cell.

5.2.3.a Electrode Cleaning Process

To begin, two copper pieces and glass plates coated with Indium-Tin-Oxide (ITO) are cleaned by wiping them with a mild detergent. After soaking in the detergent solution at 60°C for ten minutes, they are rinsed with deionised water. The electrodes are then sonicated sequentially in deionised water, 2-propanol, and acetone for 10 minutes each. They are subsequently dried in a nitrogen environment. Before spin-coating, the samples are subjected to UV ozone treatment for ten minutes.

5.2.3.b Synthesis and Purification of CS dye

CS dye, also known as azorubine (CI Food Red 3, E122), is a synthetic azo dye commonly used as a food colouring agent. The synthesis of CS dye involves a classic azo-coupling reaction, which is a type of electrophilic aromatic substitution reaction where the diazotisation of sulfanilic acid is followed by an azo-coupling reaction with 1-naphthol. Sulfanilic acid is dissolved in water and treated with sodium hydroxide to form its sodium salt. The solution is cooled to 0–5°C and then reacted with sodium nitrite in an acidic medium (HCl) to generate a diazonium salt. This diazonium compound is subsequently coupled with 1-naphthol in a slightly alkaline medium, typically maintained at a pH of 8–10 using sodium carbonate. The reaction results in the formation of an azo bond, producing the vibrant red CS dye. The dye is precipitated, filtered, washed, and dried to obtain the final product. **Figure 5.1** represents the detailed schematic diagram of the synthesis process of the dye.

5.2.3.c Synthesis of Dye-MWCNT nanocomposite

The synthesis of CS dye-multiwall carbon nanotube (MWCNT) nanocomposite begins with functionalizing the MWCNTs with carboxyl groups to improve compatibility and interaction between the dye. First, MWCNTs are functionalized by oxidation using a mixture of concentrated nitric and sulfuric acids, introducing carboxyl (-COOH) groups onto their surface. This process enhances their dispersibility in aqueous and organic solvents while providing reactive sites for further interactions. Inset of **Figure 5.1** represents the fabrication of the composite and the cell in detail. The functionalized MWCNTs are then mixed with CS dye under optimised conditions, such as controlled pH, temperature, and stirring, to promote strong

interactions, including hydrogen bonding or π-π stacking, between the dye molecules and the carboxyl-functionalized MWCNTs. After synthesis, the nanocomposite is purified through filtration and washing to remove excess dye and other by-products, followed by drying.

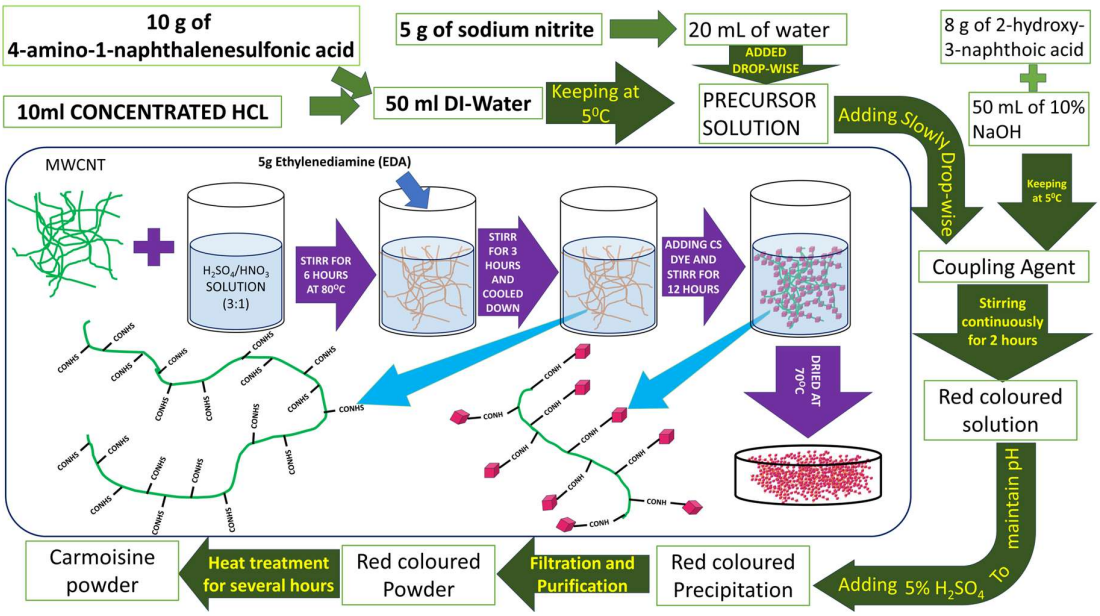

Figure 5.1: Schematic Diagram of the Synthesis Process. (Inset) Schematic Diagram of the Composite Synthesis Process.

5.2.3.d Preparation of ITO/Dye-MWCNT/Cu Schottky Cell

The preparation of the cell is the same as stated in our previous chapters

5.2.4 Characterisation

This section focuses on the characterisation of the materials and devices used in the study. It details the techniques and methods employed to analyse their structural, optical, and electrical properties, providing insights into their performance and suitability for the intended application.

5.2.4.a UV-Vis Analysis

The optical property of the thin film was characterised by the SHIMADZU Ultraviolet-Visible spectrophotometer (UV-1900) and the absorbed wavelength for the thin film was found to be at 321 nm and 515 nm (inset of **Figure 5.1(a)**) for n-p* and p-p* transitions respectively. Approximated optical bandgap of 2.14 eV calculated from the Tauc plot (**Figure 5.2(b)**).

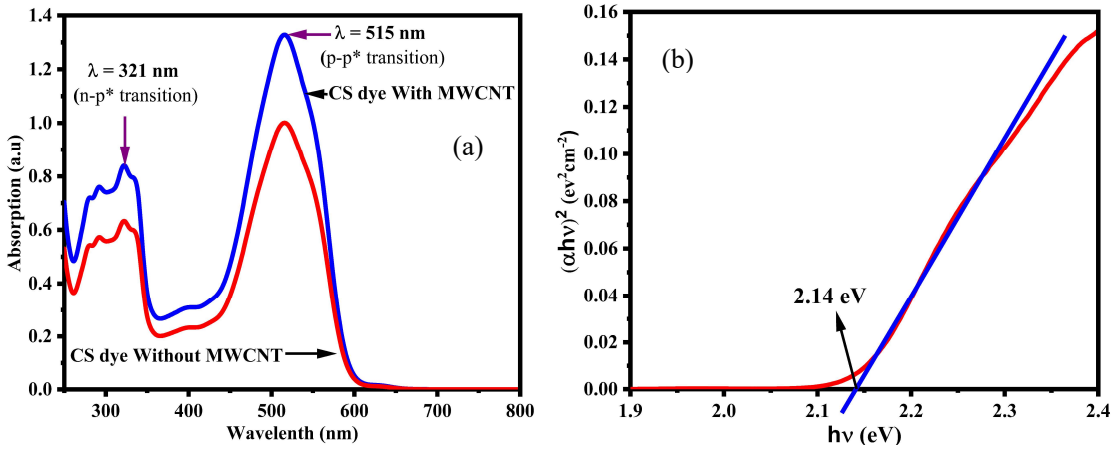

Figure 5.2: (a) UV-Vis spectroscopy of CS dye. (b) Tauc Plot.

5.2.4.b X-Ray Diffraction (XRD) Analysis

The PXRD pattern was measured by the same process and configurations as stated in previous chapters. Refinement of the pattern was carried out using EXPO-2014 software (**Figure 5.3(a)**). It can be inferred that the CS dye shows good crystallinity with a polycrystalline structure.

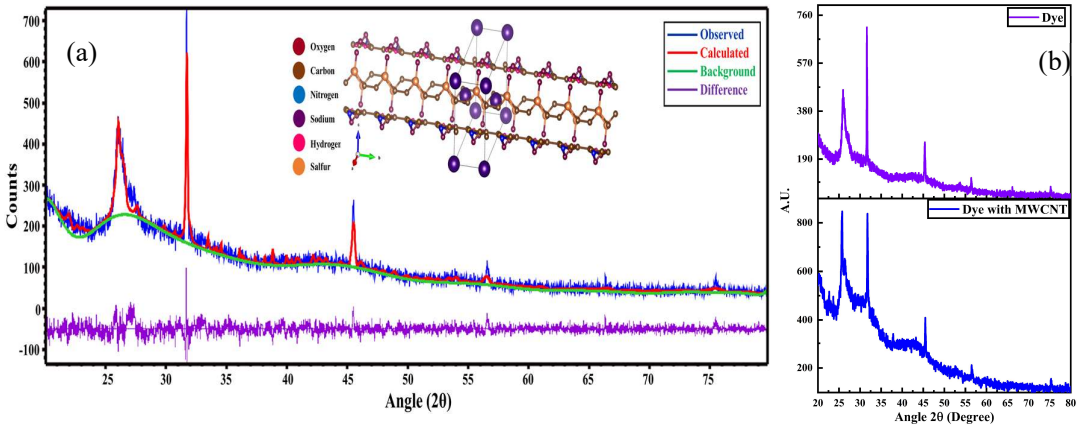

Figure 5.3: (a) The PXRD pattern of the CS dye in powder form. (Inset of (a)) Plausible crystal structure of CS dye. (b) PXRD comparison of dye with and without MWCNTs.

The possible cell structure of the cell is depicted in the inset of **Figure 5.3(a),** and the extracted cell parameters are presented in **Table 5.1** below. The comparison of the PXRD for dye and dye with composite is depicted in **Figure 5.3(b)** which represents the perfect composition of the composites, being the presence of both the MWCNTs and CS dye.

Table 5.1: Calculated crystallographic parameters of CS dye.

Parameter	Result
Lattice type	P
Space group name	P 2/m
Space group number	10
Volume of the unit cell ($Å^3$)	341.820223
A (Å)	10.77928
B (Å)	4.04120
C (Å)	7.91176
A (°)	90.0000
B (°)	97.342
Γ (°)	90.0000

5.2.4.c FESEM Analysis

Distribution of the nanosized particles in the powder format can be seen in the Field-Emission-Scanning-Electron-Microscope (FESEM) image of the CS dye (**Figure 5.4(a)**), and the corresponding particle distribution plot is represented in the inset of Figure 5.4(a). According to the plot, it is found that the average size of the particles is 244 nm. Correspondingly an Energy-Dispersive-Spectroscopy (EDS) detector (Quantax, 200) from Bruker was used to analyses the representation of the detail of the composition of the prepared sample (**Figure 5.4(b)**). In comparison to the FESEM image of the CS dye (**Figure 5.4(a)**) with the FESEM image of the dye incorporated with the MWCNTs (**Figure 5.4(c)**), a perfect mixture of the dye with the CNTs can be inferred and the EDS data of the composition also confirms the same for the mixture (**Figure 5.4(b)**). The FESEM image in **Figure 5.4(c)** reflects the homogeneous distribution of the CS dye over the large surface area of the MWCNTs. Because of the conjugated structure of the dye molecules and the high conductive nature of the MWCNTs, the transfer of charge carriers, such as polarons from the dye and the electrode will be greater, which enhances the conductivity by facilitating overlapping π-electron systems.

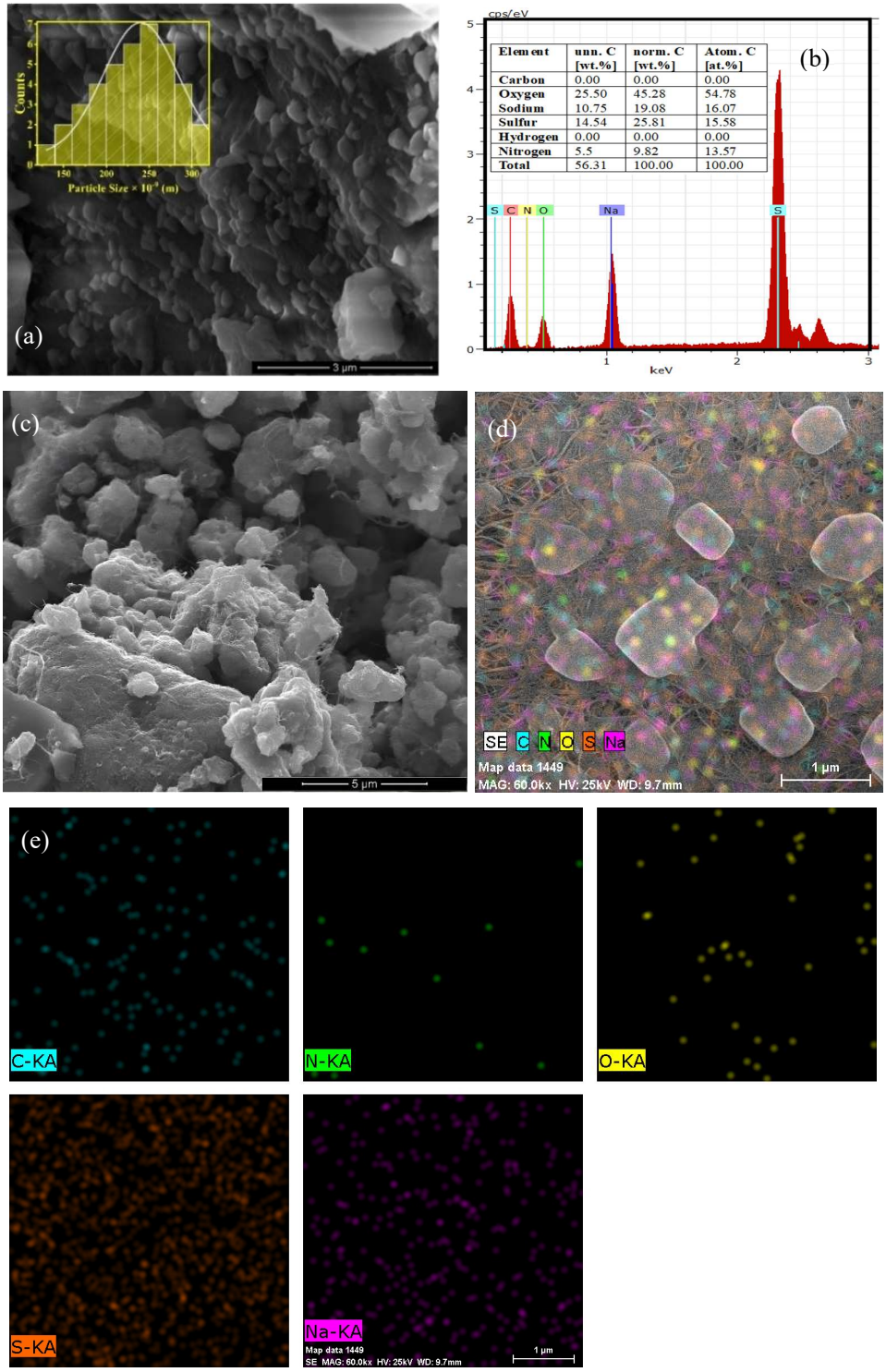

Figure 5.4: (a) FESEM image of the CS dye in powder form represents the crystalline cubic nanoparticles of CS dye. (Inset of (a)) Particle size distribution of CS dye powder. (b) EDX image represents the presence of composites of CS dye. (Inset of Figure (b)) The weight proportion of each element with its CS dye compositions. (c) FESEM image of the dye composited with MWCNTs. (d) and (e) Represents the EDX mapping for the CS dye.

5.7 Results and Discussion

This section presents the experimental results along with a detailed discussion and analysis of the findings. It highlights the significance of the observed outcomes and explores their broader implications in the context of the study.

5.7.1 Analysis of Polaron Hopping Parameters

Considering our previous articles [24–27], analysis of AC-conductivity ($\sigma_{AC}(\omega)$) can be used to determine the type of polaron conduction mechanism for the CS dye-based device incorporated with MWCNTs. Considering an AC supply of varying frequency range from 500 Hz to 100 kHz used for studying the $\sigma_{AC}(\omega)$ of CS-MWCNTs composite thin film along with a variation of temperature of 288 K to 373K.

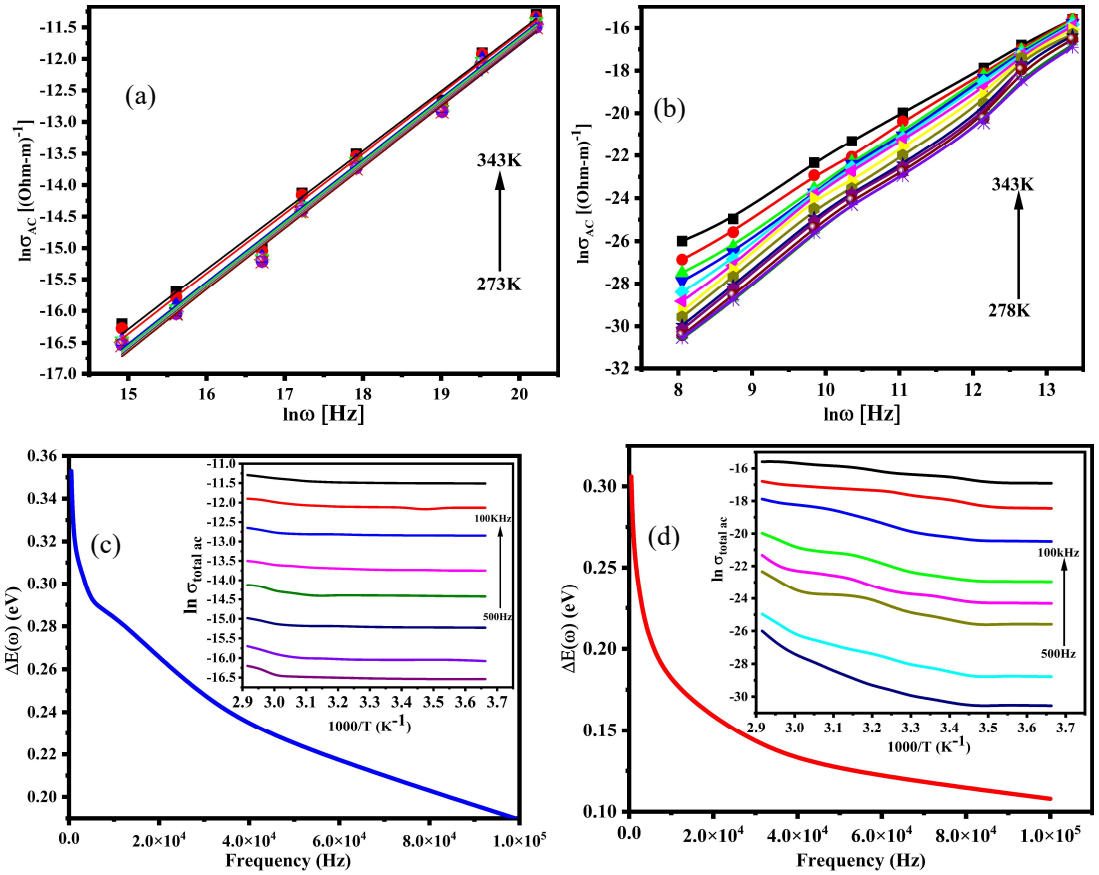

Figure 5.5: (a) and (b) Variation of $\sigma_{AC}(\omega)$ with the temperature for dye and dye incorporated with MWCNT, respectively. (c) and (d) Dependency of $\Delta E(\omega)$ with the temperature for different frequencies dye and dye incorporated with MWCNT, respectively.

Figure 5.5(a) and **5.5(b)** represents the plot for $\sigma_{AC}(\omega)$ dependency of the cell on temperature for dye and dye with MWCNTs, respectively. The AC-activation energy ($\Delta E(\omega)$) (**Figure 5.5(c)** and **5.5(d)**) has been calculated (**Equation (5.1)**) (Symbols have their usual meanings) [28–30]. From our experimental data, it can be seen that our device completely agrees with the Correlated-Barrier-Hopping (CBH) model among other models, where single polaron hopping is prominent for the polaron-conduction mechanism (**Figure 5.6(a)** and **(b)**). According to the model, different polaron hopping parameters have been calculated by the following equations (**Equation (5.3), (5.4), (5.5)**) (Symbols have their usual notations). The outcomes are depicted in **Table 5.2** below compared to our prior publication. Density of Localised State ($N(E_F)$)and the Hopping Rate (ν_p) can be estimated by the following equation (**Equations (5.6) and (5.7)**).

$$\sigma_{AC}(\omega) = \sigma_0 e^{\frac{-\Delta E(\omega)}{k_B T}} \tag{5.1}$$

$$\sigma_{AC}(\omega) = A\omega^s \tag{5.2}$$

$$W = B_m - \frac{ne^2}{\pi\varepsilon_1(\omega)\varepsilon_0 R} \tag{5.3}$$

$$1 - s = \frac{6k_B T}{B_m} \tag{5.4}$$

$$R_\omega = \frac{e^2}{\pi\varepsilon_1\varepsilon_0\left[B_m - k_B T \ln\left(\frac{1}{\omega\tau_0}\right)\right]} \tag{5.5}$$

$$\sigma_{AC}(\omega) = \frac{\pi}{3}[eN(E_F)]^2 T k_B \alpha^{-5}\omega[\ln(\frac{\nu_{ph}}{\omega})] \tag{5.6}$$

$$\nu_p = \nu_{ph} e^{\frac{E_a}{k_B T}} \tag{5.7}$$

$$\nu_p = \nu_{ph} e^{\frac{E_a}{k_B T}} \tag{5.7}$$

It is clear that the presence of MWCNTs has significantly modified the polaron hopping parameters. There are several reasons behind such modifications. One important reason can be the addition of a highly conductive and interconnected network, which increases the hopping distance and is indicated by

the reduction of $\Delta E(\omega)$ by the incorporation of MWCNTs with compared to the dye without MWCNTs [27]. The presence of MWCNTs helps to reduce the coulomb barrier that polarons have to overcome by neutralising the localised traps and hence decreasing the $\Delta E(\omega)$.

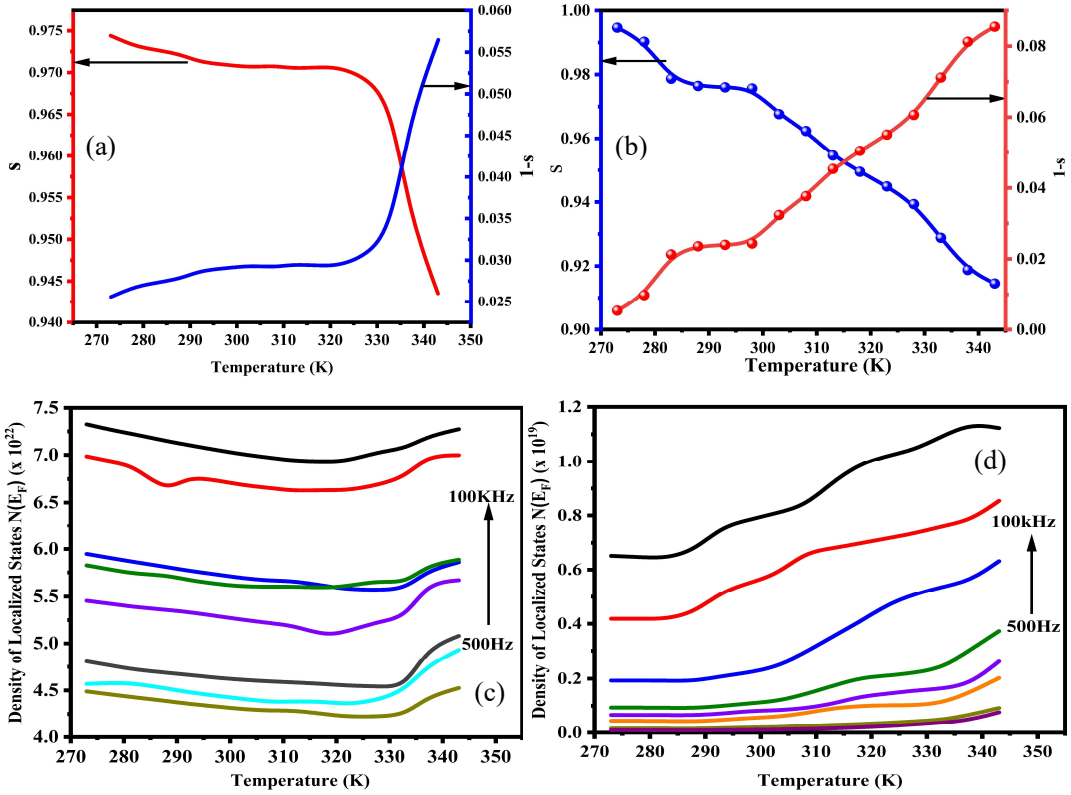

Figure 5.6: (a) and (b) Dependency of S-parameter with temperature dye and dye incorporated with MWCNT, respectively. Plot of temperature dependent N(EF) for different frequencies for (c) dye & (d) MWCNT doped dye

Table 5.2: Polaron hopping parameters

Frequency (kHz)	**Dye without MWCNTs**			**Dye with MWCNTs**		
	R_ω (Å)	**$\nu_p(\times 10^{10})$ Hz**	**B_m (eV)**	**R_ω (Å)**	**$\nu_p(\times 10^{11})$ Hz**	**B_m (eV)**
100	3.9	6.85	0.563	1.07	4.48	0.495
50	4.02	6.67	0.561	1.12	4.30	0.493
30	4.14	6.39	0.548	1.17	4.02	0.48
10	4.33	6.15	0.546	1.23	3.78	0.478
5	4.51	5.92	0.539	1.29	3.55	0.471
3	4.64	5.83	0.534	1.32	3.46	0.466
1	4.83	5.68	0.526	1.37	3.31	0.458
0.5	4.98	5.42	0.518	1.41	3.05	0.450

5.7.2 Analysis of Trap Energy

For a detailed analysis of the trap configuration, we have considered the charge transport mechanism of the cell. Organic materials are often prone to trapping, where defects and impurities create localised energy states within their bandgap. These traps act as recombination centres for polaron energies, thereby affecting the overall hopping length. **Figures 5.7(a)** and **5.7(b)** represent the comparison for the log-log plot of the I-V-T relation for the CS dye-based cells without and with MWCNTs, respectively. As we can see, two different regions from both the figures have different slopes (m).

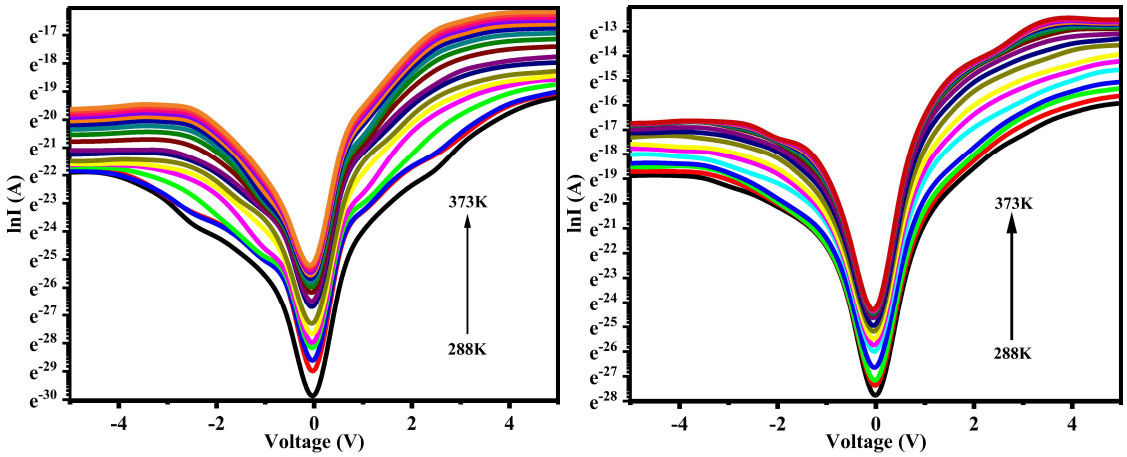

Figure 5.7: lnI-V-T relation of (a) dye and (b) dye with MWCNTs.

Now, for region I, the value of m is found to be around 1 ($m_1 = 0.976$) which suggests an ohmic characteristic of the current-voltage relation. But for region II, the value of m is found to be greater than 2 ($m_2 = 2.246$) which indicates the Space-Charge-Limited-Current (SCLC) mechanism of the device (**Figure 5.8(a)** and **5.8(b)**). Considering the Mott-Gurney relation (**Equation (5.8)-(5.11)**) [32], we have estimated the trap parameters (**Table 5.3**) and we have found an improvement in the SCLC parameters, indicating the reduction in the trap energy inside the material and hence an increase in the overall hopping parameters. According to Marcus' theory [33,34], the hopping rate (ψ) is directly proportional to the ΔE(ω) of the cell (**Equation (5.12)**). As the ΔE(ω) decreases (**Figure 5.5(b)**), the W increases, allowing polarons to access more distant sites more frequently, thereby increasing the R_ω. **Figures 5.8(c)** and **5.8(d)** represent the I vs V^2 plot with temperature for dye and dye with MWCNTS, respectively.

$$J = \frac{9\mu_{eff}\varepsilon_0\varepsilon_r}{8}\left(\frac{V^2}{d^3}\right) \tag{5.8}$$

$$\tau = \frac{9A\varepsilon_0\varepsilon_r}{8d}\left(\frac{V}{I}\right) \tag{5.9}$$

$$\mu_{eff} = \frac{qD}{kT} \tag{5.10}$$

$$\iota_d = \sqrt{2D\tau} \tag{5.11}$$

$$\psi \propto \exp\left[-\frac{\Delta E(\omega)}{k_B T}\right] \tag{5.12}$$

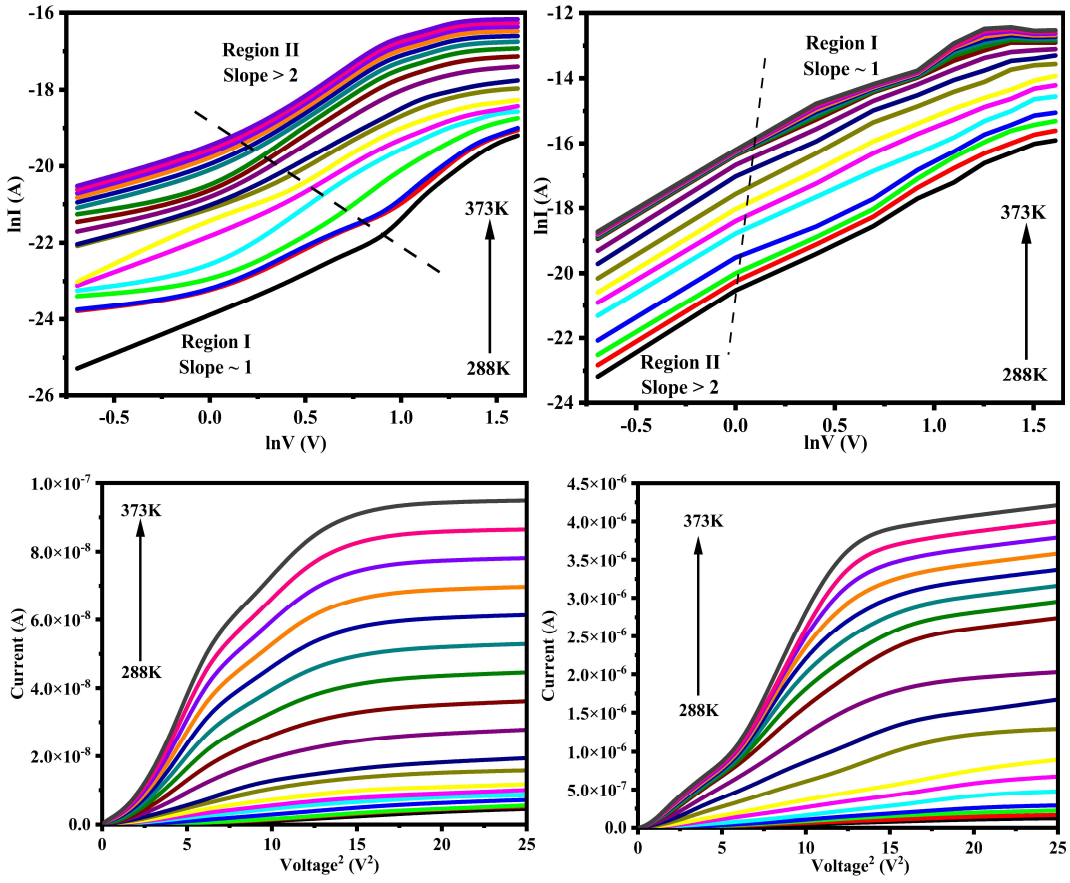

Figure 5.8: lnI-lnV plot for (a) Dye without MWCNTs and (b) Dye with MWCNTs. I-V^2 plot for (c) Dye without MWCNTs and (d) Dye with MWCNTs.

Again, reducing polarisation energy for the charge movement can also be a good reason for the decrease in the polaron hopping length. Higher dielectric constants in the material shield polarons from strong interactions with the lattice, promoting delocalized transport.

Table 5.3: Calculated SCLC parameters

Temperature (K)	Dye without MWCNTs				Dye with MWCNTs			
	$\mu_{eff} \times 10^{-4}$ ($m^2V^{-1}s^{-1}$)	$\tau \times 10^{-3}$ (s)	$D \times 10^{-6}$ (m^2s^{-1})	ι_d (μm)	$\mu_{eff} \times 10^{-4}$ ($m^2V^{-1}s^{-1}$)	$\tau \times 10^{-4}$ (s)	$D \times 10^{-4}$ (m^2s^{-1})	ι_d (μm)
288	2.88609	5.86	7.01668	2.93654	1.750525	9.93244	0.58924	8.93418
293	3.53469	5.52	8.77666	2.94954	2.073345	10.4393	0.68451	9.02252
298	3.56010	4.35	10.4105	2.95574	2.323705	11.0221	0.75431	9.1076
303	3.71362	4.05	11.3810	2.95764	3.014405	11.5359	0.95792	9.18664
308	3.86229	3.64	13.0376	2.95737	3.560935	12.0497	1.11167	9.26865
313	4.01198	3.32	14.7183	2.96075	4.014035	12.9665	1.23267	9.35217
318	4.08789	3.42	14.1545	2.96292	4.877235	14.4215	1.47108	9.42967
323	4.11246	3.39	14.4457	2.97411	5.674505	15.7506	1.68283	9.51028
328	4.28846	3.34	14.8142	2.98259	6.839215	17.5573	1.99323	9.60669
333	4.41730	3.51	14.1306	3.00488	7.989675	20.4433	2.28956	9.68565
338	4.50754	3.63	13.6894	3.02269	8.898035	24.5847	2.50852	9.7663
343	4.76028	3.79	13.1434	3.03941	9.740115	28.6119	2.70146	9.84899
348	4.97053	3.93	12.6767	3.05537	10.88324	34.8466	2.96841	9.93702
353	4.98413	4.08	12.2474	3.07109	11.73644	39.039	3.14849	9.9756
358	5.22406	4.13	12.1857	3.08537	12.27104	46.0773	3.23795	10.0346
363	5.24900	4.26	11.8866	3.10242	12.86954	60.3972	3.33920	10.13316
368	5.30048	4.39	11.5777	3.11804	13.61054	68.1112	3.47132	10.21729
373	5.51504	4.53	11.2404	3.13129	14.31834	81.7877	3.58881	10.32533

5.7.3 Analysis of Dielectric Property

The dielectric constant (ε) indicates how well a material can shield electric fields. A higher dielectric constant diminishes the Coulomb interaction between charge carriers and the lattice, thereby lowering the energy barrier for hopping. By enhancing the screening effect, a higher dielectric constant reduces the self-trapping energy of polarons, enabling them to spread over a wider region, which can lead to an increase in the hopping length. Considering Capacitance-Voltage-Frequency (C-V-T) measurement for dye without and with MWCNTs (**Figures 5.9(a)** and **5.9(b)** respectively) we can estimate the correlation between the ε ant and R_ω. The interfacial parameters have been calculated [35,36] and are given in **Table 5.4** below. We can observe that the dielectric constant has decreased significantly for the device incorporated with MWCNTs. The formation of micro-capacitors inside the module, where nanotubes act as conductive electrodes separated by a dye material (**Figure 5.9(c)**), significantly increases the

overall ε. As a whole, we can see that the R_ω for our cell is directly proportional to ε of the material. An increase in ε results increase in the R_ω for the material, hence an increase in overall conductivity.

5.7.4 Analysis of Barrier Inhomogeneity

Figure 5.10(a) and **5.10(b)** represent the C-V-F plot of dye and dye with MWCNTs, respectively. In organic dye-based photovoltaic and optoelectronic systems, the interplay between barrier height inhomogeneity and polaron hopping length plays a pivotal role in defining the overall efficiency of charge transport and energy conversion mechanisms. Organic semiconductors, unlike their crystalline inorganic counterparts, exhibit significant structural and energetic disorder.

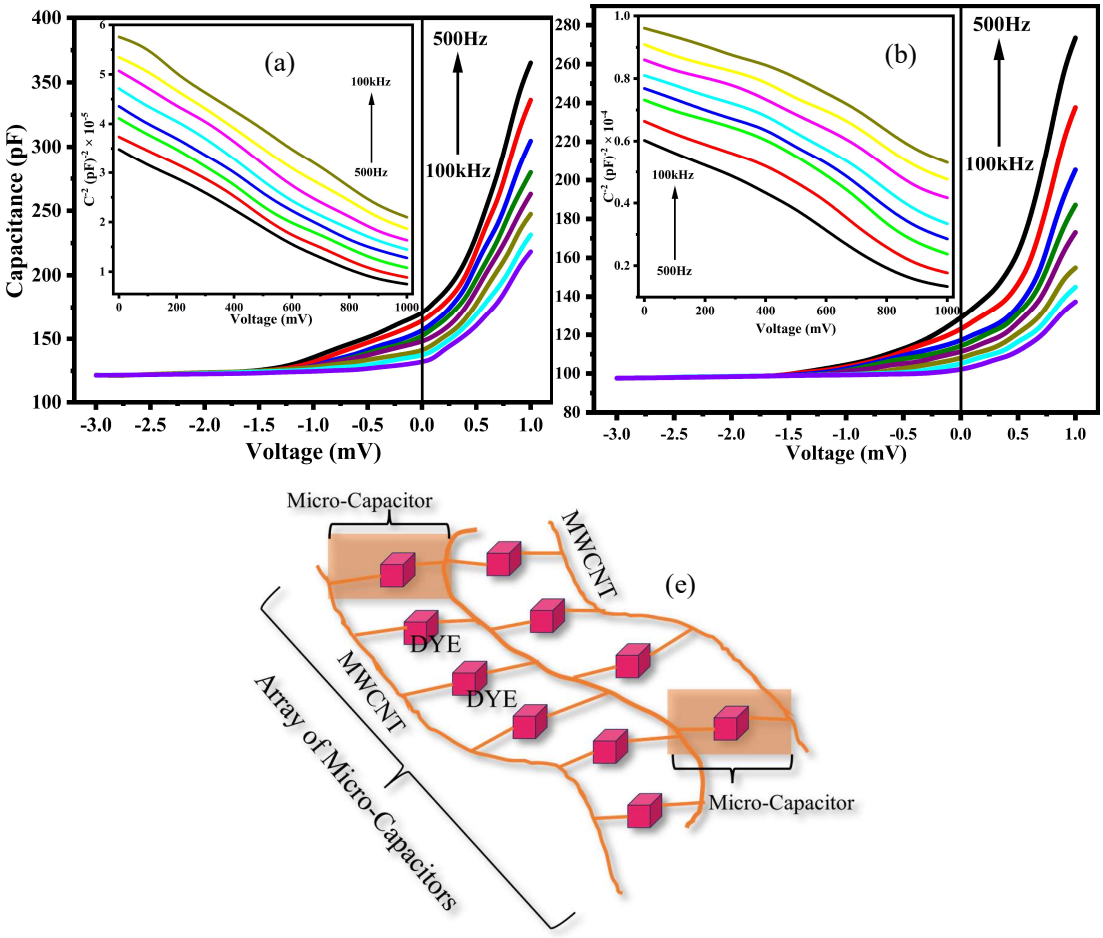

Figure 5.10: C-V-T experiment for (a) Dye and (b) Dye with MWCNTs. (c) Schematic diagram for the formation of micro-capacitors.

This leads to the formation of a non-uniform energy landscape at the interfaces, particularly at the metal–semiconductor junction, where electrons or holes are injected or extracted. The Schottky barrier, formed at this junction, is rarely uniform due to the presence of interface dipoles, chemical impurities, surface roughness, and molecular misalignment. These imperfections cause spatial fluctuations in the local barrier height, known as barrier height inhomogeneity. Such inhomogeneity results in localised potential wells and peaks that alter the electrostatic profile experienced by the charge carriers. In these organic semiconductors, charge carriers do not move freely like in a crystalline lattice. Instead, they are typically bound to lattice distortions, forming quasiparticles called polarons.

Table 5.4: Extracted junction parameters of SY dye with and without NPs.

Frequency (KHz)	Dye without MWCNTs						Dye with MWCNTs					
	ε_s	V_{bi} (eV)	$N_d \times 10^{27}$ (m^{-3})	$E_m \times 10^{2}$ (Vm^{-1})	W_L (cm)	$\Phi_{b(CV)} \times 10^{-1}$ (eV)	ε_s	V_{bi} (eV)	$N_d \times 10^{27}$ (m^{-3})	$E_m \times 10^{3}$ (Vm^{-1})	$W_L \times 10^{-3}$ (cm)	$\Phi_{b(CV)} \times 10^{-1}$ (eV)
0.5	9.3695	0.481	1.089	7.886	0.023	1.74	4.334	0.395	1.991	20.023	5.526	1.503
1	9.5135	0.44	1.004	8.447	0.022	2.068	4.323	0.381	2.055	20.48	5.319	1.809
3	9.6865	0.39	0.886	9.377	0.021	2.286	4.376	0.371	2.136	22.824	5.014	2.024
5	9.8605	0.343	0.763	10.387	0.02	2.57	4.430	0.352	2.103	24.267	4.73	2.223
10	10.123	0.315	0.689	11.731	0.019	2.677	4.572	0.341	2.044	26.437	4.418	2.404
30	10.370	0.293	0.629	13.821	0.018	3.038	4.669	0.313	1.819	29.63	4.049	2.788
50	10.565	0.273	0.563	16.063	0.017	3.539	4.720	0.291	1.656	37.631	3.741	2.915
100	10.753	0.26	0.528	17.884	0.016	3.952	4.833	0.395	18.429	40.669	3.539	2.943

These polarons move via a process known as thermally activated hopping, where they jump from one localised site to another by absorbing thermal energy sufficient to overcome local energy barriers. The hopping process is extremely sensitive to the energetic and spatial distribution of localised states, which are, in turn, affected by the inhomogeneity in the barrier height. When inhomogeneities are pronounced, the distribution of hopping sites becomes wider, and the effective hopping length, that is, the average distance between energetically favourable sites, tends to increase. This reduces the hopping probability and increases the resistance to charge flow. **Figure 5.11(a) and 5.11(b)** represent the Richardson plot comparison of the dye and the dye incorporated with MWCNTs. According the **Chapter 3**, the modification of Richardson Constant represents the modification in the inhomogeneous barrier distribution at the interface. Hence, we can say that modification in the BHI helps to reduce the Polaron hopping length. A possible reason is that the BHI introduces energetic disorder that not only distorts the local electric fields but also alters the activation energy for polaron hopping, leading to inefficient charge transport, increased recombination probability, and a decline in conductivity and PCE. Therefore, minimising barrier inhomogeneities through the

incorporation of MWCNTs enhances the uniformity of charge injection and promotes efficient hopping with shorter hopping distances.

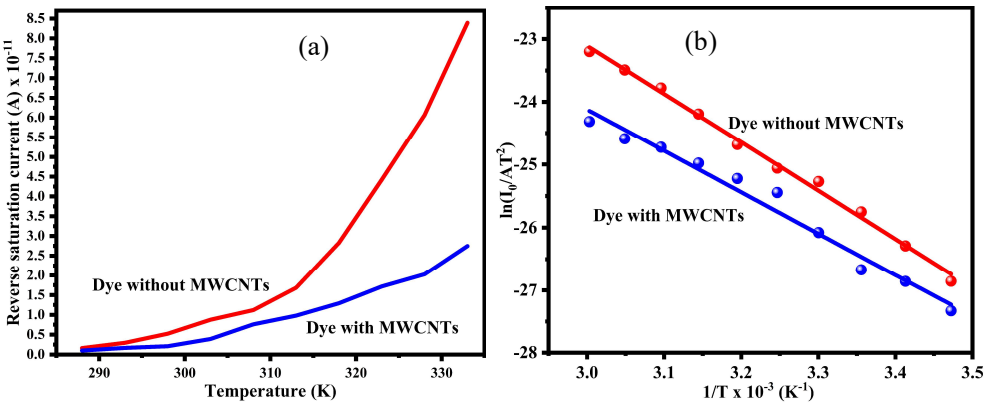

Figure 5.11: (a) Dependency of reverse saturation current with temperature for dye with and without MWCNTs. (b) Richardson plot comparison for dye without and with MWCNTs

5.7.5 Photoelectric Study

Figures 5.12(a) and **5.12(b)** depict the current-voltage (I-V) characteristics of the solar cells at room temperature under illumination (incident light intensity. P_{in}=100 W/m^2), comparing cells without and with multi-walled carbon nanotubes (MWCNTs), respectively. A significant enhancement in photocurrent is observed upon incorporation of MWCNTs. This improvement is attributed to the reduction of trap states and modifications at the interface parameters. The photocurrent transient response during light-on/off cycles is shown in **Figure 5.13(a)**, where the peak photocurrent remains consistent across cycles, with rapid rise and decay times. Furthermore, the current stability over extended periods, as illustrated in **Figures 5.13(b)** and **5.13(c)**, is notably enhanced in cells containing MWCNTs. This is consistent with previous discussions, where MWCNTs contribute to increased electron mobility, facilitating efficient charge separation and transport, thereby suppressing charge recombination and stabilising the photocurrent. Additionally, MWCNTs passivate trap states and defects within the organic dye matrix, reducing recombination at these sites and further promoting photocurrent stability. They also enhance the interfacial barrier properties between the dye and the electrode, enabling more efficient charge transfer and minimising interfacial losses, which supports a sustained photocurrent.

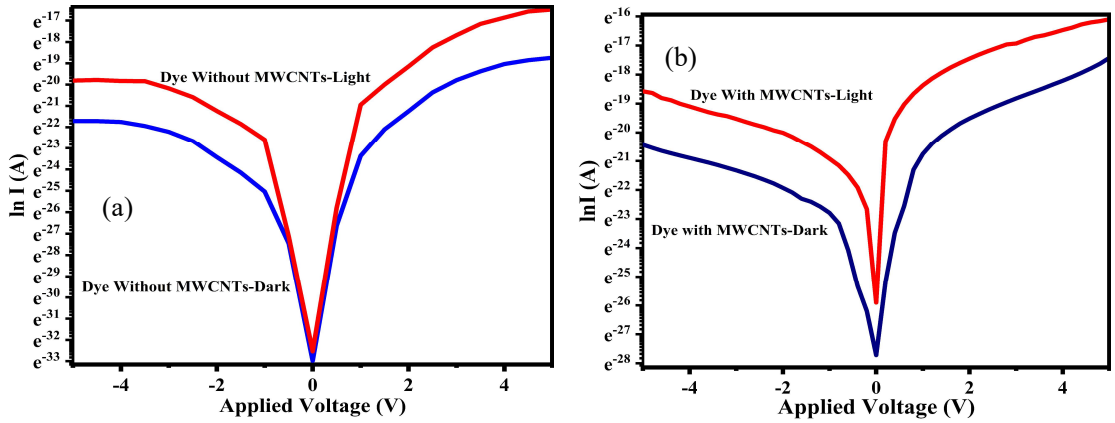

Figure 5.12: Current-Voltage characteristics of dye (a) with and (b) without MWCNTs in illuminated condition.

The comparative current density–voltage (J-V) characteristics under illumination are presented in **Figure 5.13(d)**, demonstrating typical photovoltaic behaviour with identifiable short-circuit current density (J_{sc}) at zero bias and open-circuit voltage (V_{oc}) at zero current. **Figure 5.13(e)** shows the power density (P = JV) as a function of voltage, from which the maximum power output (P_m), corresponding current density (J_m), and voltage (V_m) are extracted and summarised in **Table 5.5**. These parameters were used to calculate the Fill Factor (F_F) and power conversion efficiency (κ). Furthermore, the responsivity (s) of the cell, quantifying its effectiveness in converting incident light into an electrical signal, were determined using **Equation (5.15)**, confirming the device's potential for advanced optoelectronic applications.

$$F_F = \frac{J_m V_m}{J_{sc} V_{oc}} \tag{5.13}$$

$$\kappa = \frac{J_{sc} V_{oc}}{P_{in}} F_F \times 100\% \tag{5.14}$$

$$S = \frac{J_{sc}}{P_{in}} \tag{5.15}$$

The responsivity of the cell was found to increase with the incorporation of MWCNTs, which indicates a modification in the monomolecular recombination mechanism in the cell containing NPs, along with the efficiency of the cell also increases. Incorporating MWCNTs into CS dye enhances polaron transport parameters inside the dye matrices, which reduces recombination losses.

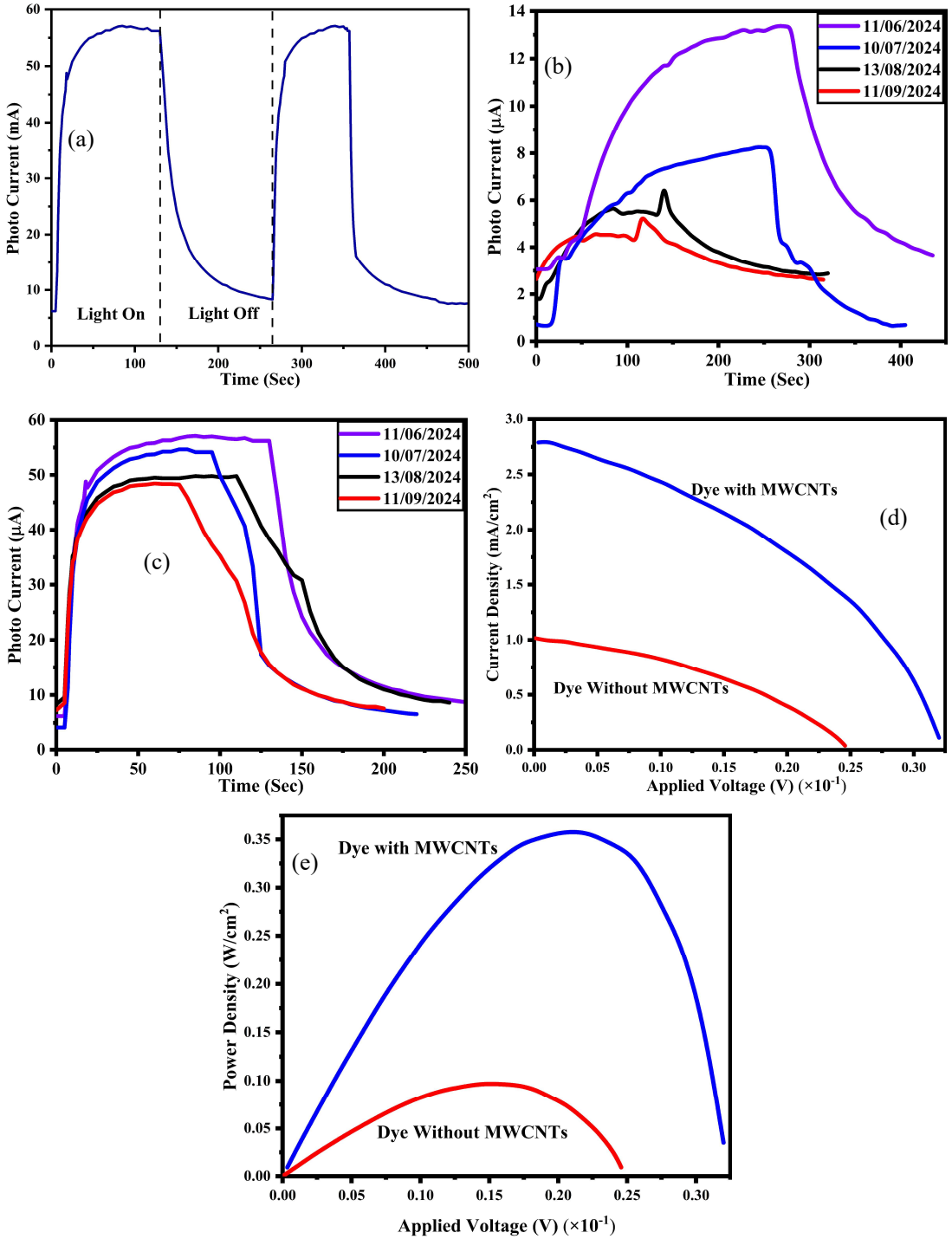

Figure 5.11: (a) Photo response plot of Dye with MWCNTs. Photo-Current Stability of (b) Dye and (c) Dye with ZnO NPs. (d) Current density vs Voltage plot. (e) Variation of power density with the applied voltage.

Table 5.5: Calculated photoelectric parameters

Cell Configuration	V_{oc} (V)	J_{sc} (mAm^{-2})	V_m (V)	J_m (mAm^{-2})	F_F	κ	S (AW^{-1})
Dye Without NPs	0.245	1.016	0.172	0.550	0.380	0.094	0.010
Dye With NPs	0.319	2.789	0.231	1.522	0.395	0.351	0.028

MWCNTs also passivate trap states and defects within the dye, minimising charge carrier trapping. Additionally, they improve the interface between the dye and electrode, facilitating more efficient charge transfer and reducing interfacial losses. These combined effects lead to better charge separation, transport, and collection, resulting in increased photoelectric performance.

5.8 Conclusion

In this chapter, we have estimated the polaron hopping parameters. The incorporation of Multi-Wall Carbon Nanotubes (MWCNTs) into CS dye-based cells presents a significant advancement in enhancing charge transport dynamics, particularly through the modulation of hopping parameters. In disordered organic systems such as CS dye films, charge transport is primarily governed by a thermally activated polaron hopping mechanism. These polarons—charge carriers coupled with localised lattice distortions—require optimised energetic and spatial conditions for efficient transport. Through the inclusion of MWCNTs, several critical hopping parameters have been favourably modified, leading to improved overall device performance. We also found that MWCNTs serve as conductive nanostructures that facilitate the formation of percolation networks, which effectively reduce the hopping length by offering continuous, low-resistance pathways for charge carriers. This reduced hopping distance diminishes the energy and spatial disorder typically observed in purely organic matrices, thereby enabling more efficient polaron migration between localised states. Simultaneously, the presence of MWCNTs introduces additional localised states and defect-assisted pathways that act as shallow traps, which in turn enhance carrier mobility through thermally activated release and re-trapping events behaviour. Moreover, MWCNT doping leads to a measurable decrease in the activation energy required for carrier transport. This is attributed to the modification of the potential energy landscape within the dye matrix, effectively flattening energetic barriers and reducing inhomogeneities at the molecular scale. This directly correlates to a decrease in the barrier height inhomogeneity at the metal–semiconductor interface. The reduction in energetic disorder also aligns with changes observed in thermally stimulated current measurements and I–V characteristics, where the transition from thermionic emission-dominated transport to a hopping-conduction-dominated regime becomes evident at lower applied biases. These modifications contribute to increased electrical conductivity and better device efficiency. The findings highlight the potential of MWCNTs as effective dopants for optimising charge transport in organic electronic devices, paving the way for future advancements in dye-based energy and optoelectronic applications.

5.9 Reference

[1] Khalil Ebrahim Jasim, Seamas Cassidy, Feryad Zaki Henari, Akil Aziz Dakhel, Curcumin Dye-Sensitised Solar Cell, Journal of Energy and Power Engineering 11 (2017). https://doi.org/10.17265/1934-8975/2017.06.006.

[2] A.S. Polo, N.Y. Murakami Iha, Blue sensitisers for solar cells: Natural dyes from Calafate and Jaboticaba, Solar Energy Materials and Solar Cells 90 (2006) 1936–1944. https://doi.org/10.1016/j.solmat.2006.02.006.

[3] H. Naarmann, The development of electrically Conducting Polymers, Advanced Materials 2 (1990) 345–348. https://doi.org/10.1002/adma.19900020802.

[4] M. Irimia-Vladu, E.D. Gåowacki, P.A. Troshin, G. Schwabegger, L. Leonat, D.K. Susarova, O. Krystal, M. Ullah, Y. Kanbur, M.A. Bodea, V.F. Razumov, H. Sitter, S. Bauer, N.S. Sariciftci, Indigo - A natural pigment for high-performance ambipolar organic field effect transistors and circuits, Advanced Materials 24 (2012) 375–380. https://doi.org/10.1002/adma.201102619.

[5] E.D. Glowacki, L. Leonat, G. Voss, M. Bodea, Z. Bozkurt, M. Irimia-Vladu, S. Bauer, N.S. Sariciftci, Natural and nature-inspired semiconductors for organic electronics, Organic Semiconductors in Sensors and Bioelectronics IV 8118 (2011) 81180M. https://doi.org/10.1117/12.892467.

[6] M. Irimia-Vladu, P.A. Troshin, M. Reisinger, G. Schwabegger, M. Ullah, R. Schwoediauer, A. Mumyatov, M. Bodea, J.W. Fergus, V.F. Razumov, H. Sitter, S. Bauer, N.S. Sariciftci, Environmentally sustainable organic field effect transistors, Org Electron 11 (2010) 1974–1990. https://doi.org/10.1016/j.orgel.2010.09.007.

[7] C.J. Bettinger, Z. Bao, Organic thin-film transistors fabricated on resorbable biomaterial substrates, Advanced Materials 22 (2010) 651–655. https://doi.org/10.1002/adma.200902322.

[8] M. Irimia-Vladu, P.A. Troshin, M. Reisinger, L. Shmygleva, Y. Kanbur, G. Schwabegger, M. Bodea, R. Schwödiauer, A. Mumyatov, J.W. Fergus, V.F. Razumov, H. Sitter, N.S. Sariciftci, S. Bauer, Biocompatible and biodegradable materials for organic field-effect transistors, Adv Funct Mater 20 (2010) 4069–4076. https://doi.org/10.1002/adfm.201001031.

[9] W.R. Klaus Hunger, Peter Mischke, Azo Dyes, 1. General, Ullmann's Encyclopedia of Industrial Chemistry (2012). https://doi.org/10.1002/14356007.a03.

[10] J.H. Bombile, S. Shetty, M.J. Janik, S.T. Milner, Polaron hopping barriers and rates in semiconducting polymers, Physical Chemistry Chemical Physics 22 (2020) 4032–4042. https://doi.org/10.1039/c9cp06039a.

[11] L.M. Herz, Charge-Carrier Mobilities in Metal Halide Perovskites: Fundamental Mechanisms and Limits, ACS Energy Lett 2 (2017) 1539–1548. https://doi.org/10.1021/acsenergylett.7b00276.

[12] D. Emin, Polarons in condensed matter, n.d.

[13] V. Coropceanu, J. Cornil, D.A. da Silva Filho, Y. Olivier, R. Silbey, J.L. Brédas, Charge transport in organic semiconductors, Chem Rev 107 (2007) 926–952. https://doi.org/10.1021/cr050140x.

[14] S. Ananthakumar, D. Balaji, J. Ram Kumar, S. Moorthy Babu, Role of co-sensitisation in dye-sensitised and quantum dot-sensitized solar cells, SN Appl Sci 1 (2019). https://doi.org/10.1007/s42452-018-0054-3.

[15] K. Fan, J. Yu, W. Ho, Improving photoanodes to obtain highly efficient dye-sensitized solar cells: A brief review, Mater Horiz 4 (2017) 319–344. https://doi.org/10.1039/c6mh00511j.

[16] V. Vohra, Natural dyes and their derivatives integrated into organic solar cells, Materials 11 (2018). https://doi.org/10.3390/ma11122579.

[17] S.M. Faraz, M. Mazhar, W. Shah, H. Noor, Z.H. Awan, M.H. Sayyad, Comparative study of impedance spectroscopy and photovoltaic properties of metallic and natural dye based dye sensitized solar cells, Physica B Condens Matter 602 (2021). https://doi.org/10.1016/j.physb.2020.412567.

[18] K. Sharma, V. Sharma, S.S. Sharma, Dye-Sensitized Solar Cells: Fundamentals and Current Status, Nanoscale Res Lett 13 (2018). https://doi.org/10.1186/s11671-018-2760-6.

[19] K.J. Hughes, K.A. Iyer, R.E. Bird, J. Ivanov, S. Banerjee, G. Georges, Q.A. Zhou, Review of Carbon Nanotube Research and Development: Materials and Emerging Applications, ACS Appl Nano Mater 7 (2024) 18695–18713. https://doi.org/10.1021/acsanm.4c02721.

[20] R.K. Abu Al-Rub, A.I. Ashour, B.M. Tyson, On the aspect ratio effect of multi-walled carbon nanotube reinforcements on the mechanical properties of cementitious nanocomposites, Constr Build Mater 35 (2012) 647–655. https://doi.org/10.1016/j.conbuildmat.2012.04.086.

[21] J. Qian, J.H. Pu, X.J. Zha, R.Y. Bao, Z.Y. Liu, M.B. Yang, W. Yang, Effect of aspect ratio of multi-wall carbon nanotubes on the dispersion in ethylene-α-octene block copolymer and the properties of the Nanocomposites, Journal of Polymer Research 26 (2019). https://doi.org/10.1007/s10965-019-1915-1.

[22] N.K. Mehra, V. Mishra, N.K. Jain, A review of ligand tethered surface engineered carbon nanotubes, Biomaterials 35 (2014) 1267–1283. https://doi.org/10.1016/j.biomaterials.2013.10.032.

[23] J.Y. Diaz Varela, L.G. Burciaga Jurado, I. Olivas Armendáriz, C.A. Martínez Pérez, C. Chapa González, The role of multi-walled carbon nanotubes in enhancing the hydrolysis and thermal stability of PLA, Sci Rep 14 (2024). https://doi.org/10.1038/s41598-024-58755-8.

[24] A.K. Karan, D. Sahoo, N.B. Manik, Enhanced electrical conductivity and charge conduction mechanisms in Nano-cubical Sunset Yellow dye incorporated with titanium dioxide nanoparticles, Physica B Condens Matter 674 (2024). https://doi.org/10.1016/j.physb.2023.415570.

[25] A.K. Karan, S. Bhunia, N.B. Manik, Study on the Conductivity of a Sunset Yellow Dye-Based Natural Organic Device, J Electron Mater 51 (2022) 7156–7163. https://doi.org/10.1007/s11664-022-09954-4.

[26] A.K. Karan, D. Sahoo, S. Sen, S. Rakshit, S. Bhunia, N.B. Manik, Estimation of activation energy of Tartrazine dye based natural organic device, in: AIP Conf Proc, American Institute of Physics, 2024. https://doi.org/10.1063/5.0206755.

[27] A.K. Karan, D. Sahoo, S. Sen, N.B. Manik, Electrical conduction mechanism of carmoisine dye-based natural organic device, Indian Journal of Physics 98 (2024) 577–583. https://doi.org/10.1007/s12648-023-02833-6.

[28] S.M. Reda, Electric and dielectric properties of some luminescent solar collectors based on phthalocyanines and hematoporphyrin doped PMMA, Dyes and Pigments 75 (2007) 526–532. https://doi.org/10.1016/j.dyepig.2006.06.031.

[29] F. Yakuphanoglu, E. Evin, M. Okutan, The dielectrical and alternating current conductivity properties of 40Cu+20Co+40Y2O3 ceramic, Physica B Condens Matter 382 (2006) 285–289. https://doi.org/10.1016/j.physb.2006.03.001.

[30] S.R. Lukić, S.J. Skuban, F. Skuban, D.M. Petrović, A.S. Tver'yanovich, DC and AC conductivities of (As2S3)100-x(AsSe0.5Te0.5I)x chalcogenide glasses, Physica B Condens Matter 403 (2008) 2578–2583. https://doi.org/10.1016/j.physb.2008.01.038.

[31] S.R. Elliott, A.c. conduction in amorphous chalcogenide and pnictide semiconductors, Adv Phys 36 (1987) 135–217. https://doi.org/10.1080/00018738700101971.

[32] S. Mahato, D. Biswas, L.G. Gerling, C. Voz, J. Puigdollers, Analysis of temperature-dependent current-voltage and capacitance-voltage characteristics of an Au/V2O5/ n -Si Schottky diode, AIP Adv 7 (2017). https://doi.org/10.1063/1.4993553.

[33] Z. Shuai, W. Li, J. Ren, Y. Jiang, H. Geng, Applying Marcus theory to describe the carrier transports in organic semiconductors: Limitations and beyond, Journal of Chemical Physics 153 (2020). https://doi.org/10.1063/5.0018312.

[34] N. Lu, L. Li, W. Banerjee, P. Sun, N. Gao, M. Liu, Charge carrier hopping transport based on Marcus theory and variable-range hopping theory in organic semiconductors, J Appl Phys 118 (2015). https://doi.org/10.1063/1.4927334.

[35] A.K. Karan, Effect of Titanium-Dioxide nanoparticle on Richardson Constant and Barrier Height of Tartrazine Dye based Schottky Device, Discov Mater (2023) 0–11. https://doi.org/10.1007/s43939-023-00040-y.

CHAPTER 6

Conclusion and Findings

Table of Contents

6.1 Summery

In this thesis, we have done an in-depth investigation into the enhancement of charge transport and photoelectric performance in organic dye-based devices through the incorporation of nanomaterials, particularly metal oxide nanoparticles and carbon-based nanostructures such as Multi-Wall Carbon Nanotubes (MWCNTs). The study aims to address the intrinsic limitations of organic and natural dye-based photovoltaic cells, such as low charge carrier mobility, high recombination rates, and poor stability, by integrating nanomaterials that can modulate electrical and optical properties. In this study, we synthesised several organic dyes, such as Brillant-Blue, Sunset-Yellow, and Carmoisine, using a solution processing method. We characterised the physical and optical properties of these materials using various techniques. Then, we fabricated multiple dye-based devices incorporating these materials and investigated their charge transport mechanisms. Our analysis emphasises the role of various parameters like barrier inhomogeneity, activation energy, and polaron hopping mechanism to describe the charge transport mechanism and overall efficiency of the cell.

However, the performance of organic dye-based cells is hindered by factors like poor electronic coupling and inefficient charge injection. To overcome these challenges, the research employs MWCNTs and metal oxide nanoparticles (e.g., ZnO, TiO_2) to alter the morphological, electrical, and interfacial characteristics of the active layer. These nanomaterials serve as charge transport enhancers by forming percolative networks, introducing additional energy levels, and improving the surface area for dye adsorption. We have adopted a combination of experimental techniques, including current-voltage (I–V) analysis, UV-Vis spectroscopy, impedance spectroscopy, and XRD. The study characterises the impact of nanomaterial incorporation on key electrical parameters such as conductivity, activation energy, carrier mobility, and barrier height inhomogeneity. The research also evaluates polaron hopping parameters, which dominate transport in disordered organic systems, and demonstrates how nanoparticles reduce the hopping distance and trap density, thereby facilitating faster and more efficient charge transport.

The following flowchart of the present work is described below.

In Chapter 1, the primary focus was on identifying and analysing the key parameters responsible for the inherently low conductivity observed in organic dye-based photovoltaic and optoelectronic cells. The chapter begins by outlining the fundamental mechanisms that limit

charge carrier mobility and transport efficiency in such systems, including factors such as disordered molecular packing, high trap density, and localized states. Furthermore, the historical evolution of these limiting parameters was explored to provide a comprehensive perspective on how the understanding of conductivity in organic materials has progressed over time.

In chapter 2, we have discussed an in-depth review of the electrical and semiconducting properties of organic dye-based cells, with particular attention to the various challenges faced in improving their performance. This chapter emphasises the critical role played by nanoparticles and carbon nanotubes in enhancing the conductivity and charge transport characteristics of organic semiconductors. By incorporating these nanostructured materials, significant modifications can be achieved in the hopping transport behaviour, trap-assisted conduction, and energy level alignment. A detailed theoretical framework is presented in this chapter to explain the mechanisms through which nanoparticles and nanotubes influence the semiconducting parameters, offering valuable insights into how nanomaterials can be engineered to optimise the performance of organic dye-based devices.

In chapter 3, we have presented a thorough investigation into the impact of titanium dioxide (TiO_2) nanoparticles on the barrier height distribution and electrical performance of metal-semiconductor (MS) contact cells fabricated using Brilliant Blue (BB), a naturally derived organic dye. Organic semiconductor devices are known for their potential in low-cost, flexible, and environmentally friendly electronics, but they often suffer from non-uniform barrier formations at the metal–semiconductor interface due to inherent structural and energetic disorder. This barrier inhomogeneity adversely affects charge injection, transport efficiency, and overall device stability. To address this challenge, the research explores the modification of the interfacial properties by introducing TiO_2 nanoparticles into the BB dye matrix, aiming to reduce the degree of inhomogeneity and enhance electrical characteristics.

The experimental approach involves fabricating two sets of MS contact devices—one based solely on BB dye and another incorporating TiO_2 nanoparticles into the dye layer. The devices are characterized using temperature-dependent current-voltage (I–V–T) measurements over a range of temperatures. The analysis of these measurements reveals that the zero-bias barrier height (Φ_{b0}) increases with rising temperature, while the ideality factor (n) decreases, suggesting that the barrier height is not constant but distributed across the interface. This

behaviour is indicative of barrier inhomogeneity, a common phenomenon in organic materials. A Gaussian distribution model is applied to describe the variation in barrier height, allowing the extraction of statistical parameters. In the BB-only device, the average barrier height is found to be around 0.89 eV with a standard deviation of 0.18 V. Upon the addition of TiO_2 nanoparticles, the average barrier height reduces to 0.75 eV, and the standard deviation decreases significantly to 0.11 V. This reduction in both mean barrier height and spread indicates a more uniform interface, facilitating improved charge injection and transport across the contact.

Complementary capacitance-voltage (C–V) and frequency-dependent C–V (C–V–F) measurements further confirm these findings. The C^{-2}–V plots exhibit changes in slope, suggesting the presence of interface states that influence charge dynamics. The frequency response of capacitance also changes with the introduction of TiO_2 nanoparticles, indicating modified dielectric properties and interfacial behaviour. Using these electrical parameters, the homogeneous Richardson constant is extracted by applying Tung's model, which accounts for inhomogeneous barrier distributions. The Richardson constant is found to be enhanced in the TiO_2-doped devices, supporting the conclusion that the nanoparticle incorporation leads to improved interface uniformity and more efficient thermionic emission of carriers.

Overall, the results demonstrate that TiO_2 nanoparticles play a critical role in modulating the electronic interface between the metal contact and the organic dye layer. By reducing the spatial and energetic disorder at the junction, the nanoparticles promote more consistent barrier formation and enhance carrier injection efficiency. This improvement not only leads to better electrical performance but also contributes to the long-term stability and reproducibility of the device. The study highlights the importance of interface engineering in organic semiconductor devices and suggests that nanomaterial incorporation—specifically TiO_2—can be a viable strategy for overcoming limitations related to barrier inhomogeneity. These findings provide a valuable foundation for the development of high-performance, dye-based optoelectronic and photovoltaic devices, particularly those utilising sustainable and biodegradable materials like Brilliant Blue.

In chapter 4, we have explored the effect of zinc oxide (ZnO) nanoparticles on the activation energy levels, conduction mechanisms, and overall electrical behaviour of organic semiconductor devices based on Sunset Yellow (SY), a natural azo dye. The investigation is

rooted in the growing interest in organic electronics, particularly the use of biodegradable and environmentally friendly dyes as active layers in low-cost, flexible electronic devices. However, one of the major limitations of such organic semiconductors is their relatively poor charge transport performance due to intrinsic disorder, shallow trap states, and high activation energy barriers. To overcome these limitations, this work examines how incorporating ZnO nanoparticles into the SY dye matrix can tune the energy landscape, reduce activation energies, and enhance charge carrier mobility and conduction mechanisms.

The experimental approach involves fabricating Sunset Yellow dye-based devices with and without ZnO nanoparticles using a spin-coating technique. These devices are characterized through a combination of temperature-dependent current-voltage (I–V–T) measurements, AC conductivity studies, and photo-response analyses. The I–V–T measurements are conducted over a range of temperatures (288 K to 333 K) to understand the effect of temperature on charge transport and to extract activation energy values. It is observed that the addition of ZnO nanoparticles leads to a noticeable reduction in activation energy at both low and high temperature regimes. Specifically, the low-temperature activation energy decreases from 0.683 eV (without ZnO) to 0.532 eV (with ZnO), while the high-temperature activation energy reduces from 0.466 eV to 0.351 eV. This reduction is attributed to the introduction of defect states and surface traps by the ZnO nanoparticles, which effectively create shallow energy levels within the bandgap, facilitating easier thermal excitation of charge carriers. Analysis using AC conductivity data indicates that the dominant charge transport mechanism in both sets of devices follows the Correlated Barrier Hopping (CBH) model, a common mechanism in disordered systems where charge carriers hop between localised states. In ZnO-incorporated devices, the hopping distance is significantly reduced, suggesting that the nanoparticles enhance localised state density and reduce spatial disorder, thus enabling more efficient hopping conduction. The improvement in charge transport characteristics is also reflected in the increase in DC conductivity of the devices with ZnO nanoparticles.

Additionally, the study includes photo-response measurements under varying illumination intensities to assess the photovoltaic behaviour of the devices. The J–V characteristics of the SY dye cells with ZnO nanoparticles exhibit improved photocurrent and a clear monomolecular recombination mechanism, which implies enhanced charge separation and transport in the presence of light. The incorporation of ZnO nanoparticles not only lowers energy barriers but

also modifies the Richardson constant and effective barrier height at the metal–semiconductor interface, further contributing to improved charge injection and conduction current.

In chapter 5, we focus on analysing how the incorporation of Multi-Wall Carbon Nanotubes (MWCNTs) into Carmoisine dye-based organic semiconductor devices affects the charge transport mechanisms, specifically through the modification of polaron hopping parameters. Organic semiconductors like Carmoisine dye are widely researched for their potential in low-cost, flexible, and sustainable electronic and optoelectronic applications. However, charge transport in such materials is often limited by the disordered nature of the organic matrix, where localised states and energetic disorder hinder carrier mobility. In these systems, polaron hopping—where charge carriers are coupled with localised lattice distortions—serves as the dominant mechanism of charge transport. The efficiency of this mechanism heavily depends on the hopping distance, activation energy, and spatial distribution of localised states. This work systematically explores how doping Carmoisine dye with MWCNTs alters these critical parameters, aiming to enhance electrical conductivity and overall device performance.

The experimental methodology includes fabricating Carmoisine-based devices both with and without the addition of MWCNTs, followed by detailed characterization using temperature-dependent current-voltage (I–V–T) measurements to analyse the nature of charge transport and extract hopping-related parameters. The results clearly indicate that the MWCNT-doped devices exhibit superior electrical behaviour compared to the undoped ones. Specifically, the incorporation of MWCNTs leads to a noticeable reduction in the activation energy required for carrier transport, which implies that the potential energy barriers between localised states are effectively flattened. This is attributed to the presence of MWCNTs acting as conductive nanostructures that form percolation networks within the organic dye matrix. These networks create continuous low-resistance paths for charge carriers, thereby reducing both the hopping length and the energy required for hopping between localised sites.

In addition to providing efficient transport pathways, MWCNTs also introduce additional localised energy states that serve as shallow traps. These shallow traps facilitate thermally activated hopping, allowing charge carriers to be temporarily trapped and subsequently released, which contributes to an overall increase in carrier mobility. This trap-assisted transport mechanism helps in smoothing the disorder in the potential energy landscape, making the charge transport more consistent and efficient across the device. The improvement in

electrical conductivity and reduced energetic disorder observed in MWCNT-doped devices is also supported by the changes in I–V–T characteristics, where the transition from thermionic emission-dominated behaviour in the undoped device to a hopping conduction-dominated regime in the doped device becomes evident at lower applied biases.

The study also highlights the significance of percolation theory in explaining the enhanced charge transport, where MWCNTs not only serve as direct transport channels but also play a role in reorganising the morphology of the dye matrix, potentially reducing structural defects and promoting better film connectivity. These effects contribute to a more efficient overlap of electronic wavefunctions, which is essential for effective hopping conduction in disordered systems. The observed improvements in carrier injection, mobility, and conductivity underscore the effectiveness of MWCNT doping as a strategy for modifying and optimising the electrical performance of organic semiconducting devices.

6.2 Findings

In chapter 3, we have made a comprehensive investigation into the barrier height inhomogeneity of Brilliant Blue dye in its pristine form and when modified with titanium dioxide nanoparticles.

Table 6.1: Findings about Richardson Constant for BB dye-based cell in the presence of TiO_2 nanoparticles.

Cell Configuration	Homogeneous Richardson Constant (A^*) ($Am^{-2}K^{-2}$)	Barrier Height "ϕ_b" (eV)	Standard Deviation "ζ" (V)
Dye	81.63×10^{-5}	0.89	0.18
Dye + TiO_2	22.85×10^{-5}	0.75	0.11

The temperature-dependent current-voltage study represents a non-linearity in the barrier height, strongly indicating the presence of barrier inhomogeneity, with the dye exhibiting an average value of approximately 0.89 eV. Upon incorporation of TiO_2 nanoparticles, a noticeable reduction in the mean barrier height to around 0.75 eV is observed, which is derived using Gaussian distribution analysis. Additionally, the standard deviation of the barrier

distribution narrows significantly from 0.18 V to 0.11 V, reflecting a marked improvement in barrier uniformity and thereby facilitating enhanced charge injection across the metal-organic interface. Following **Table 6.1** represents the main findings of ths chapter. Furthermore, from the capacitance-voltage (C^{-2}–V) measurement, we found a modification in the device properties like modification in the dielectric constant, maximum allowed electric field, depletion layer width, potential difference between HOMO and fermi energy by incorporation of TiO_2 nanoparticles. **Table 6.2** represents the outcomes and the comparison.

Table 6.2: Findings about Capacitive properties for BB dye-based cell in the presence of TiO_2 nanoparticles.

Frequency (KHz)	Dye Without NPs					Dye With NPs				
	ε_s	V_{bi} (eV)	N_d × 10^{27} (m^{-3})	E_m × 10^2 (Vm^{-1})	W_L × 10^{-6} (cm)	ε_s	V_{bi} (eV)	N_d × 10^{27} (m^{-3})	E_m × 10^3 (Vm^{-1})	W_L × 10^{-6} (cm)
0.5	5.71	0.54	4.93	44.45	9.90	7.75	0.45	7.15	40.82	8.92
1	5.14	0.58	5.28	44.45	9.34	7.03	0.49	7.26	41.84	8.89
3	4.73	0.60	5.48	44.74	8.98	6.61	0.55	7.11	42.45	8.72
5	4.49	0.62	5.54	45.39	8.97	6.17	0.60	7.23	43.97	8.61
10	4.27	0.65	5.61	45.68	8.83	5.77	0.63	7.57	44.31	8.60
30	4.02	0.72	5.92	46.62	8.77	5.45	0.63	7.99	44.77	8.52
50	3.91	0.82	6.17	47.22	8.71	5.12	0.69	8.56	45.56	8.17
100	3.67	0.92	6.94	50.20	8.68	4.84	0.90	18.40	45.93	7.98

Chapter 4 presents a detailed comparative analysis of the conduction mechanisms and photo-response behaviour of Sunset Yellow (SY) dye-based devices with and without the incorporation of zinc oxide (ZnO) nanoparticles (NPs). The integration of ZnO NPs is found to significantly enhance the device's DC electrical conductivity. A key observation is the substantial reduction in activation energies at both low and high temperatures (**Table 6.3**), which is attributed to the emergence of impurity energy states introduced by the ZnO NPs. Also, the Current-voltage analysis reveals a modification in the charge transport property (**Table 6.4**) of the SY dye-based cell by the incorporation of ZnO NPs. Furthermore, alternating current (AC) conductivity measurements also indicate a modification in the different frequency region (**Figure 6.1**). The presence of ZnO NPs considerably shortens the polaron hopping length, leading to improved charge transport dynamics.

Table 6.3: DC activation energy comparison for SY dye-based cell incorporation with ZnO NPs

Configuration	Activation Energy (eV)		Conductivity $(\Omega - m)^{-1}$	
	Low Temperature Limit	High Temperature Limit	Low Temperature Limit	High Temperature Limit
Dye	0.683	0.466	6.18×10^{-8}	1.01×10^{-8}
Dye With ZnO NPs	0.528	0.340	7.70×10^{-7}	8.34×10^{-7}

Table 6.4: SCLC parameters of Sy dye with and without ZnO NPs

Temperature (K)	Dye Without NPs				Dye With NPs			
	$\mu_{eff} \times 10^{-4}$ ($m^2V^{-1}s^{-1}$)	$\tau \times 10^{-3}$ (s)	$D \times 10^{-6}$ (m^2s^{-1})	ι_d (µm)	$\mu_{eff} \times 10^{-}$ ($m^2V^{-1}s^{-1}$)	$\tau \times 10^{-4}$ (s)	$D \times 10^{-4}$ (m^2s^{-1})	ι_d (µm)
288	2.80356	5.21	6.96405	2.69402	1.66799	9.13244	0.53661	8.69166
293	3.45216	4.2	8.72403	2.70702	1.99081	9.63932	0.63188	8.78
298	3.47757	3.55	10.3579	2.71322	2.24117	10.2221	0.70168	8.86508
303	3.63109	3.25	11.3284	2.71512	2.93187	10.7359	0.90529	8.94412
308	3.77976	2.84	12.985	2.71485	3.4784	11.2497	1.05904	9.02613
313	3.92945	2.52	14.6657	2.71823	3.9315	12.1665	1.18004	9.10965
318	4.00536	2.62	14.1019	2.7204	4.7947	13.6215	1.41845	9.18715
323	4.02993	2.59	14.3931	2.73159	5.59197	14.9506	1.6302	9.26776
328	4.20593	2.54	14.7616	2.74007	6.75668	16.7573	1.9406	9.36417
333	4.33477	2.71	14.078	2.76236	7.90714	19.6433	2.23693	9.44313
338	4.42501	2.83	13.6368	2.78017	8.8155	23.7847	2.45589	9.52378
343	4.67775	2.99	13.0908	2.79689	9.65758	27.8119	2.64883	9.60647
348	4.888	3.13	12.6241	2.81285	10.8007	34.0466	2.91578	9.6945
353	4.9016	3.28	12.1948	2.82857	11.6539	38.239	3.09586	9.73308
358	5.14153	3.33	12.1331	2.84285	12.1885	45.2773	3.18532	9.79208
363	5.16647	3.46	11.834	2.8599	12.787	59.5972	3.28657	9.89064
368	5.21795	3.59	11.5251	2.87552	13.528	67.3112	3.41869	9.97477
373	5.43251	3.73	11.1878	2.88877	14.2358	80.9877	3.53618	10.08281

Overall, this research offers meaningful insights into the impact of ZnO nanoparticle incorporation on the electrical and photovoltaic performance of organic dye-based devices and contributes to the broader understanding of how nanomaterials can optimise charge transport in organic semiconductors (**Table 6.6**).

Table 6.6: Photoelectric property comparison

Cell Configuration	V_{oc} (V)	J_{sc} (mAm^{-2})	V_m (V)	J_m (mAm^{-2})	F_F	κ	S (AW^{-1})
Dye Without NPs	0.22	0.840	0.13	0.535	00.377	0.174	21.0
Dye With NPs	0.29	2.316	0.17	1.444	0.366	2.046	23.2

In Chapter 5, we analysed the effect of MWCNTs on the Polaron hopping mechanism for a Carmoisine dye-based Schottky cell. By analysing AC conductivity in detail, we found that both cells with and without MWCNTs obey the Correlated-Barrier-Hopping model. Using this model, we have estimated the polaron hopping parameters, which are modified by the incorporation of MWCNTs. **Table 6.7** represents the related parameters and the calculated values for the cells. Also, we have obtained a result that by the incorporation of MWCNTs, SCLC parameters and dielectric parameters are also modified (**Table 6.8** and **Table 6.9**)

Table 6.7: Polaron Hopping Parameters comparison for CS dye with and without MWCNTs

Frequency (KHz)	Dye without MWCNTs			Dye with MWCNTs		
	R_ω (Å)	$\nu_p(\times 10^{10}$ Hz)	W_m (eV)	R_ω (Å)	$\nu_p(\times 10^{11}$ Hz)	W_m (eV)
100	3.9	6.85	0.563	1.07	4.48	0.495
50	4.02	6.67	0.561	1.12	4.30	0.493
30	4.14	6.39	0.548	1.17	4.02	0.48
10	4.33	6.15	0.546	1.23	3.78	0.478
5	4.51	5.92	0.539	1.29	3.55	0.471
3	4.64	5.83	0.534	1.32	3.46	0.466
1	4.83	5.68	0.526	1.37	3.31	0.458
0.5	4.98	5.42	0.518	1.41	3.05	0.450

Table 6.8: Calculated SCLC Parameters comparison for CS dye with and without MWCNTs

Temperature (K)	Dye without MWCNTs				Dye with MWCNTs			
	$\mu_{eff} \times 10^{-4}$ ($m^2V^{-1}s^{-1}$)	$\tau \times 10^{-3}$ (s)	$D \times 10^{-6}$ (m^2s^{-1})	ι_d (μm)	$\mu_{eff} \times 10^{-4}$ ($m^2V^{-1}s^{-1}$)	$\tau \times 10^{-4}$ (s)	$D \times 10^{-4}$ (m^2s^{-1})	ι_d (μm)
288	2.88609	5.86	7.01668	2.93654	1.750525	9.93244	0.58924	8.93418
293	3.53469	5.52	8.77666	2.94954	2.073345	10.4393	0.68451	9.02252
298	3.56010	4.35	10.4105	2.95574	2.323705	11.0221	0.75431	9.1076
303	3.71362	4.05	11.3810	2.95764	3.014405	11.5359	0.95792	9.18664
308	3.86229	3.64	13.0376	2.95737	3.560935	12.0497	1.11167	9.26865
313	4.01198	3.32	14.7183	2.96075	4.014035	12.9665	1.23267	9.35217
318	4.08789	3.42	14.1545	2.96292	4.877235	14.4215	1.47108	9.42967
323	4.11246	3.39	14.4457	2.97411	5.674505	15.7506	1.68283	9.51028
328	4.28846	3.34	14.8142	2.98259	6.839215	17.5573	1.99323	9.60669
333	4.41730	3.51	14.1306	3.00488	7.989675	20.4433	2.28956	9.68565
338	4.50754	3.63	13.6894	3.02269	8.898035	24.5847	2.50852	9.7663
343	4.76028	3.79	13.1434	3.03941	9.740115	28.6119	2.70146	9.84899
348	4.97053	3.93	12.6767	3.05537	10.88324	34.8466	2.96841	9.93702
353	4.98413	4.08	12.2474	3.07109	11.73644	39.039	3.14849	9.9756
358	5.22406	4.13	12.1857	3.08537	12.27104	46.0773	3.23795	10.0346
363	5.24900	4.26	11.8866	3.10242	12.86954	60.3972	3.33920	10.13316
368	5.30048	4.39	11.5777	3.11804	13.61054	68.1112	3.47132	10.21729
373	5.51504	4.53	11.2404	3.13129	14.31834	81.7877	3.58881	10.32533

Table 6.9: Calculated Dielectric Parameters comparison for CS dye with and without MWCNTs

Frequency (KHz)	Dye without MWCNTs						Dye with MWCNTs					
	ε_s	V_{bi} (eV)	$N_d \times 10^{27}$ (m^{-3})	$E_m \times 10^2$ (Vm^{-1})	W_L (cm)	$\phi_{b(CV)} \times 10^{-1}$ (eV)	ε_s	V_{bi} (eV)	$N_d \times 10^{27}$ (m^{-3})	$E_m \times 10^3$ (Vm^{-1})	$W_L \times 10^{-3}$ (cm)	$\phi_{b(CV)} \times 10^{-1}$ (eV)
0.5	9.3695	0.481	1.089	7.886	0.023	1.74	4.334	0.395	1.991	20.023	5.526	1.503
1	9.5135	0.44	1.004	8.447	0.022	2.068	4.323	0.381	2.055	20.48	5.319	1.809
3	9.6865	0.39	0.886	9.377	0.021	2.286	4.376	0.371	2.136	22.824	5.014	2.024
5	9.8605	0.343	0.763	10.387	0.02	2.57	4.430	0.352	2.103	24.267	4.73	2.223
10	10.123	0.315	0.689	11.731	0.019	2.677	4.572	0.341	2.044	26.437	4.418	2.404
30	10.370	0.293	0.629	13.821	0.018	3.038	4.669	0.313	1.819	29.63	4.049	2.788
50	10.565	0.273	0.563	16.063	0.017	3.539	4.720	0.291	1.656	37.631	3.741	2.915
100	10.753	0.26	0.528	17.884	0.016	3.952	4.833	0.395	18.429	40.669	3.539	2.943

6.3 Overall Conclusion

In the current study, we have looked at different parameters that can affect the overall conductivity of an organic dye-based cell. In this context, we have considered four parameters that must be modified to increase charge transfer and charge transport for an organic Schottky cell, which are Richardson constant, Barrier-Height-Inhomogeneity, Polaron Hoping Length and Hoping Rate. Also, we have investigated and calculated the height of the interfacial barrier, the concentration of traps, the width of the depletion layer, band bending, image force barrier lowering and barrier inhomogeneities at the M/O interface. Interfacial band bending and image force barrier lowering of these organic devices are strongly correlated with Barrier height Inhomogeneity and Polaron Hopping Mechanism. Reduced values for both factors improve charge injection, which also improves conductivity. We have calculated the above-stated parameters of various organic dye-based devices such as Brilliant Blue, Sunset Yellow, Carmoisine dyes and analysed the effects of ZnO, TiO_2, and MWCNT on M/O junction parameters. A reduction in interfacial barrier height inhomogeneity, trap concentration, depletion layer width, band bending, image force barrier lowering, and barrier inhomogeneities at the M/O interface has been observed to improve device performance when ZnO, TiO_2, and MWCNT are present.

Additionally, we have analysed the photoelectric effect. As a result, we have found that by the incorporation of NPs and MWCNTs, the power conversion efficiency increased, and the stability was also modified.

6.4 Future Scope

Future research should focus on optimising nanoparticle concentration to balance performance enhancement with material stability, conducting long-term durability and ageing tests under environmental stress, and expanding the study to include other natural dyes and nanostructures such as graphene derivatives and metal-organic frameworks. Additionally, improvements in device architecture, including multilayer configurations and tandem cells, combined with scalable fabrication techniques like roll-to-roll processing or inkjet printing, could support the transition of these materials from laboratory-scale prototypes to commercially viable technologies. Integration of experimental studies with advanced computational modelling, such as density functional theory (DFT), kinetic Monte Carlo simulations, and device-level simulations, could provide deeper insight into the structure–property relationships and help guide the rational design of highly efficient, low-cost, and environmentally sustainable organic electronic devices.

----------0----------

List of Publications Included in this Thesis

[1] **A.K. Karan**, N.B. Manik, Estimation of Richardson Constant for Natural Organic dye Based Cells using Orange-lemon and Apple-green, **International Journal of Innovative Research in Physics 2**. 62–67. **2021**.

[2] **A.K. Karan**, D. Sahoo, S. Sen, N.B. Manik, Evaluation of Richardson Constant of Fruit dyes using Carmoisine and Tartrazine, **International Journal of Innovative Research in Physics** 3. 25–31. **2022**.

[3] **A.K. Karan**, S. Bhunia, N.B. Manik, Study on the Conductivity of a Sunset Yellow Dye-Based Natural Organic Device, **J Electron Mater** 51. 7156–7163. **2022**.

[4] **A.K. Karan**, D. Sahoo, N.B. Manik, Investigating the effects of TiO_2 nanoparticles on the barrier inhomogeneity of brilliant-blue fruit dye-base solar cell, **Current Applied Physics**, 59, 95–104. **2024**.

[5] **A.K. Karan**, D. Sahoo, S. Sen, N.B. Manik, Electrical conduction mechanism of Carmoisine dye-based natural organic device, **Indian Journal of Physics** 98 (2024) 577–583.

[6] **A.K. Karan**, D. Sahoo, N.B. Manik, Enhanced Semiconducting and Photoelectric property of Organic Diode using Sunset-Yellow Dye composited with Zinc-Oxide Nanoparticles, **AIP Conf Proc, American Institute of Physics**, (communicated) **2024**.

[7] **A.K. Karan**, D. Sahoo, N.B. Manik, Enhanced Semiconducting and Photoelectric properties of Synthesised Carnosine dye based cell composited with Multi-Wall Carbon Nanotube, **Communicated**

List of Publications Not Included in this Thesis

[8] **A.K. Karan**, Effect of Titanium-Dioxide nanoparticle on Richardson Constant and Barrier Height of Tartrazine Dye based Schottky Device, **Discov Mater**. 0–11. **2022**.

[9] **A.K. Karan**, D. Sahoo, N.B. Manik, Enhanced electrical conductivity and charge conduction mechanisms in Nano-cubical Sunset Yellow dye incorporated with titanium dioxide nanoparticles, **Physica B Condensed Matter** 674. **2024**.

[10] **A.K. Karan**, D. Sahoo, S. Sen, S. Rakshit, N.B. Manik, Modification of barrier height inhomogeneity in the presence of titanium dioxide nanoparticles on Carmoisine dye-based Schottky device, **Surfaces and Interfaces** 46. **2024**.

[11] **A.K. Karan**, D. Sahoo, S. Sen, S. Rakshit, S. Bhunia, N.B. Manik, Estimation of activation energy of Tartrazine dye based natural organic device, in: **AIP Conf Proc, American Institute of Physics**, **2024**.

List of Publications as Collaborative Author

[1] D. Sahoo, **A.K. Karan**, N.B. Manik, Electrical charge transport properties of caesium tin chloride perovskite microrods: An analysis of microstructure conductivity and charge trapping, **Mater Lett** 339. **2023**.

[2] D. Sahoo, **A.K. Karan**, N.B. Manik, Influence of SWCNT on the Electrical Behaviour of an Environmentally Friendly CH3NH3SnI3 Perovskite-Based Optoelectronic Schottky Device, **ACS Appl Electron Mater**, **2023**.

[3] D. Sahoo, **A.K. Karan**, Z. Mallick, N.B. Manik, Synthesis and complex impedance analysis of nano cubic CH3NH3SnI3 perovskite for the development of optoelectronic lead-free Schottky diode, **Mater Science in Semiconductor Processing,** 155. **2023**.

[4] M. Shit, **A.K. Karan**, D. Sahoo, N.B. Manik, B. Dutta, C. Sinha, Strategy for the improvement of electrical conductivity of a 3D Zn(ii)-coordination polymer doubly bridged by mesaconato and pyridyl-isonicotinoyl hydrazide based Schottky diode device, **New Journal of Chemistry,** 47. 5922–5929. **2023**.

[5] S. Rakshit, **A.K. Karan**, N.B. Manik, Enhanced Electrical Transport Properties of Beetroot Dye-Based Thin Film in Presence of Titanium Dioxide Nanoparticles, **Journal of Electron Materials** 53. 3914–3925. **2024**.

[6] M. Shit, S. Halder, K. Manna, **A.K. Karan**, A. Samanta, N.B. Manik, S. Pal, K. Jana, C. Sinha, Mn(II) 3D Coordination Framework with Mixed 5-Aminoisophthalato and Pyridyl-isonicotinoyl Hydrazone Bridges: Structure, Electrical Conductivity, Anticancer Activity, and Drug Delivery, **ACS Appl Polym Mater** 6. 2637–2648. **2024**.

[7] M. Shit, **A.K. Karan**, S. Maity, A.M.Z. Slawin, N.B. Manik, B. Dutta, C. Sinha, Succinato-bridged Cd(II)-nicotinylhydrazone 3D coordination polymer: structure, photoconductivity and computational studies, **J Coord Chem** 77. 142–154. **2024.**

[8] D. Sahoo, **A.K. Karan**, N.B. Manik, Study on the effect of temperature on electrical parameters of lead-free methylammonium tin halide-based Perovskite Schottky Devices, **International Journal of Innovative Research in Physics,** 4.6–16. **2022**.

[9] D. Sahoo, P. Sengupta, **A.K. Karan**, N.B. Manik, Improvement in conductivity of lead-free $CH_3NH_3SnI_3$ perovskite thin film using multi-walled carbon nanotubes as a transporter, **Surfaces and Interfaces**, 41. **2023**.

[10] A. Samanta, M. Shit, **A.K. Karan**, N.B. Manik, C. Sinha, S. Khanra, Zn(II)-based 2D coordination polymer bridged by isophthalate and Dipyridylsulphide : Structural characterisation, Schottky diode device and theoretical interpretation, **Journal of Molecular Structure,** 1321(2023):139866, **2024**.

[11] S. Rakshit, **A.K. Karan**, N.B. Manik, Investigation of the effect of single walled carbon nanotube (SWCNT) on semiconducting properties of turmeric dye based Schottky device: a space charge limited conduction approach, **Journal of Materials Science: Materials in Electronics,** 36, 821. **2025**.

[12] D. Sahoo, **A.K. Karan**, N.B. Manik, MWCNT-Enhanced Cs_2SnCl_6 Perovskite for Improved Charge Transport in a Smartphone-Interfaced UV Photodetector, **ACS Applied Electronic Materials,** 7(9), **2025**.

List of National/International Conferences

[1] Effect of Titanium-Di-Oxide (TiO_2) on Malachite Green Dye-based Organic Diode, **National Seminar on New Directions in Physical Sciences 2020**, Subhra Rakshit, **Arnab Kanti Karan**, Dipankar Sahoo, Nabin Baran Manik, (**2020**).

[2] Estimation of Richardson Constant for Natural Organic dye Based Cells using Orange-lemon and Apple-green**, 3rd International Conference on Current Trends in Materials Science & Engineering (CTMSE 2021)**, **Arnab Kanti Karan**, Nabin Baran Manik, (**2021**).

[3] Study on the Conductivity of Natural Organic Dye-based Device Using Tartrazine Dye, **International Conference on Recent Trends in Green Chemistry (ICRTGC-2021), Arnab Kanti Karan**, Dipankar Sahoo, Nabin Baran Manik, (**2021**).

[4] Estimation of Activation Energy of Tartrazine Dye based Natural Organic Device, **4th International Conference on Current Trends in Materials Science & Engineering (CTMSE 2022)**, **Arnab Kanti Karan**, Dipankar Sahoo, Sudipta Sen, Subhra Rakshit, Swapan Bhunia, Nabin Baran Manik, (2022).

[5] Effect of Titanium-Dioxide nanoparticle on Richardson Constant of Sunset Yellow dye-based Cell, **International Conference on Nanotechnology (ICNT-2022)", Arnab Kanti Karan**, Dipankar Sahoo, Sudipta Sen, Nabin Baran Manik, (**2022**).

[6] Evaluation of Richardson Constant of Fruit dyes using Carmoisine and Tartrazine, **International Conference on Advanced Physics (IEMPHYS-2022), Arnab Kanti Karan**, Dipankar Sahoo, Sudipta Sen, Nabin Baran Manik, (**2022**).

[7] Estimation of Richardson Constant and Barrier Inhomogenity in the presence of Titanium Dioxide nanoparticle on Fruit Dye based Organic Schottky device using Tartrazine Dye, **30th National Conference on Condensed Matter Days (CMDAYS-2022), Arnab Kanti Karan**, Dipankar Sahoo, Sudipta Sen, Subhra Rakshit, Nabin Baran Manik, (**2022**).

[8] Modification of Richardson Constant and Interfacial Potential in the presence of Titanium Dioxide nanoparticles on Carmoisine Dye Based Device, **7th International Conference on Nanoscience and Nanotechnology (ICONN-2023), Arnab Kanti Karan**, Dipankar Sahoo, Sudipta Sen, Subhra Rakshit, Nabin Baran Manik, (**2023**).

[9] Improved Conductivity through Barrier Inhomogeneity Modification via TiO2 Nanoparticle Integration in Sunset Yellow Dye-Based Schottky Diode, **31st National Conference on Condensed Matter Days (CMDAYS-2023), Arnab Kanti Karan**, Dipankar Sahoo, Nabin Baran Manik, (**2023**).

[10] Investigating the Influence of Titanium Dioxide Nanoparticle Doping on the Polaron Hopping Distance in Cells Utilising Tartrazine Dye**, 4th International Conference on Material Science (ICMS-2024), Arnab Kanti Karan**, Dipankar Sahoo, Nabin Baran Manik, (**2024**).

[11] Highly Efficient Photo-Electric Behaviour of Carnosine-based Synthetic DSSC incorporated with Zinc-Oxide Nanoparticles, **32nd National Conference on Condensed Matter Days (CMDAYS-2024), Arnab Kanti Karan**, Dipankar Sahoo, Nabin Baran Manik, (**2024**).

[12] Enhanced Semiconducting and Photoelectric property of Synthesized Carmosine Dye-based cell composites with Multi-Wall Carbon Nanotube, **9th International Conference on Nanoscience and Nanotechnology (ICONN-2023), Arnab Kanti Karan**, Dipankar Sahoo, Nabin Baran Manik, (**2025**).